The Study of Giant Exoplanets beyond the Snow Line by Using Gravitational Microlensing

Daisuke Suzuki

A Doctoral dissertation

Department of Earth and Space Science,
Graduate School of Science,
Osaka University

February 4, 2014

Contents

List of Figures

List of Tables

Abstract

We report on the analysis of a planetary microlensing event MOA-2008-BLG-379, and the statistical analysis of the archival MOA-II data in 2007–2012.

MOA-2008-BLG-379 has a strong microlensing anomaly at its peak, due to a massive planet with a mass ratio of $q = 6.9 \times 10^{-3}$. We have conducted a Bayesian analysis based on a standard Galactic model to estimate the physical parameters of the lens system. This yields a host star mass of $M_{\rm L} = 0.56^{+0.24}_{-0.27}\ M_\odot$ orbited by a planet of mass $m_{\rm P} = 4.1^{+1.7}_{-1.9}\ M_{\rm Jup}$ at an orbital separation of $a = 3.3^{+1.7}_{-1.2}$ AU at a distance of $D_{\rm L} = 3.3^{+1.3}_{-1.2}$ kpc.

With use of the MOA-II data in 2007–2012, we construct a sample that consists of 1471 single lens events with high signal-to-noise ratio. We found 21 planets which include several new candidates discovered by a systematic modeling of all the anomalous events. We estimate the detection efficiency of the planets in all of our sample w/wo planets. We fit the planet frequency with a power law function $F = F_0(m_{\rm P}/m_0)^\alpha$, where we find $F_0 = 10^{-0.67\pm0.10}$, $\alpha = -0.78 \pm 0.12$, and $m_0 = 95.2\ M_\oplus$. We integrate the planetary mass function and find that a star has on average $0.15^{+0.04}_{-0.03}$ Jupiter like planets ($0.3-10\ M_{\rm Jup}$), $0.52^{+0.18}_{-0.15}$ Neptune like planets ($10-30\ M_\oplus$) within $0.5 < a < 10$ AU. For the planets with mass from $5\ M_\oplus$ to $10\ M_{\rm Jup}$, we find that a star has on average $1.6^{+0.52}_{-0.42}$ planets within $0.5 < a < 10$ AU.

Chapter 1

Introduction

Almost two decades have passed and more than 1000 planets have been found since the first discovery of an extrasolar planet orbiting an ordinary star in 1995 (Mayor & Queloz 1995). The discovered exoplanets are hardly similar to the familiar planets in our solar system, i.e., hot Jupiters: gas giant planets with shorter orbital periods than the Mercury's, and eccentric planets: planets with the high orbital eccentricity. Recently, the planetary systems with multiple Earth size planets orbiting inside of the Mercury's orbit have been found by *Kepler* team (Lissauer et al. 2011), who searches for transits of the exoplanets by using *Kepler* space telescope. Also, the *Kepler*'s discoveries of circumbinary planets (Doyle et al. 2011), where planets orbit two stars instead of one, confirmed a science-fiction planets as a real world. Thus, the exoplanet discoveries have driven us to explain how these planets formed and search for smaller planets with the goal of discovering another Earth.

In order to explain how these planetary systems and our solar system formed, planet formation theories have been developed. A major planet formation theory is the core accretion model (Lissauer 1993, Pollack et al. 1996). In the core accretion model, planetesimals grow through the coagulation process and reach the critical mass of roughly 10 $M_\oplus$, which triggers the run away gas accretion on the planet if a lot of gas remain in the proto planetary disk. This is more likely to happen at the out side of the so-called snow line, beyond which the temperature is cold enough for ices to condense, because the surface density on the proto planetary disk increases by a factor of 3–4 beyond the snow line (Ida & Lin 2005, Lecar et al. 2006, Kennedy et al. 2006, Kennedy & Kenyon 2008) . The enhancement of the surface density facilitates the formation of large cores. The location of the snow line for main sequence star is given by ~ 2.7 AU $(M/M_\odot)^2$ (Ida & Lin 2004a). The scaling coefficient with stellar mass depends on the stellar luminosity–mass relation, which is a function of stellar age. In this thesis, we choose the coefficient such that the snow line scales to the stellar luminosity at the time of planet formation, $\sim 10^6$ yr.

Thus, the snow line is given by ~ 2.7 AU $M/M_{\odot}$ (Kennedy & Kenyon 2008). If the gas has already dissipated when the planets exceed the critical mass, they can not get enough gas accretion. Then they become failed Jupiter cores like Neptune or Super Earth (Kennedy & Kenyon 2008), and such planets have been founded(Muraki et al. 2011).

Population synthesis simulations (Ida & Lin 2004a, Mordasini et al. 2009) showed the predictions of planet distribution on an a-$m_{\rm P}$ plane, where a and $m_{\rm P}$ are semi-major axis and planet mass, respectively, based on the core accretion theory. Ida & Lin (2004a) expects a "planet desert" that is a deficit of planets with $M = 10-100\ M_{\oplus}$ and $a = 0.2-3$ AU. They also predict a higher frequency of low mass planets compared to gas giants. Mordasini et al. (2009) also gives the similar results, but they expect that the planet desert might be slightly smoothed. These results are based on the general physical considerations, but also depend on a number of simplifications. Thus, these expectation should be tested by observational data.

Most of the planets were discovered through the radial velocity (Butler et al. 2006, Bonfils et al. 2013) and transit (Borucki et al. 2011) methods, which are the most sensitive to the planets orbiting close to their host stars. In contrast, direct imaging is the most sensitive to young planets in orbits wider than that of Saturn (Marois et al. 2008). The gravitational microlensing method (Bennett & Rhie 1996) has unique sensitivity to the planets with masses down to Earth mass orbiting just outside of the snow line (see Figure 1.1). Here, we briefly review the detection methods for exoplanets.

- Radial Velocity

  The first exoplanet (Mayor & Queloz 1995) and the most of the planets known today were discovered by this method. The radial velocity (RV) method, also called as Doppler method, measures the star' s line-of-sight velocity by using high resolution spectroscopy. If a star has a planet, they orbit about the center of mass. By analyzing the repeating patterns in the time series of RV, the orbital period and minimum mass ($m_{\rm P}\sin i$, where $m_{\rm P}$ is the mass of the planet and i is the inclination, the angle between the line of sight and the planet's orbital axis) of the planet are characterized. The massive planets with shorter orbital periods are easily detected. The detection of the Jupiter, which orbits about 5 astronomical unit (AU, the Earth-Sun distance), requires the precision of ~ 10 m/s RV for the Sun. The detection of the Earth requires ~ 10 cm/s RV measurement, which has not been achieved yet. The current best precision is ~ 50 cm/s.

- Transit

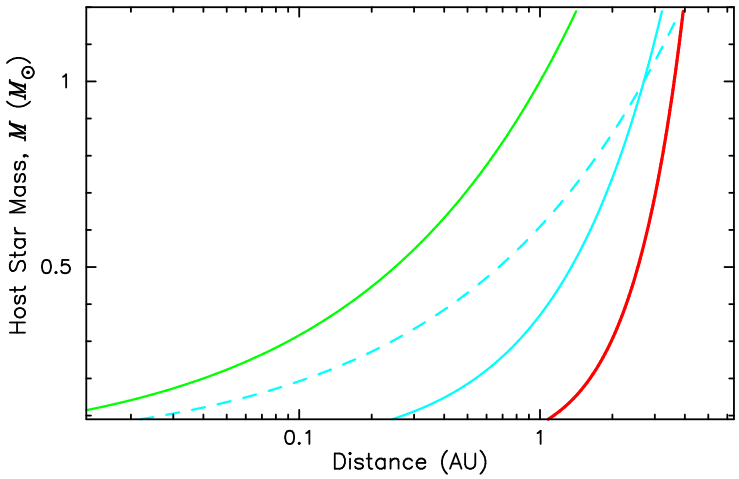

Figure 1.1: Location of the snow line and the region where microlensing has a sensitivity, with different host star masses. The blue dashed line shows the snow line given by 2.7 AU $(M/M_\odot)^2$. The blue solid line shows the snow line given by 2.7 AU $M/M_\odot$ (Kennedy & Kenyon 2008). The red line shows the typical size of the Einstein ring radius, where the microlensing has a peak sensitivity for the planets (see Equation 2.6). The green line shows the approximate location of the habitable zone (Kasting et al. 1993), where an ocean planet could exist.

If a planet has an inclination of $i \simeq 90°$ (edge-on), an eclipse in the extrasolar system can be seen. The probability of a random planetary orbit being along the line-of-sight to a star is given by R/a, where R is the radius of the primary star and a is the semi-major axis of the planet. This leads the probability of transits for an Earth-like planet at 1 AU orbiting a Sun-like star, 0.465 %. By analyzing the light curve of the transit, the radius of the planet can be derived. A Jupiter-size planet occults a Sun-like star by the flux of $\sim$ 1%. This level of the precision has been achieved with ground-based telescopes. But, measuring the enough photometric precision for the detection of Earth-size planets around Sun-like stars requires space telescopes, such as *Kepler* mission (Borucki et al. 2011), which is one of the most successful survey for exoplanets.

Transit method is widely applicable to derive the information of planetary systems. In combination with an RV measurement of the star with a transit planet, the average density of the planet can be derived, because the RV and transit methods give the mass and radius of the planets, respectively. As of today, the planet densities are measured in $\sim$ 200 planets (Howard 2013). Also, measuring the RV during the transit can derive a stellar obliquity, which is the angle between the stellar spin axis and a planet's orbital axis (Albrecht et al. 2012). This is possible because of the Rossiter-McLaughlin

effect, where the planet alternatively occults the blue and red shift part of RV caused by the stellar spin. If the planetary system has another planets that might not occult the star, the additional planets perturb gravitationally the transiting planet, affecting the mid time of the transit. Measuring the residual from the mid time of the transit, transit timing variation (TTV), can not only discover the another planets but also derive the mass of the planets (Lissauer et al. 2011). Another remarkable aspect is that the difference in the transit light curves in different wavelengths gives us the information on the planet's atmosphere (Narita et al. 2013, Fukui et al. 2013).

- Gravitational Microlensing

  Gravitational microlensing method is very unique in that we need photons from neither the host star nor orbiting planets. Although the close-in planets are more detectable by the RV and transit methods, the microlensing method can detect wide planets with masses down to the Earth mass orbiting at a few AU, which is equivalent to a region just outside of the snow line. These planets could be detectable by the RV method, but the long orbital period requires the long time series observations. The probability of that any microlensing event is occurring at any given time is $\sim 10^{-6}$ even toward the Galactic bulge, where the surface density of stars is the highest. This low probability requires a large number of stars to survey. Although the number of detected planets is much less compared to the RV and transit (see Figure 1.2), the parameter space that microlensing can survey is complimentary to the other method. Thus, to complete a planet distribution map, such as Figure 1.2, the microlensing method is indispensable.

  Unlike the other planet detection method, microlensing is able to detect planets far away from our solar system, i.e., 1–8 kpc. With enough sample, we can estimate the planet frequency as a function of distance from the Sun. Although this is interesting, the distance to the planets can be derived only for the special case (where both finite source and parallax effects can be observed). So, we must wait for statistically large samples to know the relation.

  Microlensing is also unique in its sensitivity to planets orbiting stars that are too faint to detect (Bennett 2008, Gaudi 2012). In fact, planetary mass objects can be detected even in cases when there is no indication of a host star (Sumi et al. 2011). These planetary mass objects, free-floating planets, are thought of as ejected planets from the proto plaentary disks by planet-planet scattering. Complete understanding of the planet formation requires the number of not only orbiting planets but also ejected planets.

- Direct Imaging

One of our ultimate dream is to observe another Earth directly. However, exoplanets are too dim to observe directly and their host stars are relatively too bright. But, by using a spatially high resolution imaging with a occulting mask for the bright host star, it is possible to observe exoplanets directly for the special case where the planets are bright enough due to their youth and far enough from the host star. Currently, dozens of gas giant planets with long semi-major axises have been found by the direct imaging (Rameau et al. 2013).

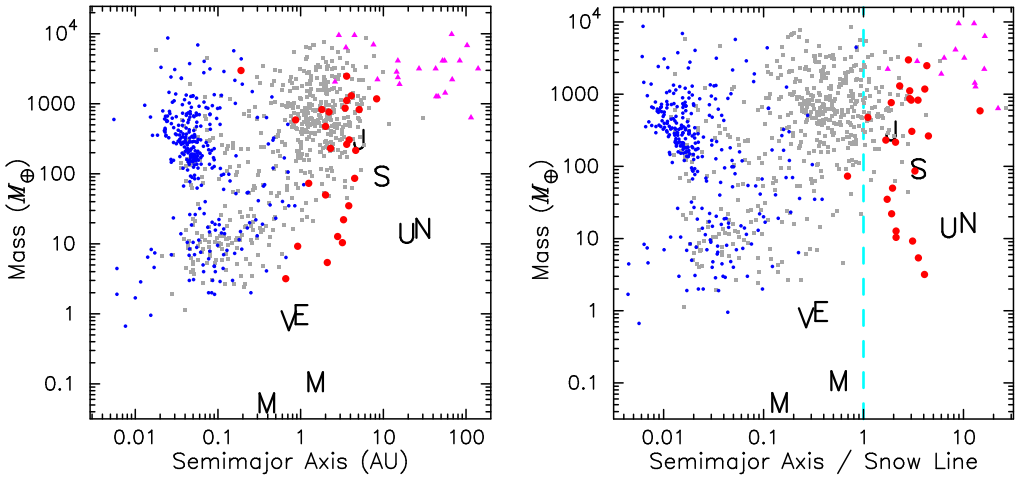

Figure 1.2: Left: Mass versus semimajor axis for known planets. The blue dots show the planets discovered by transit method. The gray squares are the planets discovered by RV method. The magenta triangles are the planets discovered by direct imaging method. The planets discovered by micolensing method are plotted in the red points. The alphabets show the planets in our solar system. Right: Same with the left figure, but the masses are plotted as a function of the semimajor axis normalized by the snow line, which is assumed to depend on the host star mass as ~ 2.7 AU $M/M_\odot$ (Kennedy & Kenyon 2008).

The planets discovered to date are plotted in Figure 1.2. The number of planets discovered by each detection method is large enough to discuss the statistics, i.e., how many exoplanets per star or how frequently the star harboring any planets, depending on the planetary mass, orbital period, primary star mass, and metallicity of the primary star. The RV observations have shown interesting results that can put constraints on the planetary formation scenario:

- The probability of a star hosting a planet per logarithm of planet mass per logarithm of orbital period, is increasing with a decrease of planetary masses and with a logarithm of the orbital periods, $dN = m_{\rm P}^{-0.31\pm0.2} P^{0.26\pm0.1} d\ln m_{\rm P}\, d\ln P$ (Cumming et al. 2008).

- Occurrence (the probability of a given star harboring any planets) of the planet with mass of $3 < m_{\rm P}{\rm sin}i/M_\oplus < 30$ and orbital period $P < 50$ days is $30 \pm 10\%$ (Mayor et al. 2009).

- Occurrence of the planet with mass of $3 < m_{\rm P}{\rm sin}i/M_\oplus < 30$ and orbital period $P < 50$ days is $15^{+5}_{-4}\%$ (Howard et al. 2010).

- About half of Sun-like stars have at least one planet with mass of $m_{\rm P} \lesssim 30\ M_\oplus$ and orbital period of $P < 100$ days (Mayor et al. 2011).

- 14% of Sun-like stars have giant planets with mass of $m_{\rm P} \gtrsim 20\ M_\oplus$ and orbital period of $P < 10$years (Mayor et al. 2011).

- Occurrence of the giant planets (with $m_{\rm P} > 50\ M_\oplus$) is strongly depending on the metallicity of the primary star, but not for the super Earth and Neptune-mass planets (Mayor et al. 2011)

- Occurrence of the close-in giant planets (with $0.44 < m_{\rm P}{\rm sin}i/M_{\rm Jup} < 1.12$, $a < 2.5$ AU), is increasing with both the primary star masses and the primary star metallicity (Johnson et al. 2010b)

- The frequency of habitable planets with mass of $1 \leq m_{\rm P}{\rm sin}i/M_\oplus \leq 10$ orbiting M dwarfs, $\eta_\oplus$, is estimated as $0.41^{+0.54}_{-0.13}$ (Bonfils et al. 2013).

Both the HARPS survey (Mayor et al. 2009, 2011) and η-Earth survey (Howard et al. 2010) have shown that the planets of $m_{\rm P} \lesssim 30\ M_\oplus$ and $P < 50$ days ($a < 0.3$ AU) are abundant, while the population synthesis simulations based on the core accretion model predict the planet desert on that parameter space (Ida & Lin 2004a, Mordasini et al. 2009). But the positive correlation of the occurrence of the hot Jupiters to the primary star mass and metallicity (Johnson et al. 2010b) supports the core accretion model (Ida & Lin 2004b, 2005).

Although transit method can derive only the radius of the planets (except for the special case such as TTV), and the *Kepler* planets in the statistical analysis are still planet candidates, the statistical study by using 1235 *Kepler* planets demonstrates the powerfulness of *Kepler* survey (Howard et al. 2012):

- The planet occurrence is increasing with a decreasing planet radius down to $2\ R_\oplus$.

- Planets with orbital periods $P < 2$ days are very rare; the occurrence of such planets with radius of $R_{\rm p} > 2\ R_\oplus$, is less than 0.1%.

- The "parking distance", inside of which the close-in planet occurrence falls off rapidly, moves outward with decreasing planet size.

- The occurrence of 2–4 $R_\oplus$ planets increases with decreasing the effective temperature of the primary star, $T_{\rm eff}$; seven times more common around cool stars (3600–4100 K) than hottest stars in the sample (6600–7100 K).

The *Kepler* results are partly consistent with the RV result (Howard et al. 2010) in terms of that smaller planets are more common. But the abundant small planets are found in the desert predicted by the core accretion model. Also, the higher occurrence of the planets with 2–4 $R_\oplus$ in the cooler stars, which are equivalent to less massive primary stars, dose not agree with the positive correlation estimated by Johnson et al. (2010b). This could be explained by the metallicity bias in the *Kepler* stars, but further observational results are required to make clear this discrepancy.

The comparison of the observational results by RV and transit with the planet formation models has been tried for the close-in planets. For the planets with wide orbital periods, the observational results by direct imaging method have been compared to the planet formation models. Rameau et al. (2013) put the constraints on the planet formation models by both core accretion and gravitational instability, where a massive cold disk becomes unstable and leads to the clumps of gas and dust becoming giant planets beyond 10 to 20 AU (Stamatellos & Whitworth 2009). Although the constraints are not very strong, the direct imaging surveys suggest that a break-up of the positive correlation of planet occurrence with orbital period between the population of close-in planets and wide-orbit giant planets. This could be probed by microlensing, which can detect planets with the intermediate orbital periods.

Microlensing has indicated that cold planets orbiting a few times the distance of the snow line are quite common (Sumi et al. 2010, Gould et al. 2010a, Cassan et al. 2012). Relatively low-mass cold Neptunes or super-Earths are found to be more common than gas giants, which is in rough agreement with the core accretion theory expectation. Although the gas giants are relatively rare beyond the snow line, $\sim 30\%$ of the discovered planets by microlensing are thought of as gas giants. Furthermore, typical mass of the host stars surveyed by microlensing is $\sim 0.5\ M_\odot$. Thus, the observational fact suggests that the gas giants orbiting around M or K dwarfs beyond the snow line are not uncommon and this may be challenging for the core accretion model.

In this thesis, we present the result of the analysis of a planetary microlensing event MOA-2008-BLG-379, where another gas giant planet is discovered, and the statistical analysis of the archival MOA-II data in 2007–2012. In Chapter 2, we describe the basics of gravitational microlensing and its application for the detection of planets. The MOA project is introduced in Chapter 3. The analysis of MOA-2008-BLG-379 is described in Chapter 4. In Chapter 5, we present the analysis and result of the statistical study. Discussion and our conclusion are presented in

Chapter 6.

Chapter 2

Gravitational Microlensing

2.1 Brief History

One of the distinctive characteristics of microlensing is that this method does not measure the flux from a lens star, but measure the flux from a source star far behind the lens objects. This leads the strength of that the microlensing is able to detect dim objects, such as remnant stars, brown dwarfs and planets, even if the planets have no host stars. In other words, these objects are hard to observe directly, therefore the identification of the host star is the most difficult aspect for the microlensing. But, the original difficulty of detecting microlensing events is a rareness of the phenomena.

Originally, the idea of gravitational lensing, which is the deflection of light by gravity, goes back to the era of Sir Isaac Newton. After two centuries, Lodge (1919) and Eddington (1920) predicted an idea of the phenomena that the light rays from the background star are deflected by a foreground star alined with the line of sight to the background star and result in making the images around the foreground star. Chwolson (1924) remarked that a ring-shaped image of the background star will be produced if the alignment is perfect. Although it seems that Einstein had such an idea in 1912 (Renn et al. 1997), he published a paper in which the lens equation is derived and the amount of magnification is estimated(Einstein 1936). In this paper, he noted that the alignment scarcely happens and the angle of the images are too small to be observed. "Therefore, there is no great chance of observing this phenomenon", as Einstein concluded.

After three decades from the Einstein's paper, Liebes (1964) and Refsdal (1964) estimated the physical quantities of the gravitational lensing phenomena. Liebes (1964) considered the case of that the lens is a star orbited by an Earth like planet, and found there could be a small perturbation by the planet in the lens action of the host star. Liebes (1964) also discussed the lensing effect caused by free-floating

planets and concluded that these events are even more rare in the detectable events and hard to be detected due to the shortness of the event timescale. The both paper considered that the phenomena possibly happen but we can not expect where and when they take place.

Two decades later, Bohdan Paczyński used the term "microlensing" for the first time (Paczyński 1986a). He predicted that microlensing may detect the MAssive Compact Halo Objects (MACHOs) in the Galactic halo, which is one of candidates of the dark matter (Paczyński 1986b). Even before the first detection of the microlensing event and the first detection of the extrasolar planet, Mao & Paczyński (1991) predicted that the extrasolar planets can be found by the microlensing. These paper have driven many collaborations to search for the microlensing events (MACHO collaboration; Alcock et al. 1993a, EROS collaboration; Aubourg et al. 1993, OGLE collaboration; Udalski et al. 1992, MOA collaboration; Bond et al. 2001).

At last, the first microlensing event was discovered towards the Large Magellanic Cloud (LMC) by the MACHO and EROS collaborations (Alcock et al. 1993b). The first detection of a microlensing event towards the Galactic Bulge was reported by the OGLE collaboration (Udalski et al. 1993). For a while, no planetary microlensing events were detected, but interesting upper limits were placed on frequency of the Jupiter masses planets (Rhie et al. 2000, Gaudi et al. 2002). And the OGLE and MOA collaborations discovered the first planetary microlensing event, OGLE 2003-BLG-235 / MOA 2003-BLG-53 (Bond et al. 2004), which triggered the enthusiastic observations searching for planetary microlensing events.

2.2 Fundamental Theory

In this section, we review the basic equations for both single and binary lens microlensing.

2.2.1 Single Lens

Gravitational microlensing occurs when a star with a certain mass is almost perfectly aligned with the line of sight to a far behind source star. Figure 2.1 shows a schematic view of the microlensing. The light rays travelling from a source star at a distance of $D_{\rm S}$ are deflected by the lens, a star with a mass of $M_{\rm L}$ at a distance of $D_{\rm L}$. From the observer's viewpoint, two images of the source star can be seen. For the simplicity, we assume that the lens star is a point mass and the source star is a point source. With the lens geometry shown in Figure 2.1, we can get a

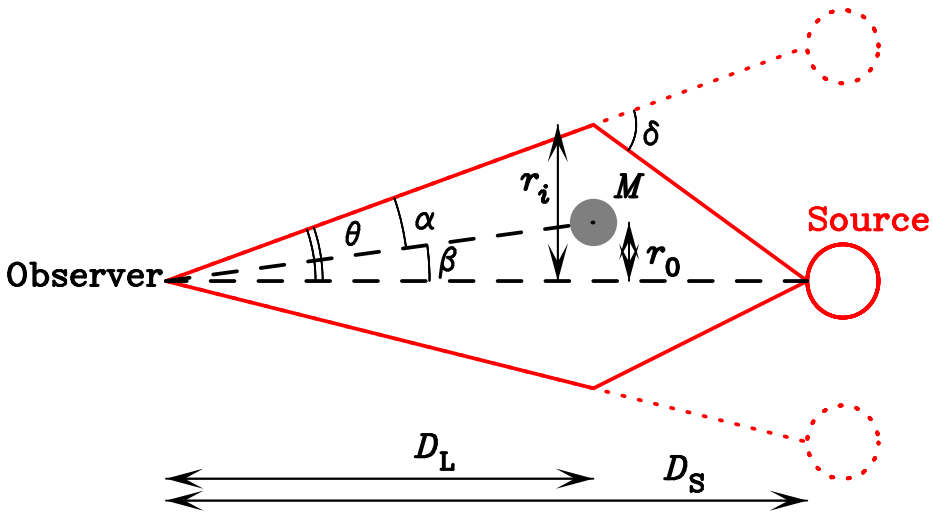

Figure 2.1: Schematic view of microlensing caused by a lens star with a mass of M at a distance $D_{\rm L}$.

simple equation,

$$D_{\rm S}\theta = (D_{\rm S} - D_{\rm L})\delta, \tag{2.1}$$

where θ is the angle between the source star and one of images and δ is the deflection angle, because the θ and δ are very small. The deflection angle for a light ray passing a mass, M, with an impact parameter, r, is derived from General Relativity as,

$$\delta = \frac{4GM}{c^2 r}, \tag{2.2}$$

where c is the light speed in the vacuum, G is the universal gravitational constant. With a relation,

$$D_{\rm L}\theta = r_i, \tag{2.3}$$

Equation (2.1) yields,

$$r_i = \frac{4GM}{c^2(r_i - r_0)} D_{\rm S} x(1-x), \quad x \equiv D_{\rm L}/D_{\rm S}\ . \tag{2.4}$$

If the lens star is perfectly aligned ($r_0 = 0$), the two images merge to form a ring of radius,

$$R_{\rm E} \equiv D_{\rm L}\theta_{\rm E} \equiv \sqrt{\frac{4GM}{c^2} D_{\rm S} x(1-x)} \tag{2.5}$$

$$\simeq 2.6\ {\rm AU} \left(\frac{M}{0.5\ M_\odot}\right)^{1/2} \left(\frac{D_{\rm S}}{8\ {\rm kpc}}\right)^{1/2} \left(\frac{x(1-x)}{0.2}\right)^{1/2} \tag{2.6}$$

known as a Einstein radius ($\theta_{\rm E}$ is an angular Einstein radius). Then, we can rewrite the lens equation

$$r_i = \frac{R_{\rm E}^2}{r_i - r_0} \tag{2.7}$$

which has two solutions,

$$r_i = \frac{r_0 \pm \sqrt{r_0^2 - 4R_{\rm E}^2}}{2}. \tag{2.8}$$

These images are difficult to be resolved because a typical angular Einstein radius is

$$\theta_{\rm E} \simeq 391\ \mu{\rm as} \left(\frac{M}{0.5\ M_\odot}\right)^{1/2} \left(\frac{D_{\rm S}}{8\ {\rm kpc}}\right)^{-1/2} \left(\frac{(1-x)/x}{0.3}\right)^{1/2}. \tag{2.9}$$

The lensed images are distorted and also magnified. Because surface brightness is conserved, and the observed flux from an image is just the surface brightness integrated over the image area, the observed magnification can be written by differentiating Equation (2.8),

$$A_i = \left|\frac{r_i}{r_0}\frac{dr_i}{dr_0}\right| = \left|\frac{r_i^4}{r_i^4 - R_{\rm E}^4}\right|, \quad i = 1, 2\ . \tag{2.10}$$

Then the total magnification is a sum of the each magnification as,

$$A = A_1 + A_2 = \frac{u^2+2}{u\sqrt{u^2+4}}, \quad u \equiv \frac{r_0}{R_{\rm E}} = \frac{\beta}{\theta_{\rm E}}, \tag{2.11}$$

where u is the normalized lens-source separation. So, the magnification is approximately, $A \simeq u^{-1}$ for $u \ll 1$, and $A \simeq 1$ for $u \gg 1$.

Actually, u depends on time, and so does A. Let's assume that the source, lens and observer are moving inertially. We can describe the time-dependent lens-source separation as

$$u(t) = \sqrt{u_0^2 + \left(\frac{t - t_0}{t_{\rm E}}\right)^2}, \quad t_{\rm E} = \frac{R_{\rm E}}{v_\perp}, \tag{2.12}$$

where u_0 is the minimum impact parameter, $v_\perp$ is the transverse velocity, and $t_{\rm E}$ is the crossing time on the Einstein radius, also called the event timescale. Combining this with Equation (2.11), the time-dependent magnification is described as,

$$A(t) = \frac{y^2 + u_0^2 + 2}{\sqrt{y^2+u_0^2}\sqrt{y^2+u_0^2+4}}, \quad y \equiv \frac{t - t_0}{t_{\rm E}}. \tag{2.13}$$

In Figure 2.2, we can see the $A(t)$ for the various u_0, and the lensed images for $u_0 = 0.2$. Therefore, microlensing experiment is the observation of a light curve,

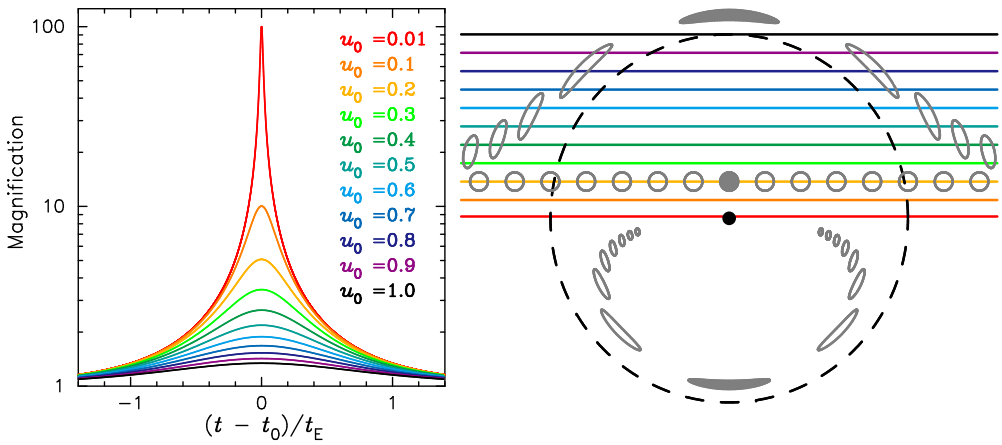

Figure 2.2: Theoretical microlensing light curve (left) and geometry of the lens plane seen from the observer (right). The difference in the color indicates difference in the impact parameter, u_0. With smaller impact parameter, the magnification becomes higher. In the right figure, the black dot and black dashed circle show the lens star and the Einstein ring, respectively. The positions of the source star with $u_0 = 0.2$ and created images are plotted in the gray circles and ellipses, respectively. The images out side and in side of the Einstein ring are called as major and minor images, respectively.

the time-dependent magnification of the source star. The typical event timescale is

$$t_{\rm E} \simeq 22 \text{ days} \left(\frac{M}{0.5\ M_\odot}\right)^{1/2} \left(\frac{D_{\rm S}}{8 \text{ kpc}}\right)^{1/2} \left(\frac{x(1-x)}{0.2}\right)^{1/2} \left(\frac{v_\perp}{200 \text{ km s}^{-1}}\right)^{-1}. \quad (2.14)$$

Note that $t_{\rm E}$ is proportional to the square root of M, and the lens mass, distance to the lens, and the transverse velocity degenerate in $t_{\rm E}$, assuming the source is at the Galactic center.

2.2.2 Binary Lens

In the Galaxy, about half of the stars are binary stars. And the star with a planet is thought of as a binary system with a small mass ratio. We can have a lens equation for the binary system along with the basis in Section 2.2.1. Let's assume the each lens is a point mass and the source is a point source. In the case of binary lens, the lens system may have a width along with the line of sight to the source star, but this can be negligible compared to $D_{\rm L}$ and $D_{\rm S}$. Here, we introduce a dimensionless vector for the source position $\boldsymbol{u} \equiv \boldsymbol{\beta}/\theta_{\rm E}$, and for the image positions

$\boldsymbol{y} \equiv \boldsymbol{\theta}/\theta_{\rm E}$. The lens equation is derived as,

$$\boldsymbol{u} = \boldsymbol{y} - \sum_{i=1}^{2} \epsilon_i \frac{\boldsymbol{y} - \boldsymbol{y}_{m,i}}{|\boldsymbol{y} - \boldsymbol{y}_{m,i}|^2}, \quad \epsilon \equiv \frac{m_i}{\sum_{i=1}^{2} m_i}, \tag{2.15}$$

where m_i and $\boldsymbol{y}_{m,i}$ are the mass and position of ith lens, respectively. This lens equation (2.15) can be thought of as the mapping from the source position to the image position, $\boldsymbol{u} \rightarrow \boldsymbol{y}$. Then, the magnification of jth image is written as the inverse of the Jacobian,

$$A_j = \frac{1}{\det\ J}, \quad J = \left(\frac{\delta \boldsymbol{u}}{\delta \boldsymbol{y}_j} \right). \tag{2.16}$$

The number of images for the binary lens is 3 or 5 depending on the each lens position and source position. Actually, Equation (2.15) can be expanded into a fifth order polynomial equation in $\boldsymbol{y}$, which can be solved numerically, and this equation has 3 or 5 real solutions (Witt 1990, Rhie 1997).

As we know from Equation (2.16), the magnification can be infinity if det $J = 0$. Although, it dose not become infinity because the source has a finite size in practice. The source position at which the magnification would be infinity is called caustic. The set of locations where the caustics are mapped in the lens plane by the lens equation is called critical curve. For the case of single lens, the caustic is the location of $u = 0$, and the critical curve corresponds to the Einstein ring. The caustics are important locations because not only the magnification of a point source diverge to infinity, but also the caustics on a magnification map, which shows the source magnification of each location on the sky , help us to understand the complex light curve for the binary lens.

Figure 2.3 shows the examples of magnification maps and caustics for the binary lenses with source trajectories, and corresponding light curves. The caustics are characterized by a cusp, which has a convex shape, and a fold, which has a concave curve. The size, shape and location of the caustics are determined by a mass ratio $q = M_2/M_1$, where M_1 is the primary star mass and M_2 is the companion's mass, and a separation s between the lens components in units of the angular Einstein ring radius. We can see one to three sets of caustic depending on q and s. If $s < 1$, there are three sets of caustic (The top panel in Figure 2.3). A caustic close to the center of the lens mass, which is at $(x, y) = (0, 0)$, is called a central caustic, and the other two are called planetary caustics, which are located on the opposite side of the center of mass from the companion. If $s > 1$, there are two sets of caustic (The bottom panel in Figure 2.3). The one is a central caustic and the other is a planetary caustic, which is located on the same side with the companion. If $s \simeq 1$, the central caustic and planetary caustics marge to form a

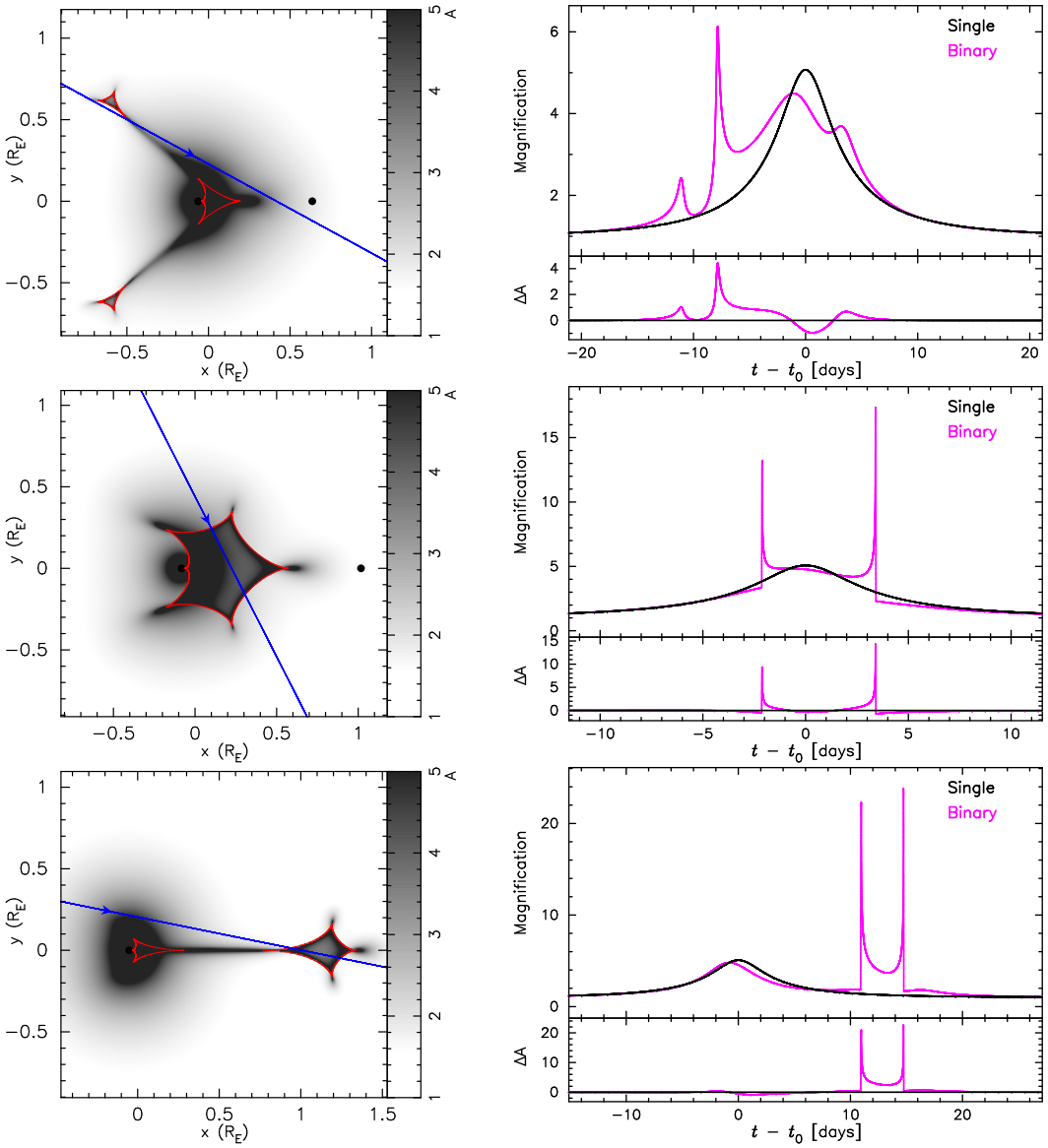

Figure 2.3: Magnification maps and light curves of binary microlensing with a mass ratio of $q = 10^{-1}$, and various separations s. The separations are 0.7, 1.1 and 1.75 from the top to bottom. Left panels show the magnification map where the magnification is drawn in gray scale, the caustics are plotted in red, and the source trajectories and directions are plotted in the blue lines and arrows. The x, y coordinates are scaled by the angular Einstein radius, and the origin is the barycenter. The magenta light curves in the right panels are corresponding to the cross-section along with the source trajectories of the left figures. The black light curves indicate the magnification for the single lens model with same $t_{\rm E}$ as that in the binary model at the position of primary. The bottom insets in each right panel show the residuals of the two light curves.

large resonant caustic. In general, the size of the central caustics is $\propto q$, and the size of the planetary caustics is $\propto \sqrt{q}$ (Chung et al. 2005, Han 2006). And the size of the caustics shrinks if $|s-1|$ becomes larger. Therefore, the smaller planets or the planets located away from the Einstein ring radius generate smaller caustics. The boundaries between the resonant caustic and the planetary caustics on an s - q plane are plotted in Figure 2.4 (Cassan 2008).

The cross-section of the trajectory on the magnification map corresponds to a light curve for the binary lens as drawn in Figure 2.3. When a point source approaches to the cusps, the magnification increases sharply. But, for the fold caustics, the magnification pattern is similar to that of the single lens when the source is out side of the caustics. And, the magnification increases suddenly just when the source goes into the fold caustics. This is because the number of images is three outside of the caustics, but five images emerge inside the caustics.

Whenever the number of the lens is more than two, caustics should exist. Therefore, if we could see the caustic crossing or approaching feature in the observed light curve, this promises that the lens consists of two or more mass points. This is what we are looking for to discover planets by microlensing. Phenomenology for the caustics and light curves for the planetary companion is explained in Section 2.3.

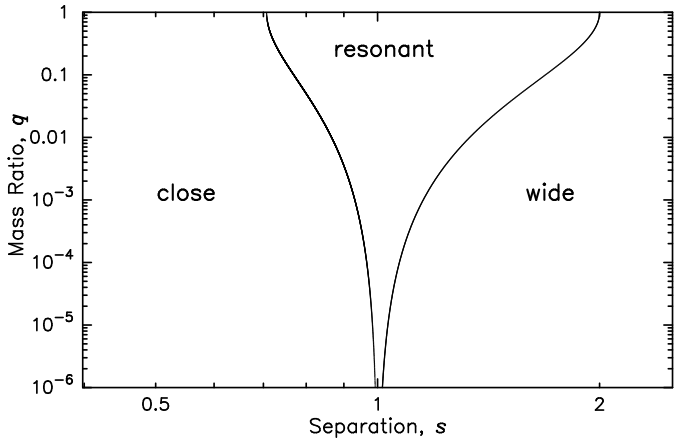

Figure 2.4: Caustic shapes depending on s and q. The close and wide boundaries are plotted with $s^8 = (1+q)^2(1-s^4)^3/27q$ and $s^2 = (1+q^{1/3})^3/(1+q)$, respectively (Cassan 2008).

2.2.3 Optical Depth and Event Rate

Microlensing is a accidental phenomenon where a lens star is aligned to the line of sight to the behind source star. If the surface density of the source star and the

density of the lens star are higher, we can expect the probability of the alignment will be higher. So, the density of the lens star can be estimated from the microlensig observation. Here, we define the optical depth τ, the probability that any given star is being lensed at any given time by a foreground lens object. In general, a given source star is defined to be lensed when it is located within the angular Einstein ring radius, where $A \geq 1.34$. Then the optical depth is the number of lens stars within the microlesing tube that is a tube with a radius of the Einstein ring $R_{\rm E}$. The number of stars in a volume of $\pi R_{\rm E}^2 \times {\rm d}D_{\rm L}$ is $n\pi R_{\rm E}^2 {\rm d}D_{\rm L}$, where n is the number density of lenses. Integrating this yields,

$$\tau = \int_0^{D_{\rm S}} n\pi R_{\rm E}^2 {\rm d}D_{\rm L} \tag{2.17}$$

$$= \frac{4\pi G D_{\rm S}^2}{c^2} \int_0^1 \rho(x) x(1-x) {\rm d}x, \quad \rho = n/M, \tag{2.18}$$

where ρ is the mass density along the line of sight, and we used the relation $x = D_{\rm L}/D_{\rm S}$. Because $n \propto M^{-1}$ and $R_{\rm E}^2 \propto M$, the optical depth depends only on the mass density along the line of sight and not on the mass function of lenses. Many theoretical (Kiraga & Paczyński 1994, Han & Gould 1995) and observational (Popowski et al. 2005, Sumi et al. 2006) works estimated τ towards the Galactic bulge. The latest observational result Sumi et al. (2013) gives $\tau \sim 4 \times 10^{-6}$. Although this result is factor ~ 10 larger than the first prediction of $\tau \sim 5 \times 10^{-7}$ with the symmetric bulge by Paczyński (1991) and Griest et al. (1991), the revised estimate with the bar structure (Han & Gould 2003, Wood & Mao 2005, Kerins et al. 2009) are consistent with Sumi et al. (2013).

The probability of that a given source star is magnified by a foreground lens star is defined as an event rate, Γ. If we assume that a lens star has a proper motion $v_{\rm rel}$ relative to a source star, the Einstein ring sweeps an area of $2R_{\rm E}v_{\rm rel}{\rm d}t$ in a time ${\rm d}t$. So, the probability of the given source star being microlensed by the lenses within $D_{\rm L} \sim D_{\rm L} + {\rm d}D_{\rm L}$ in a time ${\rm d}t$ is $n2R_{\rm E}v_{\rm rel}{\rm d}t{\rm d}D_{\rm L}$. Integrating this yields,

$$\Gamma {\rm d}t = \frac{2}{\pi}\frac{{\rm d}t}{t_{\rm E}} \int_0^{D_{\rm S}} n\pi R_{\rm E}^2 {\rm d}D_{\rm L}, \tag{2.19}$$

where we used $v_{\rm rel} = R_{\rm E}/t_{\rm E}$. Therefore, the event rate is written as,

$$\Gamma = \frac{2}{\pi}\frac{\tau}{t_{\rm E}}. \tag{2.20}$$

If we assume that the optical depth is $\tau \sim 1 \times 10^{-6}$, the event rate is $\Gamma \sim 1 \times 10^{-5}$ yr^{-1} because the typical event timescale $t_{\rm E}$ for the Galactic Bulge is ~ 20 days. So we can expect 500 microlensing events yr^{-1} toward the Galactic Bulge if we

observe tens of millions of stars. Actually, MOA-II (Bond et al. 2001, Sumi et al. 2003) observes such number of stars and finds $500 \sim 600$ microlensing events every year. Sumi et al. (2013) found that the event rate around the Galactic coordinate $(l, b) = (0°.97, -2°.26)$ is $\Gamma = 4.57^{+0.51}_{-0.46} \times 10^{-5}$ yr^{-1}, which is higher than the even rate at $l \approx 0°$ for the same Galactic latitude.

2.3 Planetary Microlensing

A planetary microlensing is thought of as the binary lens with an extreme small mass ratio. As we see Section 2.2.2, if the lens is a planetary system, the caustics should exist on the sky. We can see the deviation from the light curve of a single lens, if the source trajectory crosses or passes close to the caustics. This deviation, an anomaly in the light curve, occurs in shorter time and has smaller amplitude compared to the anomaly arisen from the stellar binary lenses, because the size of the caustics for a smaller mass ratio is smaller. The smaller caustics take a short time for the source star to cross them. Also, the actual source star has a finite source size, so the deviation by the caustics in the light curve could be washed out, or negligible for a large size of the source star.

Figure 2.5 shows magnification maps and the light curves for the planetary microlensing with a mass ratio of $q = 10^{-3}$ and various separations s, and finite source sizes $\rho = \theta_*/\theta_{\rm E}$, where θ_* is an angular source star radius. Figure 2.6 shows similar figures, but with a mass ratio of $q = 10^{-5}$. Compared to the stellar binary mass ratio $q = 10^{-1}$ in Figure 2.3, we can see the size of caustics and perturbations in the light curve are smaller. The timescale for the perturbation is a few days, even if the source trajectories hit the caustics with a favorable angle. Also, due to the small size of caustics, the finite source size strongly affect the perturbation. For the giant source star with $\rho = 0.03$, the sharp anomaly are smoothed out. On the other hand, the large size of source star can sweep large area, so it has much chance of hitting the caustics. But if the lens has a mass ratio of $q = 10^{-5}$, which is 1 $M_\oplus$ if the primary mass is 0.3 $M_\odot$, the caustic sizes are too small to detect the perturbation with the large source star (See Figure 2.6). Especially, for the close configuration, $s < 1$, the perturbation is canceled out by the positive and negative magnifications. Therefore, to detect the anomaly by an Earth size planet, a main sequence star is preferred as a source star.

As described in Section 2.2.2, the central caustic shrinks with $\propto q$, and the plenary caustics shrink with $\propto \sqrt{q}$. So the central caustic size is much smaller for the planetary microlensing. The shape of the central caustic is same for s^{-1} and s (Chung et al. 2005, Han 2006). This is called close-wide degeneracy. Due to this degeneracy, we could not determine the separation uniquely, except for the special case (Shin et al. 2013). Nevertheless, the central caustic is always located

at the center of mass, and this yields a big chance of hitting the central caustic for the source trajectories close to the center of mass, a high-magnification event. So time of the anomaly can be predicted prior and easy to coordinate the intensive observation. Contrary, although we can not predict when the planetary caustic event occur, the event rate is higher due to the relatively large caustics. Thus, high cadence continuous survey is optimal for finding small planets. The detail properties of the central and planetary caustics are discussed in Chung et al. (2005) and Han (2006), and the discussion about the detection limit of small planets with various finite source size is written in Bennett (2008).

2.4 High Order Effects

The observable information on the lens system in the majority of microlensing events is only an event timescale, $t_{\rm E}$. As shown in Equation (2.14), the lens mass, M, the distance to the lens, $D_{\rm L}$, and the relative transverse velocity, $v_{\rm rel}$ degenerate in $t_{\rm E}$. These parameters could not be determined uniquely unless both finite source and parallax effect are detected in the light curve.

We define the finite size of the source star in unit of the angular Einstein ring radius as,

$$\rho = \theta_*/\theta_{\rm E}, \tag{2.21}$$

where θ_* is the angular source star radius. This effect is observed in the light curve, where the source star crosses the caustics or approaches the cusp closely, as seen in Figure 2.5 and 2.6. Even in the single lens event, the peak of the light curve is well perturbed by this effect if the source size is larger than the impact parameter, $\rho \geq u_0$, where the lens transits the source star (Choi et al. 2012). The angular source star radius θ_* can be empirically estimated from the source star color and magnitude (Kervella et al. 2004, Kervella and Fouqué 2008). Therefore, the detection of the finite source effect leads to $\theta_{\rm E}$, although we can not know $R_{\rm E}$ without the distance to the lens $D_{\rm L}$.

In Equation (2.12), we assumed that the source, lens and observer are moving inertially, but actually the Earth is orbiting about the Sun. If the event timescale $t_{\rm E}$ is longer, this orbital motion of the Earth can be seen in the light curve as a deviation. This is called miclolensing parallax. The parallax effect is also detectable if the Einstein ring radius projected on the observer plane $\tilde{r}_{\rm E}$ is comparable to the Earth's orbital size, 1 AU (Gould 2000).

As shown in Figure 2.7, we can have a relation

$$\delta = \frac{4GM}{R_{\rm E}c^2} = \frac{\tilde{r}_{\rm E}}{D_{\rm L}}. \tag{2.22}$$

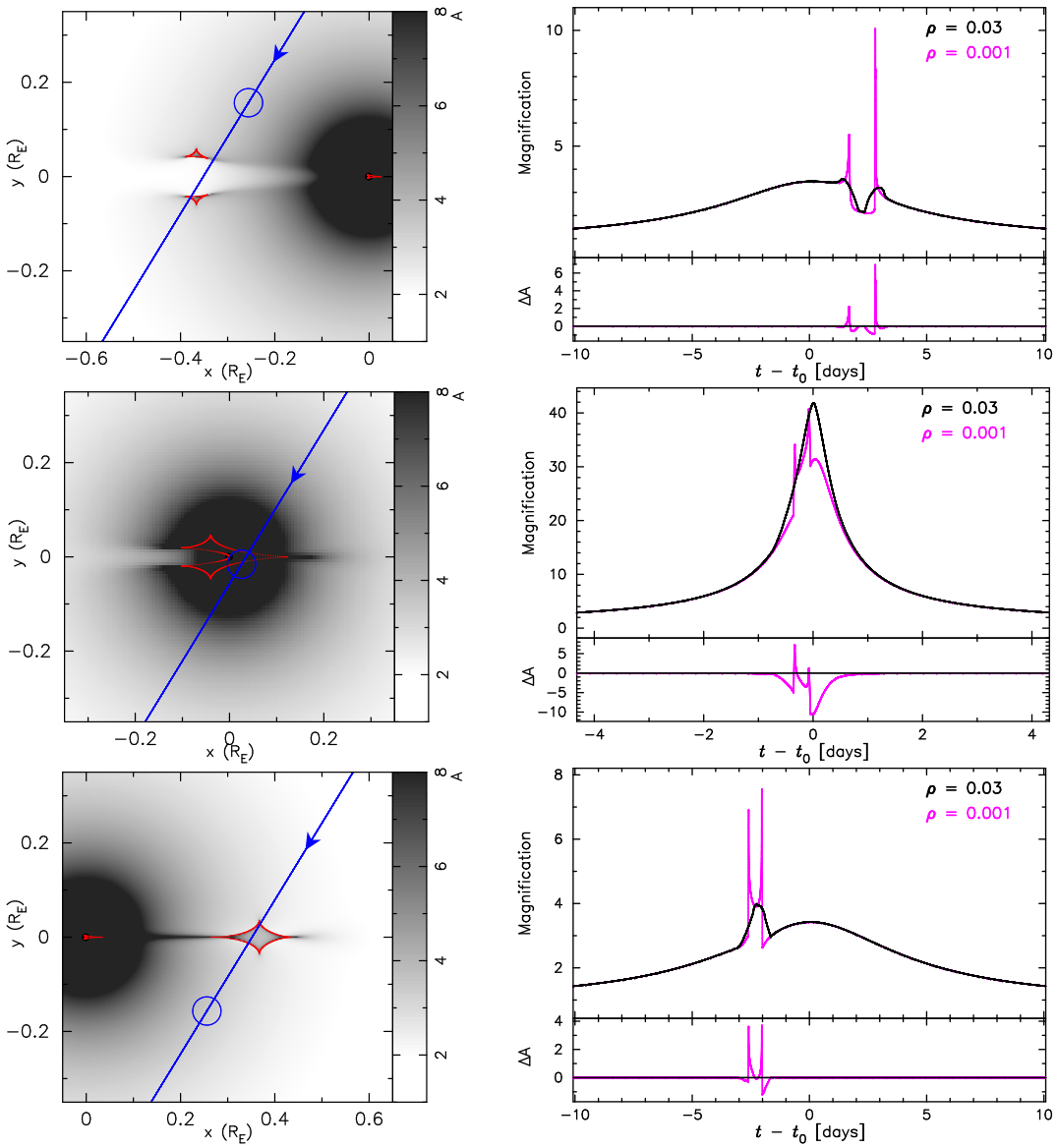

Figure 2.5: Magnification maps and light curves of planetary microlensing with a mass ratio of $q = 10^{-3}$, and various separations s and source sizes ρ in unit of the angular Einstein radius. The separations are 0.83, 0.98 and 1.2 from the top to bottom. Each left panel shows the magnification map where the magnification is drawn in gray scale, the caustics are plotted in red, and the source trajectories and directions are plotted in the blue lines and arrows. The blue circles show the source star sizes, $\rho = 0.03$ and 0.001 (The circles for $\rho = 0.001$ is too small to see). The light curves in the right panels are corresponding to the cross-section along with the source trajectories. The black and magenta lines indicate the large and small ρ, respectively. The bottom insets in each right panel show the residuals of the two light curves.

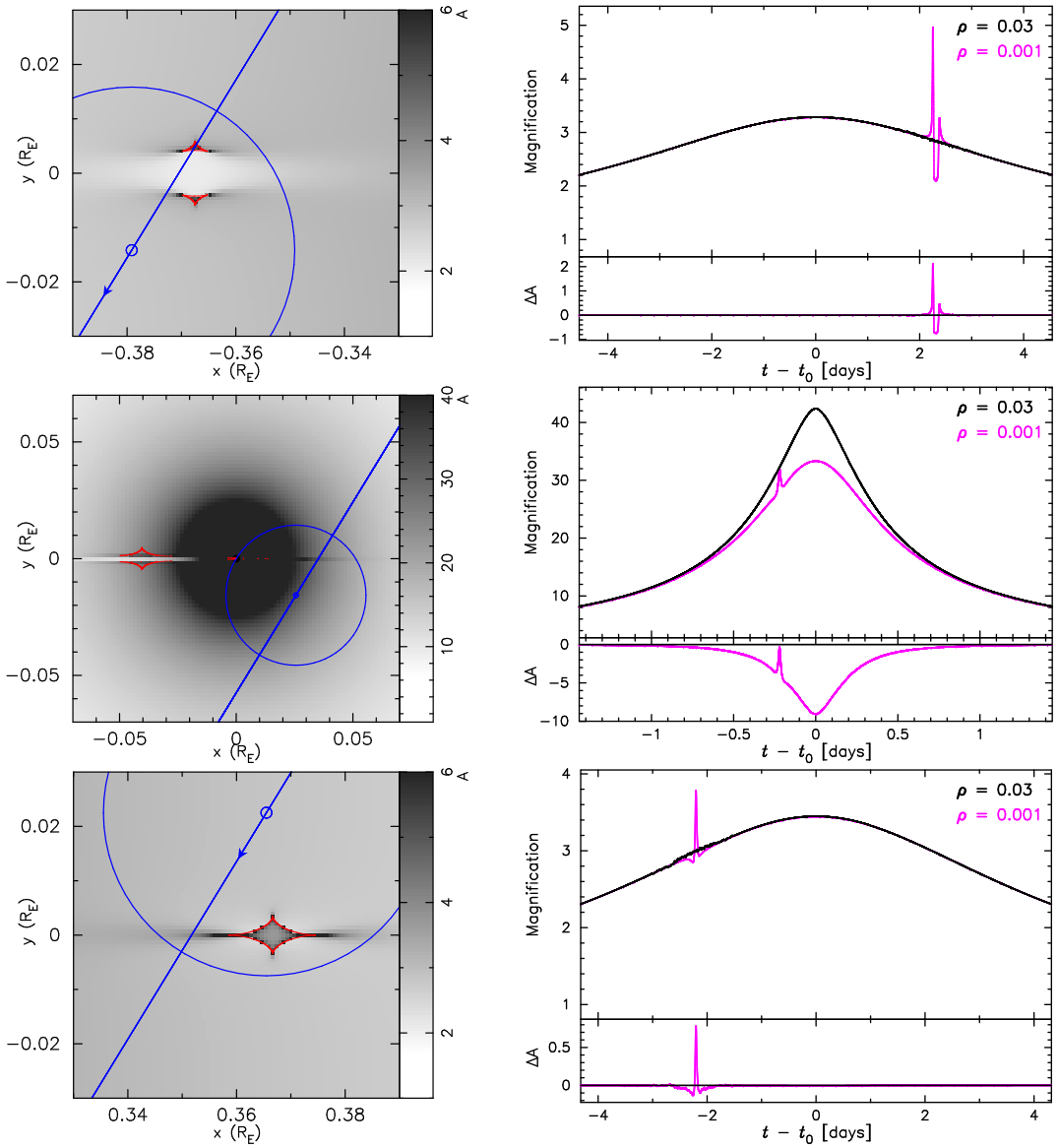

Figure 2.6: Same as Figure 2.5, but for a mass ratio of $q = 10^{-5}$, which is 1 $M_\oplus$ if the primary mass is 0.3 $M_\odot$.

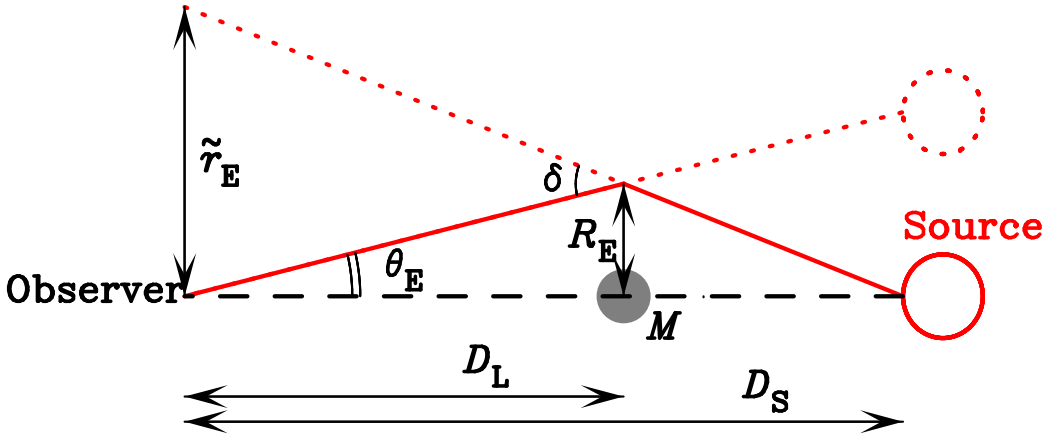

Figure 2.7: Schematic view of the projected Einstein ring on the observer plane.

This can be written as,

$$\tilde{r}_{\rm E} = D_{\rm rel}\theta_{\rm E}, \tag{2.23}$$

where $D_{\rm rel}^{-1} = D_{\rm L}^{-1} - D_{\rm S}^{-1}$. From the light curve fitting, we can derive the parallax vector as,

$$\boldsymbol{\pi}_{\rm E} = \boldsymbol{\pi}_{\rm rel}/\theta_{\rm E}, \quad \pi_{\rm rel} = \frac{\rm AU}{D_{\rm rel}}, \tag{2.24}$$

where $\boldsymbol{\pi}_{\rm E}$ has a direction of the lens-source proper motion. Then we can get a relation, $\pi_{\rm E} = {\rm AU}/\tilde{r}_{\rm E}$. Therefore, if both finite source and microlensing parallax effect are detected, the observables, $\theta_{\rm E}$ and $\pi_{\rm E}$ yield a lens mass as,

$$M = \frac{1}{\kappa}\frac{\theta_{\rm E}}{\pi_{\rm E}}M_\odot, \quad \kappa \equiv \frac{4GM_\odot}{c^2{\rm AU}} = 8.14 \text{ mas}. \tag{2.25}$$

With an assumption of the distance to the source star, the distance to the lens $D_{\rm L}$ and the transverse velocity $v_\perp$ are also determined uniquely. Note that this method can derive the mass of the lens system directly without the mass-luminosity relation.

Even if the projected Einstein ring radius on the observer plane is too large, we can detect the parallax effect with the long baseline, i.e., the ground based observation combined with the observation from the space craft. Actually, the observation from a space craft, *EPOXI* was conducted to detect the parallax effect for the planetary event MOA-2009-BLG-266 (Muraki et al. 2011). Although the very special case, the observations from distant telescopes on the different continent could detect the parallax effect (Gould et al. 2009). Unless the secure parallax effect is detected, we use a Bayesian analysis with the constraints from upper limit

of the parallax effect or flux from the lens star to estimate the physical property of the lens system.

2.5 Practical Application

As mentioned before, microlensing events are rare, and the planetary signals are observed as a short term anomaly in light curves. Thus, the microlensing method requires the monitoring many stars with high cadence of ten or more times per night. To overcome the difficulties in the detections of planetary signals, Gould & Loeb (1992) proposed a observational strategy that consists of two stages. In the first stage, the survey telescopes with wide field of view (FOV) camera search for mirolensing events and alert the candidates before the peak of magnification. Then, as the second stage, the follow-up telescopes with small FOV monitor the alerted candidates with high cadency. This strategy was adopted due to the limited number of telescopes. Actually, this strategy is successful especially for high-magnification events, where the peak magnification reaches $A_{\rm max} \gtrsim 100$, and it is still being undertaken nowadays. In the high-magnification events, if a planet exists around the Einstein ring radius, the light curve could be perturbed by the central caustic around the peak because the source trajectory passes very close to the primary star ($u \simeq 1/A_{\rm max} \lesssim 1/100$). Because the time of the peak magnification is expected before the peak by fitting the light curve, monitoring only the peak of the events can yield the detection of the anomaly. Also, the highly magnified source star is good for the small aperture telescopes. Thus, this survey plus follow-up strategy (first generation microlensing survey) is used for the limited telescopes.

If the survey telescopes with wide FOV are able to detect a number of microlensing events with high cadence, the planetary signal will be discovered by the survey telescopes alone. In this strategy, second generation of survey only mode, the planets will be discovered mainly through the low-magnification channel. In the low magnification events, we can not expect when the planetary anomaly happens. Therefore, round-the-clock observations with the large telescopes located at different longitude are required for the second generation survey. Such a high cadence survey started for the first time with the MOA collaboration by using the dedicated 1.8 m MOA-II telescope with 2.2 deg^2 FOV in New Zealand (Sako et al. 2008). The OGLE collaboration started the high cadence survey with their upgraded 1.3 m telescope with 1.4 deg^2 FOV in Chile. In addition to these telescopes, the Wise microlensing survey has started high cadence observations using 1.0 deg^2 CCD mosaic camera on the 1.0 m Wise telescope in Israel (Shvartzvald & Maoz 2012). Finally, the Korean Microlensing Telescope Network (KMTNet) (Kim et al. 2010) is funded to increase the longitude coverage of microlensing survey telescopes. Their plan is to construct three 1.6 m telescopes with 4.0 deg^2

FOV cameras in South Africa, South America and Australia. The second generation microlensing survey will be perfectly achieved, and the microlensing planet discovery rate will dramatically increase when their telescopes come online.

Although the second generation microlensing survey with ground-based telescopes will demonstrate the great improvement in the planet discoveries, the ultimate microlensing survey is the observation from space-based telescope. The space-based microlensing survey has a lot of advantages in many ways (Bennett & Rhie 2002). Actually, the Wide-Field InfraRed Survey Telescope (Green et al. 2012:WFIRST) has been proposed and selected as the top priority for a large space mission in the 2010 Astronomy and Astrophysics Decadal Survey. Such a survey has a sensitivity for all the planets analogous to our solar system except for the Mercury. Combining the transit survey results from *Kepler*, which is sensitive to close-in planets, the space-based microlensing survey will complete the planet distribution map on the separation-mass plane.

Chapter 3

The MOA Project

Gravitational microlensing method needs to survey observations toward the dense field with high cadence imaging because the microlensing phenomena is very rare and the planetary signal occurs within short term. Nowadays, microlensing events are detected by the two main survey groups, the Microlensing Observations in Astrophysics (MOA; Bond et al. 2001, Sumi et al. 2003), and the Optical Gravitational Lensing Experiment (OGLE; Udalski 2003). In this Chapter, we focus on the MOA collaboration and introduce the instruments and survey observation. Finally, we summarize the discovery of the planetary microlensing events so far, to which the MOA collaboration contributes.

3.1 The MOA collaboration

Originally, MOA has started in 1995 (Muraki et al. 1999) as a Japan and New Zealand collaboration to search for microlensing events caused by massive compact halo objects (MACHOs) in the halo of our galaxy. At that time, the MOA collaboration used a 61 cm Boller & Chivens telescope to observe the LMC, SMC and GB at Mt. John University Observatory (MJUO) in New Zealand (Figure 3.1). MJUO is located at latitude 43° 59′.2 south, longitude 170° 27′.9 east, which is the southernmost observatory except for Antarctic. This makes it possible to observe the GB longer through a year and the LMC and SMC a whole year. After the first detection of a planetary microlensing events (Bond et al. 2004), the survey target has been shifted from searching for MACHOs to hunting exoplanets. To investigate the MACHOs fraction to the dark matter further and discover more planets efficiently, a new telescope equipped with a wide field-of-view CCD camera were constructed in 2004, with which a new generation of microlensing survey has started.

Figure 3.1: Mt. John University Observatory.

3.2 Instruments

Currently, the MOA survey uses the 1.8 m MOA-II telescope with 2.2 deg^2 field-of-view (FOV) CCD camera, MOA-cam3 at (Sako et al. 2008). The MOA-cam3 mounted on the focal plane consists of ten E2V CCD4482 chips. Each chip has 2 k $\times$ 4 k pixels and the pixel size is 15 μm, yielding 0.58 arcsec pixel^{-1}. Figure 3.2 and Figure 3.3 show the MOA-II telescope and MOA-cam3, respectively.

The main sequence stars in the Galactic Bulge, which is the observational fields to search for planets, receive the extinction from the interstellar dust. These stars are our major targets, therefore the custom wide-band MOA-Red filter, which is roughly the sum of the Cousins R- and I-bands, is prepared for an effective microlensing survey. Bessell V, I filters are also prepared. Microleisng phenomenon does not depend on the wavelength, so observing the light curve with different filter is one of methods to discriminate a microlesing event from other variable stars. Also, the angular radius of the source star could be estimated with the color of the source star. The angular Einstein radius, which is a key physical value of the lens object, is estimated from the angular radius if the finite source effect is detected, the light curve with different color is important. But, the mechanism that change the filters automatically has a problem and a manual change of the filters takes a few dozen minutes, which lose the observing time. As a result, the most of the

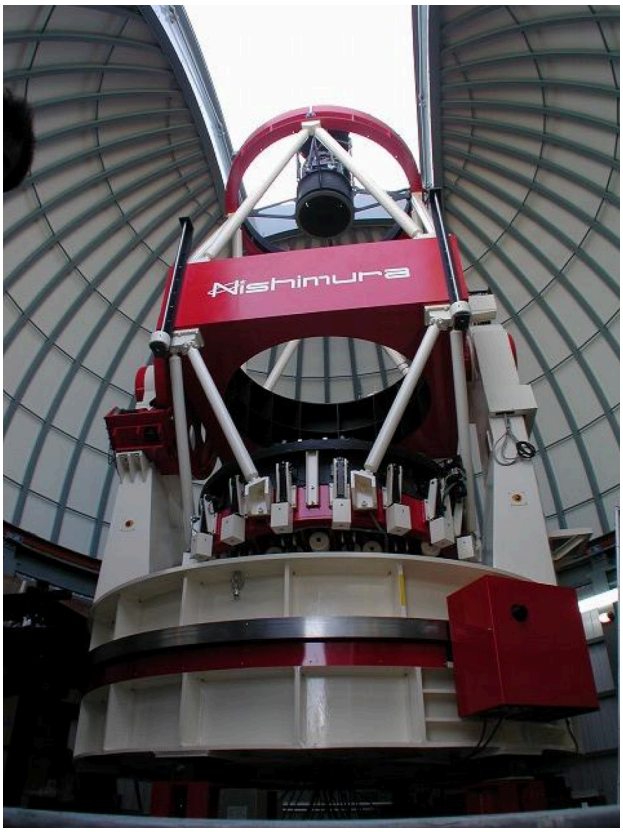

Figure 3.2: MOA-II telescope.

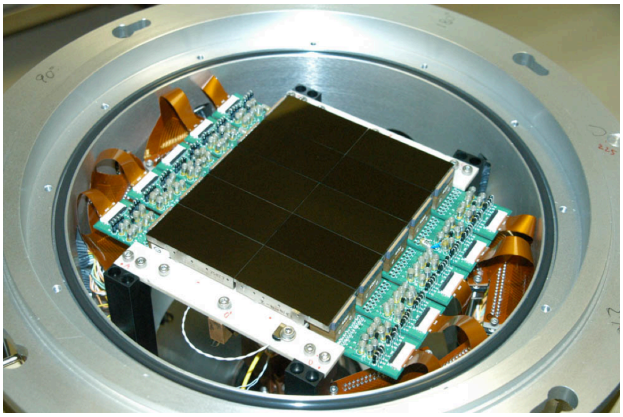

Figure 3.3: MOA-cam3.

survey data are taken with MOA-Red and the color information of stars is prone to rely on the data from other telescopes. Figure 3.4 shows the transmittance of these filters.

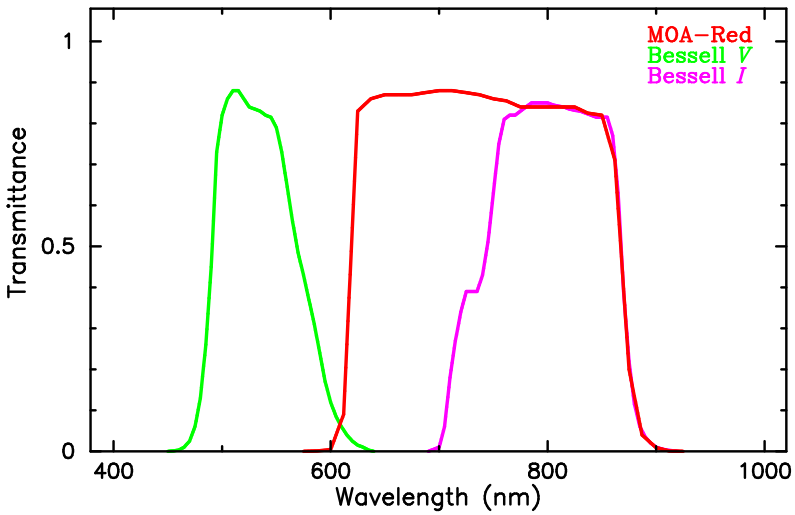

Figure 3.4: Transmittance of MOA-Red, Bessell V and Bessell I.

3.3 Observations

MOA-II observes the Galactic Bulge with very wide FOV to search for microlensing events. The frequency of the imaging is high to detect a short time anomaly in the light curve of microlensing. Figure 3.5 and Table 3.1 show the observation fields and the coordinates of the each field. The observation area that consists of 22 fields covers about 42 deg^2 between $-5^\circ < l < 10^\circ$ and $-7^\circ < b < 1^\circ$. Until 2008, gb5 and gb9 were observed once per 10 minutes, and the other fields are observed once per 1 hr. After optimization of the observation strategy, since 2009, gb3, gb4, gb5, gb9 and gb10 are observed once per 15 minutes, gb1, gb2, gb8, gb13, gb17 and gb18 are observed once per 47 minutes, and the other fields are observed once per 95 minutes, except for gb6 and gb22 which are observed once per night. The observation frequency is assigned such that even MOA-II data alone can detect the anomaly caused by an Earth mass planet, Neptune mass planet and Jupiter mass planet in the field observed once per 15 minutes, 47 minutes and 95minutes, respectively.

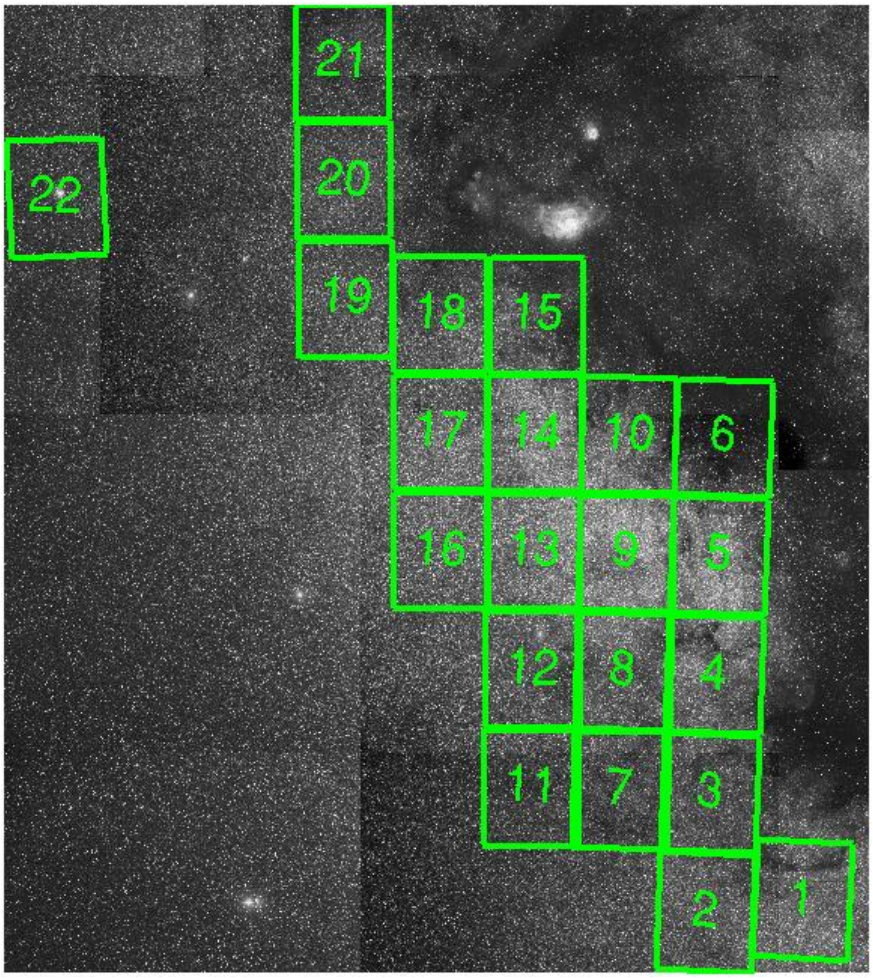

Figure 3.5: Observation fields by MOA-II.

Table 3.1: Equatorial Coordinate for MOA-II Observation Fields

Field	R.A.(J2000)	Decl.(J2000)
gb1	17 47 30.0	-34 15 00
gb2	17 54 00.0	-34 30 00
gb3	17 54 00.0	-32 45 00
gb4	17 54 00.0	-31 00 00
gb5	17 54 00.0	-29 15 00
gb6	17 54 00.0	-27 30 00
gb7	18 00 00.0	-32 45 00
gb8	18 00 00.0	-31 00 00
gb9	18 00 00.0	-29 15 00
gb10	18 00 00.0	-27 30 00
gb11	18 06 00.0	-32 45 00
gb12	18 06 00.0	-31 00 00
gb13	18 06 00.0	-29 15 00
gb14	18 06 00.0	-27 30 00
gb15	18 06 00.0	-25 45 00
gb16	18 12 00.0	-29 15 00
gb17	18 12 00.0	-27 30 00
gb18	18 12 00.0	-25 45 00
gb19	18 18 00.0	-25 30 00
gb20	18 18 00.0	-23 45 00
gb21	18 18 00.0	-22 00 00
gb22	18 36 24.0	-23 54 00

3.4 Alert System

Once a microlensing event is found, the event is alerted by email and uploaded to the MOA alert pages (https://it019909.massey.ac.nz/moa/), which is updated almost real time. The follow-up groups check the alert and decide which events they should observe depending on their criteria. Table 3.2 shows the number of the alerted events by MOA. The fluctuation of the number of the alerted events could be partially explained by the Poisson probability, but the trend of increase can be explained by the improvement of the detection criteria and skill of the observer. The criteria for detecting and alerting the microlensing events is not same level all the time because the procedure is not automatic perfectly. Actually, the MOA observers check a lot of candidate events for microlensing in real time. The skill and technique for selecting microlesning events from the thousand of the candidates have been improved. The candidates including many types of variable objects are picked up by the developed software, where the criteria is optimized before every winter season in the Southern Hemisphere starts. Nevertheless, there could be events which fail to be found and alerted by the criteria and observer. But these events should be found in the off line analysis (Sumi et al. 2011, Bennett et al. 2012).

The alerted microlensing events are a little contaminated by the other type of variable objects such as cataclysmic variable stars (CV), periodic variable stars and asteroids, which mimic the light curve of microlensing events. The systematic variation of the brightness caused by the different refraction of atmosphere or the change of seeing could mimic the microlensing light curve. These objects are hard to reject when the events are alerted, because the alert should be issued earlier to inform the follow-up groups of the possible anomaly in the microlensing light curve. Also, in order to detect a short time event that is a candidate of a free-floating planet event (Sumi et al. 2011), an earlier alert is necessary. However, these false events can be classified later by the investigation of the light curve with more data points in the baseline.

3.5 Systematic Modeling

Some planetary events were identified in a systematic modeling of all the anomalous events (i.e. those not well fit by a point source, single lens model without microlensing parallax) from the MOA alert pages from the 2007–2012 seasons. A similar analysis of OGLE-III binary events was conducted by Jaroszyński et al. (2010). The light curve calculations for this systematic analysis were done using the image centered ray-shooting method (Bennett & Rhie 1996, Bennett 2010). All the events that have anomalous deviation from a point source, single lens

Table 3.2: The Number of the Alerted Microlensing Events by MOA

Year	Number of Alerted Events
2006	168
2007	488
2008	477
2009	563
2010	607
2011	485
2012	680
2013	668

model were fitted with the binary lens model according to the following procedure. Binary lens models have three parameters that are in common with single lens models. These parameters are the time of the closest approach to the lens system center of mass t_0, the Einstein radius crossing time, $t_{\rm E}$, and the impact parameter u_0, in units of the angular Einstein radius $\theta_{\rm E}$. Binary lens models also require three additional parameters. These are the lens system planet-star mass ratio, q, the planet-star separation, s, projected into the plane perpendicular to the line-of-sight, and the angle of the source trajectory relative to the binary lens axis α. Another parameter, the source radius crossing time, t_* is also included in the binary lens model because this parameter is important for most of planetary microlensing light curves. We carefully searched to find the best fit binary lens model over a wide range of values of microlensing parameters using a variation of the Markov Chain Monte Carlo (MCMC) algorithm (Verde et al. 2003). Because the shape of anomaly features in the light curve well depends on q, s and α, these three parameters are fixed in the first search. Next, we searched χ^2 minima of the 100 models in order of χ^2 in the first search with each parameter free and found the best fit model.

Chapter 4

MOA-2008-BLG-379Lb: A Massive Planet Orbiting a Late Type Star beyond the Snow Line

A microlensing event, MOA-2008-BLG-379 was found to be a candidate of a planetary microlensing event for the first time after the systematic modeling of all the anomalous events. The detail analysis with re-reduced dataset yields that the lens system consists of a host star with mass of $M_{\rm L} = 0.56\ M_{\odot}$ orbited by a planet with mass of $m_{\rm P} = 4.1\ M_{\rm Jup}$ at an orbital separation of $a = 3.3$ AU. In this Chapter, the data reduction, light curve analysis, and Bayesian analysis for MOA-2008-BLG-379 will be discribed.

4.1 Observations and Data Reduction

4.1.1 Discovery of MOA-2008-BLG-379 / OGLE-2008-BLG-570

Prior to 2009, the MOA-II observing strategy called for the observations of the two fields with the highest lensing rate every 10 minutes and observations of the remaining 20 fields every hour using the custom wide-band MOA-Red filter, which is roughly the sum of the Cousins R- and I-bands. MOA-2008-BLG-379 was discovered in field gb8, which was observed with an hourly cadence in 2006–2008.

The microlensing event MOA-2008-BLG-379 was identified by the MOA alert system (Bond et al. 2001) at (R.A., decl.)(J2000) = ($17^{\rm h}58^{\rm m}49^{\rm s}.44$, -30°11′48″.95), and was announced by the MOA collaboration at UT 22:00, 2008 August 9, (or HJD′ = 4688.42). Figure 4.1 shows the images of MOA-2008-BLG-379 taken by MOA-II. As can be seen from the light curve in Figure 4.2, this was after the first

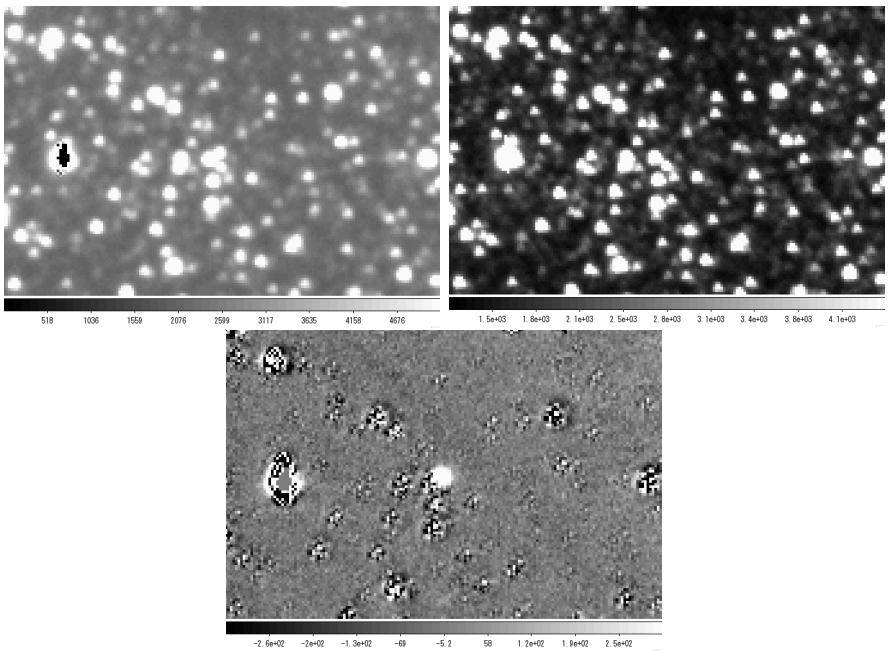

Figure 4.1: MOA-II images for MOA-2008-BLG-379. The top left image shows epoch HJD′ ∼ 4688 and the top right is the MOA reference image. The bottom image shows the difference image produced by the subtraction of the reference image from the top left image. East is up and North is to the right.

caustic entrance and exit and the central cusp approach feature. Given the sparse coverage and lack of OGLE data at this time, it was not immediately obvious that this event was anomalous. Two weeks later, at UT 20:00 2008 August 23, the event was also identified and announced by the OGLE Early Warning System (EWS; Udalski et al. 1994) as OGLE-2008-BLG-570. The delay in the identification of this event by OGLE was due to the fact that the source was faint and was not located close to the location of a "star" that was identified in the OGLE reference image in Figure 4.3. This is fairly common, as most bulge main sequence stars are not individually resolved at $\sim 1''$ resolution. The source star, MOA-2008-BLG-379S, happens to be located at an unusually large distance from the nearest star in the OGLE catalog, and as a result, it could only be found via the "new object" channel of the OGLE EWS. In 2008 this channel was not run as often as the regular "resolved star" channel of the OGLE EWS. As a result, both the MOA and OGLE collaboration groups observed this event with normal cadence.

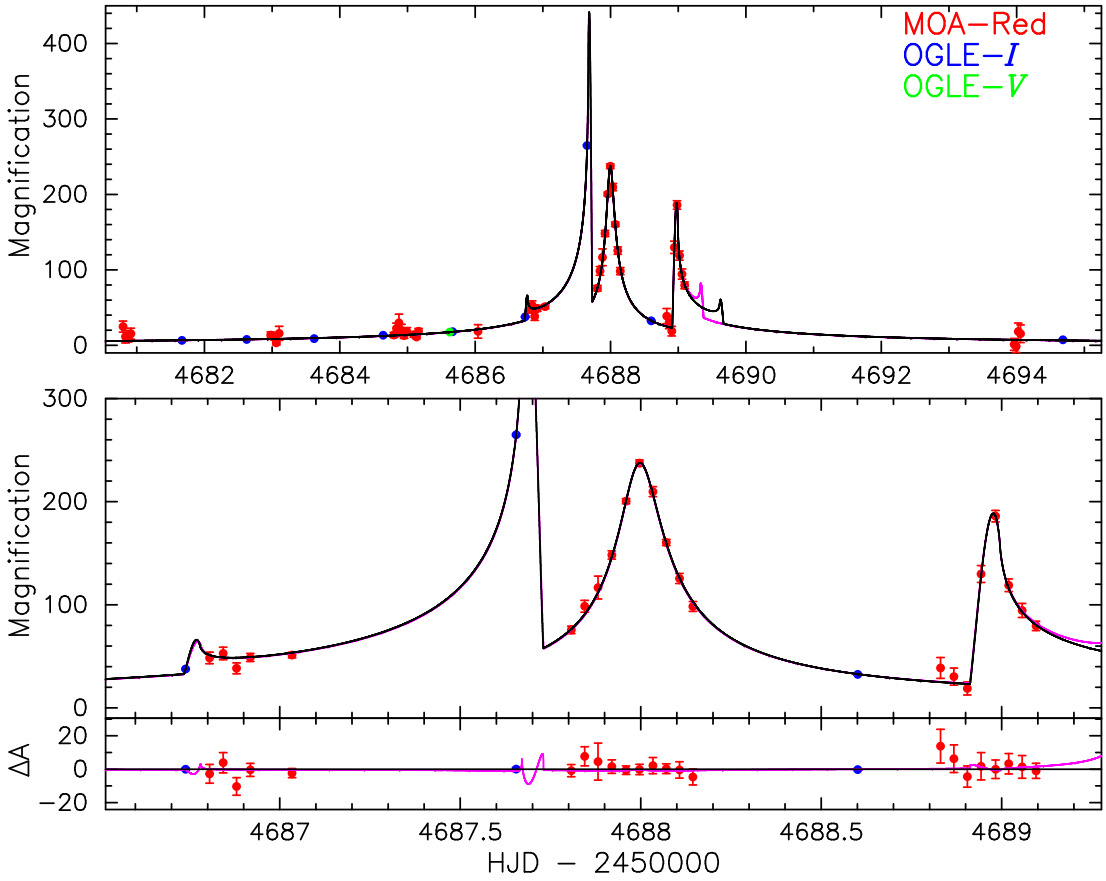

Figure 4.2: Light curve of MOA-2008-BLG-379. The top panel shows the magnified part of the light curve and the middle panel shows a close up of the anomaly. The red, blue, and green points are for MOA-Red, OGLE-I, and OGLE-V, respectively. The black and magenta lines indicate the best close and wide model. The bottom panel shows the residual from the best close model.

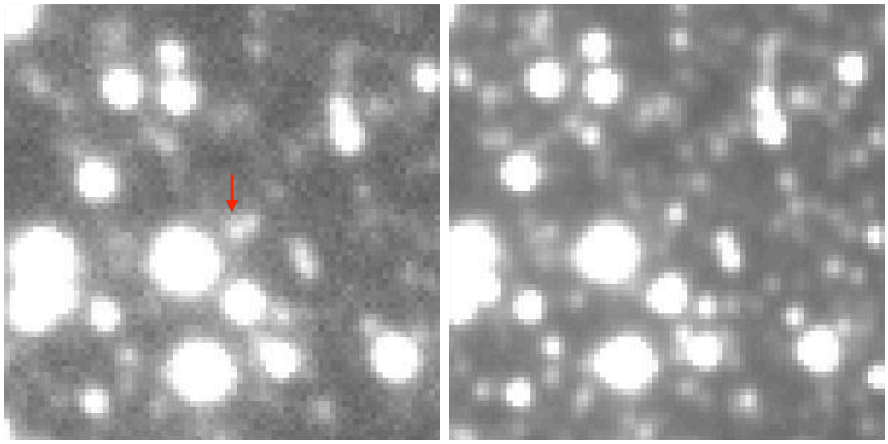

Figure 4.3: OGLE images for MOA-2008-BLG-379. The left image shows epoch HJD′ ∼ 4685.7 and the right is the OGLE reference image. The magnified source star is indicated by the red arrow in the left image. East is up and North is to the right.

4.1.2 Photometry

The MOA and OGLE data for MOA-2008-BLG-379 were reduced using the respective MOA (Bond et al. 2001) and OGLE (Udalski 2003) photometry pipelines. The initial reductions used the normal photometry available on the respective MOA and OGLE alert web sites, and these data were used to show that the correct model involved a planet. However, it was possible to obtain improved photometry for both the MOA and OGLE data sets. The improved MOA photometry used "cameo" sub-images centered on the target, and the improved OGLE photometry was redone with source position determined from difference images and a careful selection of reference images.

MOA photometry was found to have systematic errors at the beginning and/or end of each observing season, when observations are only possible at high airmass. This may be due to low-level variability for a very bright star about 3 arc seconds from the source, MOA-2008-BLG-379S. So we removed the MOA data prior to HJD′ = HJD − 2450000 = 4543, leaving 951 MOA data points in the range 4543 < HJD′ < 4762. The OGLE data consist of 294 I-band observations and 7 V-band observations, as shown in Table 4.1.

4.1.3 Error Normalization

The error bar estimates from the photometry codes are normally accurate to a factor of 2 or better, and they provide a good estimate of the relative photometry errors for each data set. These are sufficient to find the best light curve model, but in order to estimate the fit parameter uncertainties, we need more accurate error

Table 4.1: The Error Bar Corrections Parameters and Linear Limb Darkening Parameters for the Data Sets Used to Model the MOA-2008-BLG-379 Light Curve

Dataset	k	$e_{\rm min}$	Limb-darkening Coefficients	Number of Data
MOA-Red	1.266	0	0.5919	951
OGLE I-band	0.995	0	0.5493	294
OGLE V-band	1.180	0	0.7107	7

Note. The formula used to modify the error bars is $\sigma_i^{'} = k\sqrt{\sigma_i^2 + e_{\rm min}^2}$ where σ_i is the input error bar for the ith data point from the photometry code in magnitudes, and $\sigma_i^{'}$ is the final error bar used for the determination of parameter uncertainties.

bars, which have $\chi^2/{\rm dof} \simeq 1$ for each data set. Therefore, once we have found the best fit model with the unmodified error bars, we modify the error bars with the formula

$$\sigma_i' = k\sqrt{\sigma_i^2 + e_{\rm min}^2} \tag{4.1}$$

where σ_i is the input error bar estimate (in magnitudes) for the ith data point, k is the normalization factor, and $e_{\rm min}$ is the minimum error. The modified error bars, σ_i', are used for all subsequent modeling and parameter uncertainty determination.

The factors k and $e_{\rm min}$ are estimated for each data set with the following procedure. First, we plot the cumulative distribution of χ^2 as a function of the size of the input error bars, σ_i. Then, we chose the value of $e_{\rm min} \geq 0$ such that the cumulative distribution is a straight line with slope of unity. Then, the parameter k is chosen to give $\chi^2/{\rm dog} \simeq 1$ for each data set. For this event, we find that $e_{\rm min} = 0$ for all data sets. The values of k and $e_{\rm min}$ for all three data sets are listed in Table 4.1.

4.2 Light Curve Modeling

The systematic modeling described in Section 3.5 indicated a planetary mass ratio for the MOA-2008-BLG-379L lens system. Using the optimized dataset listed in Table 4.1, the best fit model was found with the same procedure as the systematic modeling (See Section 3.5). Figure 4.2 shows the light curve of this event and the best fit models. There are five distinct caustic crossing and cusp approach features in the light curve. The first caustic crossing is sandwiched between a single observation by OGLE and five MOA observations beginning 96 minutes later at HJD$'$ = 4686.8, The subsequent, very bright, caustic exit was observed with a single OGLE observation on the subsequent night, but the central cusp approach feature and the next caustic entrance feature were reasonably well sampled by 9

and 7 MOA observations, respectively, on the next two nights. It is the sampling of these two features that allow the parameters of the planetary lens model for this event to be determined.

For many binary events and most planetary events, the light curve has very sharp features due to caustic crossings or cusp approaches that resolve the finite size of the source star. Such features require an additional parameter, the source radius crossing time, t_*. Since the MOA-2008-BLG-379 includes caustic crossings and a close cusp approach, it is necessary to include finite source effects in its light curve model, and a proper accounting of finite source effects requires that limb darkening be included.

For the limb darkening coefficients, we adopted a linear limb-darkening model for the source star based on the source color estimate of $(V-I)_{\rm S,0} = 0.81 \pm 0.13$, which is discussed below in Section 4.3. This color implies that the source is a late G-star with an effective temperature of $T_{\rm eff} \simeq 5386$ K (Bessell & Brett 1988). We use limb-darkening parameters from Claret (2000) for a source star with an effective temperature $T_{\rm eff} = 5500$ K, surface gravity $\log g = 4.5$ cm s^{-2}, and metallicity $\log [{\rm M/H}] = 0.0$. Girardi's isochrones (Girardi et al. 2002) suggest that the source may be a metal poor star if it is located at the distance of the Galactic center, but $\log [{\rm M/H}] = 0.0$ is consistent within the 1-σ error bar. The list of the coefficients used for the linear limb-darkening model are as follows, 0.7107 for V, 0.5493 for I, and 0.5919 for MOA-Red, which is the mean of the coefficients for the Cousins R and I-bands. These are listed in Table 4.1.

As is commonly the case for high magnification events, there are two degenerate light curve solutions that can explain the observed light curve. This is the well-known "close-wide" degeneracy, where the solutions have nearly identical parameters except that the separation is modified by the $s \leftrightarrow 1/s$ transformation. Figure 4.4 shows the two caustic configurations from the close and wide models for this event. Sometimes, when the planetary caustics have merged with the central caustic to form a so-called resonant caustic curve, as in this case, the light curve data can resolve this close-wide degeneracy. We can see in Figure 4.2 that the close and wide light curves do have substantial differences, such as the time of the final caustic exit. However, the observations for this event are too sparse to sample these light curve features, and the degeneracy remains. Fortunately, the parameters for these two solutions differ by only $\sim 20\%$, so this degeneracy has little effect on the inferred physical parameters of the lens system. We find $s = 0.903 \pm 0.001$, $q = (6.85 \pm 0.05) \times 10^{-3}$ and $u_0 = (6.02 \pm 0.06) \times 10^{-3}$ for the close model, which is preferred by $\Delta\chi^2 = 0.7$, and $s = 1.119 \pm 0.001$, $q = (6.99 \pm 0.01) \times 10^{-3}$, and $u_0 = (6.03 \pm 0.03) \times 10^{-3}$ for the wide model. The full set of fit parameters are listed in Table 4.2.

Higher order effects such as microlens parallax, xallarap (source star orbital

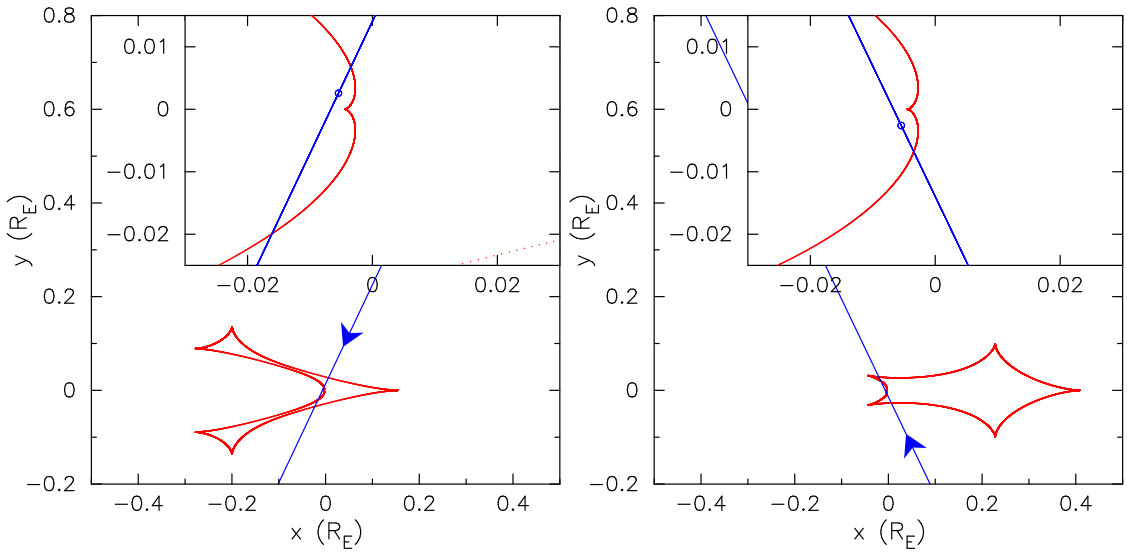

Figure 4.4: Caustic geometries for both close (left) and wide (right) models are indicated by the red curves. The insets in each panel are close up around the center of the coordinate. The blue lines show the source star trajectory with respect to the lens system, with arrows indicating the direction of motion. The small blue circles in the insets indicate the source star size.

Table 4.2: The Best Fit Model Parameters for Both the Wide and Close Models

Model	t_0 HJD′	$t_{\rm E}$ (days)	u_0 10^{-3}	q 10^{-3}	s	α (rad)	t_* (days)	χ^2
Wide	4687.896	42.14	6.03	6.99	1.119	1.124	0.0219	1246.7
	0.001	0.23	0.03	0.01	0.001	0.003	0.0020	
Close	4687.897	42.46	6.02	6.85	0.903	5.154	0.0212	1246.0
	0.001	0.45	0.06	0.05	0.001	0.002	0.0017	

Note. The second and fourth rows in each column are the 1-σ error bars for each parameter. HJD′ $\equiv$ HJD − 2450000.

motion) and orbital motion in the lens system have been detected in some previous events(Alcock et al. 1995, Gaudi et al. 2008, Bennett et al. 2010, Sumi et al. 2010, Muraki et al. 2011, Kains et al. 2013). The measurement of finite source effects or microlensing parallax effects can partially break the degeneracies of the physical parameters that can be inferred from the microlensing light curve, and the measurement of both microlensing parallax and finite source effects yields a direct measurement of the lens system mass (Bennett 2008, Gaudi 2012). For this event, however, the source is too faint for a reliable microlensing parallax measurement for an event of its duration, and the relatively sparse data sampling leaves some uncertainty in the measurement of the source radius crossing time. Therefore, we use the light curve constraints on the source radius crossing time to constrain the physical parameters of the lens system using a Bayesian analysis based on a standard Galactic model, as discussed in Section 4.5. If the lens star can be detected in high angular resolution follow-up observations, it will then be possible to directly determine the physical parameters of the lens system (Bennett et al. 2006, 2007, Dong et al. 2009a).

4.3 Lens Properties

4.3.1 Color-Magnitude Diagram

The source star magnitude and color estimated from the light curve modeling are affected by extinction and reddening due to interstellar dust. These effects must be removed in order to infer the intrinsic brightness and color of the source star. In order to estimate extinction and reddening, we use the centroid of the red clump giant (RCG) distribution, which is an approximate standard candle. The color magnitude diagram (CMD), shown in Figure 4.5 was made from stars from the OGLE-III catalog (Szymański et al. 2011) within $2'$ from the source star. From this CMD, we have found the RCG centroid to be at

$$(V-I, I)_{\rm RCG} = (2.55, 16.24) \pm (0.02, 0.04)\ . \tag{4.2}$$

We adopt the intrinsic RCG centroid $V-I$ color and magnitude from Bensby et al. (2011) and Nataf et al. (2013), respectively, which gives

$$(V-I, I)_{\rm RCG,0} = (1.06, 14.42) \pm (0.06, 0.04)\ . \tag{4.3}$$

Comparing the our measured RCG centroid from Equation (4.2) with the intrinsic dereddened magnitude and extinction from Equation (4.3), we find that the the reddening and extinction are

$$(E(V-I), A_I)_{\rm RCG} = (1.49, 1.82) \pm (0.06, 0.06) \tag{4.4}$$

, where $E(V-I)$ is the average reddening and A_I is the average extinction.

The models presented in Table 4.2 give the source magnitude and color of $I_{\rm S} = 21.30 \pm 0.03$ and $(V-I)_{\rm S} = 2.07 \pm 0.09$ from the OGLE observations, calibrated to the OGLE-III photometry map (Szymański et al. 2011). This color is bluer than most of the bulge main sequence stars at this magnitude, but with the error bars, it is marginally consistent with a bulge main sequence star, as shown in Figure 4.5. This could be due to the fact that there is only a single bright OGLE V-band image that might be affected by a nearby bright variable star.

4.3.2 Color from MOA-Red - OGLE I-band

Because the MOA-Red passband is centered at a slightly shorter wavelength than the OGLE I-band, we can use the MOA-Red and OGLE I passbands to derive the source color (Gould et al. 2010a). Although the color difference between these two passbands is relatively small, we have a large number of data points at significant magnification in both of these passbands. So, this method should yield a color that is less sensitive to systematic photometry errors than the determination based on the single magnified OGLE V-band measurement. In order to calibrate the MOA-Red measurements to the OGLE-III (V, I) system, we use the OGLE-III photometry map (Szymański et al. 2011) and a DoPHOT (Schechter, Mateo, & Saha 1993) reduction of the MOA reference frame. Because the seeing in the MOA reference frame is significantly worse than the seeing images used for the OGLE-III catalog, we choose isolated OGLE stars for the comparison with MOA to avoid problems due to blending in the MOA images. In order to select the stars with small uncertainty in magnitude and color, we remove faint stars with $I > 19$ and stars with a $V-I$ error bar > 0.1. In order to obtain an accurate linear relation, we only fit stars in the color range $2 < V-I < 4$. We recursively reject 2.5σ outliers and find

$$R_{M,\rm DoPHOT} - I_{\rm OGLE-III} = (0.18931 \pm 0.00533)(V-I)_{\rm OGLE-III} \qquad (4.5)$$

, where $I_{\rm OGLE-III}$ and $V_{\rm OGLE-III}$ are the OGLE-III catalog magnitudes, and $R_{M,\rm DoPHOT}$ is the calibrated MOA-Red band magnitude. (The MOA-Red calibration has a zero-point uncertainty of 0.0144 mag.) Figure 4.6 shows the linear relation of Equation 4.5. The MOA light curve photometry (Bond et al. 2001) is done with the difference imaging analysis (DIA; Tomaney & Crotts 1996, Alard & Lupton 1998), which is usually significantly more precise than DoPHOT, but DIA only measures changes in brightness, which is why DoPHOT photometry is used to derive the relation in Equation (4.5) between the $R_M - I_{\rm OGLE}$ and standard $V-I$ colors. Thus, it is important that the MOA-Red band photometry from the DIA and DoPHOT codes have identical magnitude scales. This is accomplished by using the DoPHOT point-spread function for the DIA photometry.

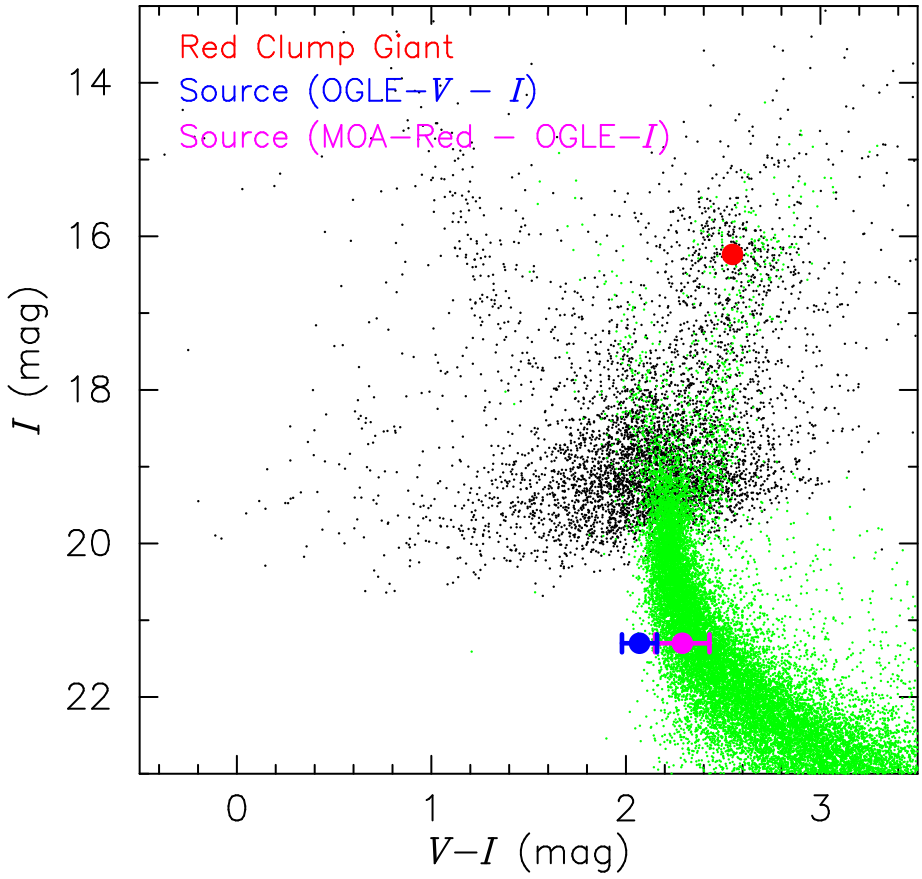

Figure 4.5: Color-magnitude diagram (CMD) of the stars within 2′ of MOA-2008-BLG-379 from the OGLE-III catalog is shown as black dots. The green dots show the *HST* CMD of Holtzman et al. (1998) whose extinction is adjusted to match the MOA-2008-BLG-379 using the Holtzman field red clump giant (RCG) centroid of $(V-I, I)_{\rm RCG,Holtz} = (15.15, 1.62)$ (Bennett et al. 2008). The red dot indicates the RCG centroid for the MOA-2008-BLG-379 field. The source star color and magnitude derived from OGLE VI is indicated with a blue dot, while the source star color and magnitude derived from the MOA-Red and OGLE-I passbands is shown as a magenta dot. Although the error bars on the MOA-Red + OGLE-I color estimate are similar to the error bar from the OGLE VI estimate, we use the MOA-Red + OGLE-I estimate for the source color because it is subject to smaller systematic uncertainties.

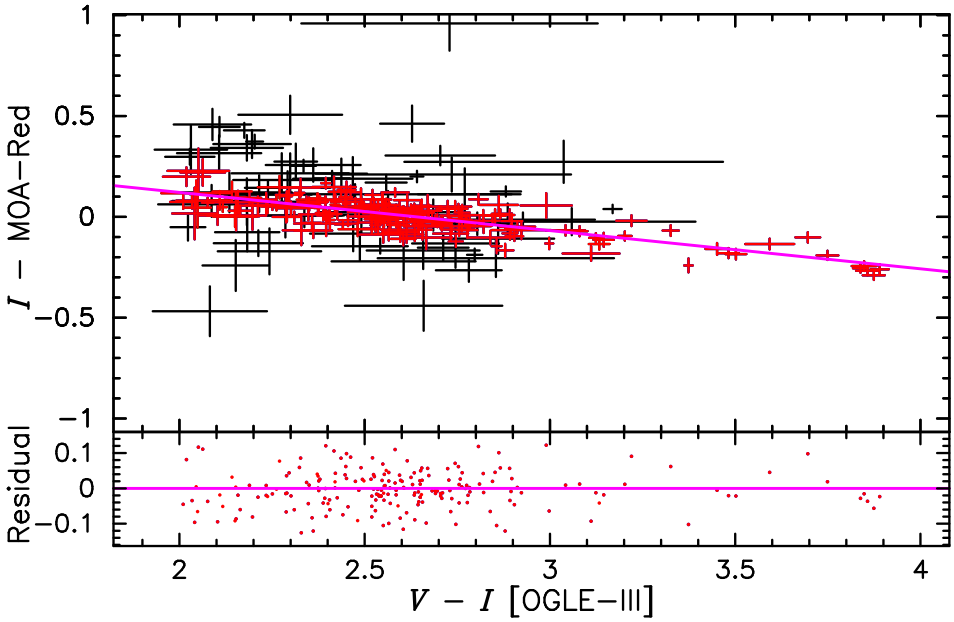

Figure 4.6: Color-color relation of $(V-I)_{\rm OGLE-III}$ and $I_{\rm OGLE-III} - R_{M,\rm DoPHOT}$. The black plus marks are all the stars used for the fit to get the linear relation. The red plus marks are used after rejecting 2.5 σ outliers. The mageta line shows the best fit. The bottom panel shows the residual from the best fit.

Using the source magnitudes from the light curve modeling, this procedure yields $(V-I, I)_{\rm S} = (2.29, 21.30) \pm (0.14, 0.03)$ for the best fit model. As shown in Figure 4.5, this source magnitude and color are more reasonable for a bulge source than the less precise color derived from OGLE V-band measurements, and it is the one that we use in our analysis.

Combining the extinction from Equation (4.4) with the source magnitudes and colors from the best fit wide and close models, we have

$$(V-I, I)_{\rm S,0} = (0.79, 19.48) \pm (0.13, 0.06) \text{ for the wide model} \quad (4.6)$$

$$(V-I, I)_{\rm S,0} = (0.80, 19.49) \pm (0.12, 0.06) \text{ for the close model.} \quad (4.7)$$

Also, from the light curve models, we have determined the magnitude of the unlensed flux at the location of the source. This is the flux of the stars with images blended with the source. The flux from the blend stars is often used as an upper limit for the magnitude of the lens star. In this event, however, we found that the blending flux in the light curve is dominated by the flux from a bright star 0.″5 away from the event by the careful inspection of the OGLE reference image shown in Figure 4.3. We found no star is resolved at the position of the event and thus the real upper limit of the lens magnitude is fainter. If we assume

that the extinction to these blend stars are the same as the source (which is a reasonable approximation if the stars are at a distance of $\gtrsim 4\,\mathrm{kpc}$), then we have the extinction-free 3-σ limit of blend magnitude

$$I_{\mathrm{b},0} > 17.87 \text{ mag} \tag{4.8}$$

, which will be used as an upper limit for the magnitude of the planetary host star in Section 4.5.

4.4 Angular Einstein Radius θ_{E}

With the use of $(V-I, I)_{\mathrm{S},0}$, we can determine the source angular radius with the color surface–brightness relation of Kervella and Fouqué (2008),

$$\log_{10}(2\theta_*) = 0.4992 + 0.6895(V-I) - 0.0657(V-I)^2 - 0.2V \ . \tag{4.9}$$

This yields an angular source radius of $\theta_* = 0.45 \pm 0.07$ μas. θ_* is also able to be derived from the method of Kervella et al. (2004) with $(V-K)_{\mathrm{S},0}$ estimated from the dwarf star color-color relations from Bessell & Brett (1988), but the result is consistent with the above value. We can combine this value of θ_* with the fit source radius crossing time, t_*, values from the light curve models to determine the lens-source relative proper motion,

$$\mu_{\mathrm{rel}} = \frac{\theta_*}{t_*} = \frac{\theta_{\mathrm{E}}}{t_{\mathrm{E}}} = 7.46 \pm 1.65 \text{ mas yr}^{-1} \text{ for the wide model} \tag{4.10}$$

$$= 7.75 \pm 1.56 \text{ mas yr}^{-1} \text{ for the close model.} \tag{4.11}$$

Note that this is the relative proper motion in the instantaneously geocentric inertial reference frame that moved with the Earth when the event reached peak magnification. The measurement of t_* also yields the angular Einstein radius

$$\theta_{\mathrm{E}} = \frac{\theta_* t_{\mathrm{E}}}{t_*} = 0.86 \pm 0.19 \text{ mas for the wide model} \tag{4.12}$$

$$= 0.90 \pm 0.18 \text{ mas for the close model ,} \tag{4.13}$$

which can be used to help constrain the lens mass.

As we discuss in Section 4.6, follow-up observations might be able to detect the lens separating the source and measure the lens-source relative proper motion. However, this would be in the heliocentric reference frame rather than the instantaneously geocentric inertial frame used for Equations (4.10) and (4.11). Fortunately, the follow-up observations and light curve model provide enough information to convert between these two reference frames.

For this paper, however, we have not been able to distinguish the wide and close models, so to obtain our final predictions, we combine the values from the wide and close models with weights given by $e^{-\Delta\chi^2/2}$. This gives an angular Einstein radius and lens-source relative proper motion of

$$\theta_{\rm E} = 0.88 \pm 0.19 \text{ mas} \quad (4.14)$$

$$\mu_{\rm rel} = 7.63 \pm 1.61 \text{ mas yr}^{-1} , \quad (4.15)$$

with the lens-source relative proper motion in the same instantaneous geocentric inertial reference frame used for Equations (4.10) and (4.11).

4.5 Bayesian Analysis

A microlensing light curve for a single lens event normally has the lens distance, mass, and angular velocity with respect to the source constrained by only a single measured parameter, the Einstein radius crossing time, $t_{\rm E}$. But, like most planetary microlensing events, MOA-2008-BLG-379 has finite source effects that allow t_*, and therefore $\theta_{\rm E}$, to be measured. If we could have also measured the microlensing parallax effect, we could determine the total lens system mass (Bennett 2008, Gaudi 2012).

Without a microlensing parallax measurement, we are left with the relation

$$\theta_{\rm E}^2 = \kappa M \left(\frac{1}{D_{\rm L}} - \frac{1}{D_{\rm S}} \right) \quad (4.16)$$

where $\kappa = 8.14 \text{ mas}/M_\odot$, M is the mass of the lens system, and $D_{\rm S}$ is the distance to the source star. This can be interpreted as a lens mass–distance relation, since $D_{\rm S}$ is approximately known.

We can now use this mass-distance relation, Equation (4.16), in a Bayesian analysis to estimate the physical properties of the lens system (Beaulieu et al. 2006). Our Bayesian analysis used the Galactic model of Han & Gould (2003) with an assumed Galactic center distance of 8 kpc with model parameters selected from the MCMC used to find the best fit model. The lens magnitude is constrained to be less than the blend magnitudes presented in Equation (4.8). Since the best fit wide model is slightly disfavored by $\Delta\chi^2 = 0.7$, we weight the wide model Markov chains by $e^{-\Delta\chi^2/2}$ with respect to the close model Markov chains. The probability distributions resulting from this Bayesian analysis are shown in Figures 4.7 and 4.8.

An important caveat to this Bayesian analysis is that we have assumed that stars of all masses, as well as brown dwarfs, are equally likely to host a planet with the measured mass ratio and separation. Because of this assumption, the results

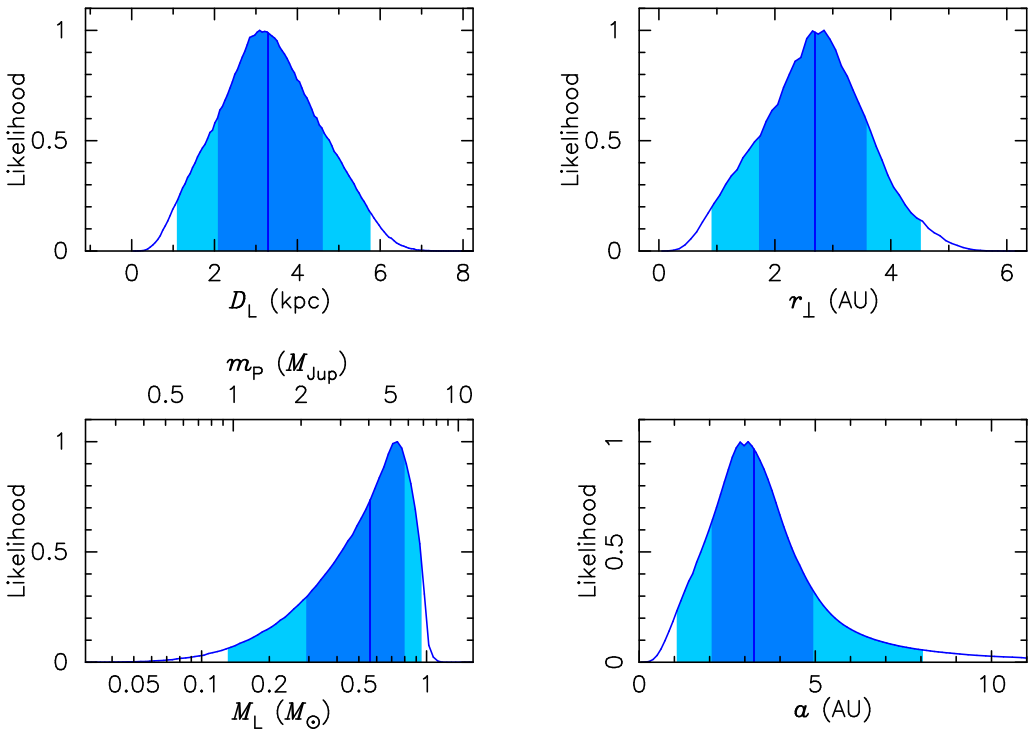

Figure 4.7: Probability distribution of lens parameters from the Bayesian analysis. The top-left panel shows the probability of the distance to the lens system. The bottom-left panel shows the mass of the primary and secondary lenses (the star and planet) in units of Solar and Jupiter masses, respectively. The top-right panel shows the projected separation $r_\perp$. The bottom-right panel shows the three-dimensional star-planet separation a, assuming a random inclination and phase. The dark and light blue regions indicate the 68% and 95% confidence intervals, and the vertical lines indicate the median value.

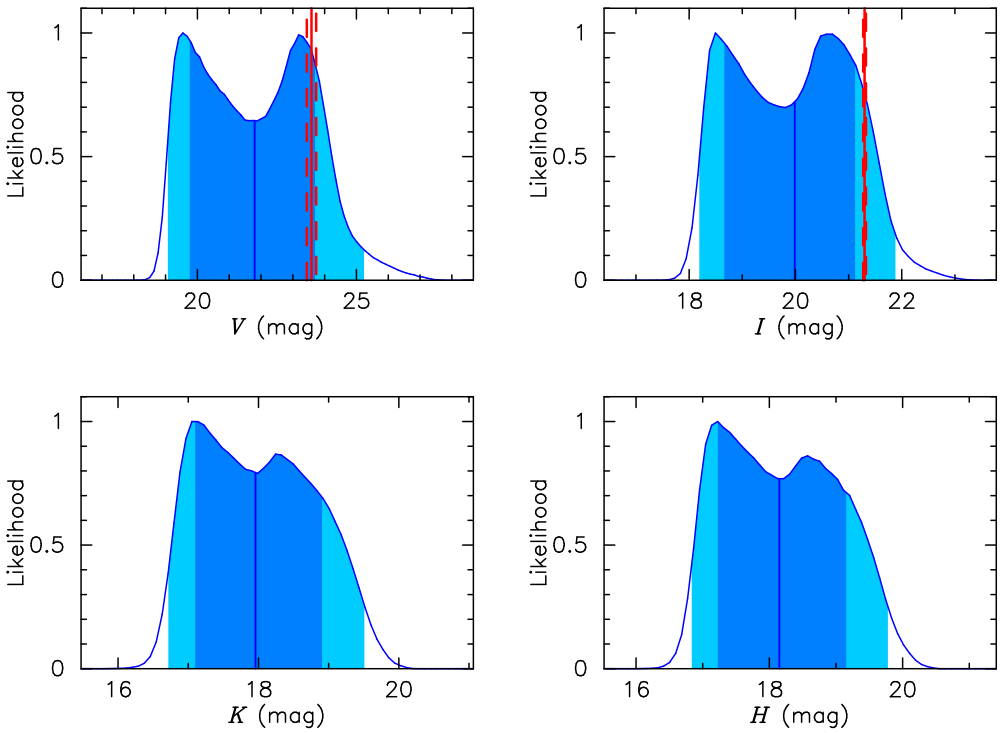

Figure 4.8: Probability distribution of V-, I-, K- and H-band magnitudes for the extinction-free lens star from the Bayesian analysis. The dark and light blue regions indicate the 68% and 95% confidence intervals. The red solid lines show the source star magnitudes with the extinction estimated in Equation (4.4), and the red dashed lines are their 1 sigma errors.

of this Bayesian analysis cannot (directly) be used to determine the probability that stars will host planets as a function of their mass. With this caveat, the star and planet masses resulting from the Bayesian analysis are $M_{\rm L} = 0.56^{+0.24}_{-0.27}\ M_\odot$ and $m_{\rm P} = 4.1^{+1.7}_{-1.9}\ M_{\rm Jup}$, respectively. Their projected separation was determined to be $r_\perp = 2.7^{+0.9}_{-1.0}$ AU, and the lens system is at a distance of $D_{\rm L} = 3.3^{+1.3}_{-1.2}$ kpc. The three-dimensional star-planet separation is estimated to be $a = 3.3^{+1.7}_{-1.2}$ AU, assuming a random inclination and phase. These values are listed in Table 4.3. Therefore, the most likely physical parameters from the Bayesian analysis, indicate that the planet has a mass of nearly 4 Jupiter-masses and orbits a late K-dwarf host star at just over twice the distance of the snow line.

Table 4.3: Physical Parameters of the Lens System Obtained from the Bayesian Analysis

Primary Mass $M_{\rm L}$ ($M_\odot$)	Secondary Mass $m_{\rm P}$ ($M_{\rm Jup}$)	Distance $D_{\rm L}$ (kpc)	Projected Separation $r_\perp$ (AU)	Separation a (AU)
$0.56^{+0.24}_{-0.27}$	$4.1^{+1.7}_{-1.9}$	$3.3^{+1.3}_{-1.2}$	$2.7^{+0.9}_{-1.0}$	$3.3^{+1.7}_{-1.2}$

4.6 Discussion

We reported on the discovery and analysis of a planetary microlensing event MOA-2008-BLG-379. As is often the case with high magnification microlensing events, there are two degenerate models: a close model with a planet-host separation of $s = 0.903$ and a wide model with $s = 1.119$. Both have a mass ratio of $q \simeq 7 \times 10^{-3}$. Our Bayesian analysis indicates that the lens system consists of a G, K, or M-dwarf orbited by a super-Jupiter mass planet. The most likely physical properties for the lens system, according to the Bayesian analysis, are that the host is a late K-dwarf, and the planet has a mass of about 4 Jupiter masses with a projected separation of about 3 AU. However, these values are dependent on our prior assumption that stars of different masses have equal probabilities to host a planet of the observed mass ratio and separation.

Fortunately, the parameters of this event are quite favorable for a direct determination of the lens system mass and distance by the detection of the lens separating from the source star in high angular resolution follow-up observations (Bennett et al. 2006, 2007). The source star is quite faint at $I_{\rm S} = 21.30 \pm 0.03$, so it is unlikely that the lens will be very much fainter than the source. The brightness

of the source is compared to the Bayesian analysis predictions for the lens (host) star in the V-, I-, H-, and K-bands in Figure 4.8. This indicates that the lens star is likely to have a similar brightness to the source in all of these passbands. Also, it is unlikely that the lens and source magnitudes will differ by more than 2 mag in any of these passbands, so both the source and lens should be detectable.

The measured source radius crossing time indicates a relatively large lens-source relative proper motion of $\mu_{\rm rel} = 7.6 \pm 1.6$ mas yr^{-1} (measured in the inertial geocentric reference frame moving at the velocity of the Earth at the peak of the event). This implies a separation of $\sim 37.8 \pm 8.3$ mas in the later half of 2013 when high resolution follow-up observations were obtained from Keck and the *Hubble Space Telescope* (*HST*). (Because the relative proper motion, $\mu_{\rm rel}$, is measured in an instantaneously geocentric reference frame, it cannot be directly converted into a precise separation prediction, but the conversion to the heliocentric reference frame, which is more relevant to the follow-up observation, usually results in a small change.) The results of these follow-up observations will be reported in a future publication, but it seems quite likely that the planetary host star will be detected, resulting in a complete solution of the lens system. That is, the lens masses, distance and separation will all be determined in physical units.

One unfortunate feature of this discovery is that MOA-2008-BLG-379 was not recognized as a planetary microlensing event when it was observed. This was partly due to the faintness of the source star, which rendered the relatively long planetary perturbation as the dominant portion of the magnified light curve. However, the lack of familiarity with the complete variety of binary lens and planetary microlensing light curves also played a role in this lack of recognition. The planetary nature of the event was discovered as a result of a systematic effort to model all of the binary microlensing events that were found by the MOA alert system. Fortunately, the joint analysis of OGLE data and the high cadence MOA-II survey observations allowed the planetary nature of the event to be establish and the basic planetary lens parameters to be measured.

Chapter 5

Abundance of Giant Exoplanets beyond the Snow Line

With use of the archival MOA-II data in 2007–2012, we construct a sample that consists of 1471 single lens events with high signal-to-noise ratio (S/N) to the detectable planets. 21 planets, which include several new candidates discovered by the systematic modeling of all the anomalous events, are found to be enough detectable by the sensitivity of the selected single lens events in the sample. The correction by the detection efficiencies to the planets yields the planetary mass function, $F = F_0(m_{\rm P}/m_0)^{\alpha}$ where $F_0 = 10^{-0.67\pm0.10}$, $\alpha = -0.78 \pm 0.12$, and $m_0 = 95.2\ M_{\odot}$. We integrate the planetary mass function and find that a star has on average $0.15^{+0.04}_{-0.03}$ Jupiter like planets ($0.3 - 10\ M_{\rm Jup}$) within $0.5 < a < 10$ AU.

5.1 Event Selection

In 2007–2012, MOA-II issued 3300 microlensing alerts from the high cadence survey observations toward the Galactic bulge. These alerted events include some contaminations which mimic the microlensing light curve and are hard to be distinguished. They could be periodic variable stars, cataclysmic variable stars (CVs), asteroids, or other transient events. In order to provide a statistical analysis of microlensing events, all the contaminations should be removed from the microlensng alerts. Because the goal of this paper is estimating the planet abundance around main sequence single stars, the stellar binary microlensing events also should be removed. In this section, we discuss the criteria for the event selection to make a well-defined sample, where we can detect a planet signal confidently.

5.1.1 Stellar Binary Events and Cataclysmic Variable Stars

Microlensing is able to detect circumbinary planets (Gaudi 2012). It is possible to estimate the planet abundance around stellar binary system by microlensing. But, this requires the calculation of detection efficiency to planets in stellar binary events. These analysis are very complicated and beyond this paper. To estimate an average number of planets around a single star, stellar binary events should be removed from the sample. By using the binary lens model (See Section 3.5), we fit all the anomalous events, which have deviations from the single lens model in the light curve, and set mass ratio threshold $q = 0.03$ as a boundary between stellar binary and planetary system. Bond et al. (2004) also used 0.03 as the boundary. Some anomaly events still have deviation from the binary lens model. Most of them are thought of as CVs because they show characteristic light curves. They have sharp rise and shallow drop of brightness, and show plateau in the dropping side. These events are removed from the sample by visual inspections because they are not microlensing events.

5.1.2 Criteria for Single Lens Events

After rejecting the stellar binary lens events and CVs, we apply the following rejection criteria to remove poor-quality single lens events where we could not search for planetary anomalies confidently. Note that any criteria should be acceptable unless they do not depend on the presence or absence of planetary anomalies in the light curves. In the following rejection criteria, we fit the remaining events with finite-source single-lens model, where the angular source star radius is estimated as described in Section 5.2.2. The rejection criteria are

Cut-1 $t_0 < 0$, $u_0 = 0$, $t_{\rm E} < 1$, $t_{\rm E} > 500$ and $u_0 > 2$

Cut-2 $\delta u_0/u_0 > 0.5$, $\delta t_{\rm E}/t_{\rm E} > 0.2$

Cut-3 low S/N ($\sum {\rm f/fe} < 1000$) around the peak, $|(t - t_0)/t_{\rm E}| < 1$

Cut-4 low S/N ($\sum {\rm f/fe} < 200$) on the one side of the wing

Cut-5 low S/N ratio on the one side of the wing to the other side (smaller than 10%).

Cut-1 is used for rejecting contaminations and confusing events that are seemingly hard to classify as a microlensing or other type of variable star. For the other type of variable stars or the light curves with a poor coverage, the parameters given by the single-lens model become unphysical. We also use the cut for the events with large impact parameter. In these events the size of caustics is small

and the source star might be bright giant star, where the probability of caustic crossing is very small and the finite source effect might be remarkable. In these events, therefore, the detection efficiency, which is a probability of the detection of a planet with a given dataset if we assume a planet with a certain separation and mass ratio, should be low. Thus, they do not affect the statistical analysis.

Cut-2 is used for the events with large uncertainties in the impact parameter and event timescale. These uncertainties become large if the data has a poor coverage over the peak in high-magnification events, or the blending degeneracy is large. The cut for the impact parameter is also used in the previous works (Gaudi et al. 2002, Cassan et al. 2012). The small uncertainty in the impact parameter u_0 is required to search for the anomaly in the light curve. We apply these criteria to choose robust single lens events in which we can reliably search for planetary signals. Now the selected sample consists of pure single lens events.

Cut-3 – Cut-5 are used to leave the events with good coverage over the peak. Microlensing method is most sensitive to the planet around the Einstein radius, that is, $s \simeq 1$. Many theoretical studies have shown that the detection efficiency is high in the "lensing zone", $0.6 \leq s \leq 1.6$, where the caustics exist within the Einstein radius. This means that anomaly tends to occur at least during the time, $(t_0 - t)/t_{\rm E} < 1$. Therefore, Cut-3 is necessary to leave the events sensitive to the anomaly. Also, the coverage of the both side of the wing, which is the rising and declining part of the light curve, is necessary to claim the anomaly confidently in the well determined light curve parameters.

As a result, imposing these criteria on the total 3300 microlensing events, we select 1471 robust single lens events that consist of 216, 215, 254, 280, 207 and 299 events in 2007, 2008, 2009, 2010, 2011 and 2012, respectively. The cumulative distribution of $t_{\rm E}$ for the selected events are plotted in Figure 5.1.

5.1.3 Planetary Events Sample

In our analysis, we decide the event is a planetary event if the best fit model with mass ratio of $q < 0.03$ is preferred to the binary model with mass ratio of $q > 0.03$ by $\Delta\chi^2_{\rm B-P} = \chi^2_{\rm B} - \chi^2_{\rm P} > 25$, where $\chi^2_{\rm B}$ and $\chi^2_{\rm P}$ are χ^2 of the binary model with $q > 0.03$ and planetary model with $q < 0.03$, respectively. The planetary events with $q < 0.03$ are selected by the systematic modeling of all the anomalous events, where on-line MOA data are used for the parameter estimation. Here, we should select all the planetary events which could be found from the MOA survey alone. Because only MOA data is used in this analysis, well-known planetary events that do not show any anomalies in MOA dataset, such as MOA-2007-BLG-400 (Dong et al. 2009b) and MOA-2008-BLG-310 (Janczak et al. 2010), should be removed. In the actual observation, once anomaly signal is found, observers change the observation frequency higher than normal strategy to obtain good coverage over

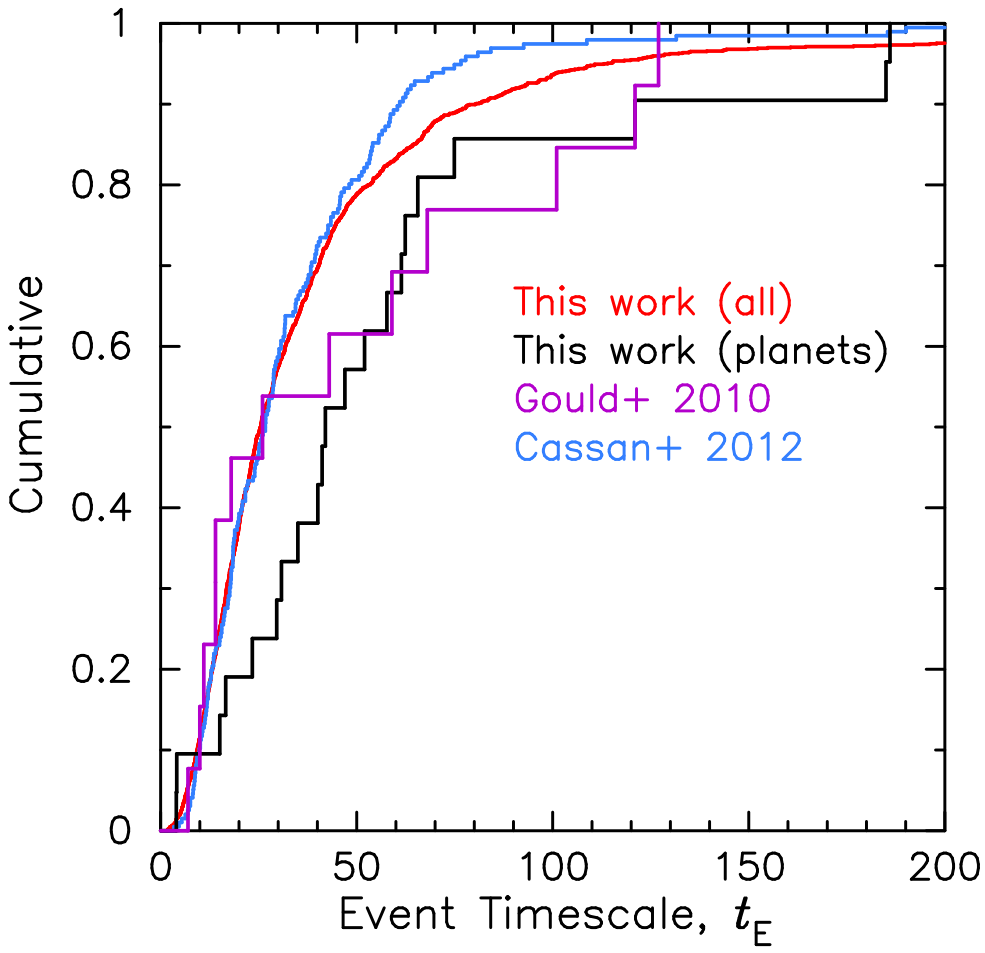

Figure 5.1: Cumulative distribution of the event timescale $t_{\rm E}$. The red line shows our sample of the 1471 single lens events. The black line shows the cumulative distribution for the 21 planetary events. The distribution of our sample is similar to the sample of Cassan et al. (2012) drawn with the blue line. Gould et al. (2010b) drawn in the purple line also has almost same median value, but might be distorted to the long $t_{\rm E}$. The black line shows the cumulative distribution of the 21 planets listed in Table 5.1. The planet distribution seems to be biased to longer event timescale. This is discussed in Section 5.7.

the anomaly signal. Getting more dense data by changing observation frequency is good for modeling light curve. This is, however, not appropriate for the statistical analysis because the observation frequency was raised due to the existence of the planet and this makes the efficiency biased. In order to get rid of this bias in the dataset, we reduced the extra data points in the planetary events assuming that the anomalies had not been detected and the event had been observed with normal frequency. We examine the significance of the planetary signal in each planetary event with the reduced data points. Here, we define the significance, $\Delta\chi^2_{\rm S-P} = \chi^2_{\rm S} - \chi^2_{\rm P}$, where $\chi^2_{\rm S}$ is the χ^2 produced by the best single lens model fitting. We decide the significance is enough, if $\Delta\chi^2_{\rm S-P} > \chi^2_{\rm thres}$, where we set $\chi^2_{\rm thres} = 100$. We discuss this threshold, in Section 5.2.1.

Planetary events also should satisfy the criteria that are used for single lens event selection in Section 5.1.2. Assuming the planets have been absent, we generate single lens light curves using the actual data points and the three parameters, $t_0, t_{\rm E}$ and u_0 in each planetary event. Note that in the artificial light curve, the extra data points are removed because they would have not been taken if there were no anomalies. Next, we impose the criteria (Cut-1 - Cut-5) on the generated light curves. Then, we find that 21 planetary events satisfy both the significance of planetary signal and criteria for the single lens events. They are listed in Table 5.1, and the light curves of each event are plotted in Figure 5.2 – 5.8. Note that these events are able to be characterized as planetary events with online MOA data alone. For the precise analysis, i.e., measurements of parallax effect and orbital motion of the lens system, optimized MOA data and reduced data from other telescopes (survey data by OGLE and WISE, and follow-up data by follow-up groups, such as μFUN, PLANET, RoboNet, and MINDSTEp) are necessary. Figure 5.10 shows the histogram of the mass ratios for the 21 planets. We add these 21 planetary events to the single lens sample, which are used to calculate detection efficiency, so the total number of the sample is 1492. As for the published planets, the values in the each reference are used for the table. For the other events, we use the values from our analysis, where the parameters of $t_{\rm E}$, u_0, q and s are well determined but $M_{\rm L}$, $m_{\rm P}$ and a are estimated by the Bayesian analysis with relatively large uncertainty of $\sim 20\%$.

We also list the planet candidates with $4 < \Delta\chi^2_{\rm B-P} < 25$ and $0 < \Delta\chi^2_{\rm B-P} < 4$ in Table 5.2 and Table 5.3. Although these events prefer the planetary model with $q < 0.03$ to the stellar binary model, optimized MOA data and data points from other telescopes might be required to claim the detection of planets. We proceed the statistical analysis with and without the 3 planet candidates listed in Table 5.2. Figure 5.9 shows the light curves of these 3 events. The comparison of the final results between with and without the 3 planet candidates is discussed in Section 5.8.

Among the planetary events listed in Table 5.1, 10 planets are already published and 9 planets are being prepared to publish. The other 2 events, MOA-2007-BLG-189, MOA-2010-BLG-353 are found for the first time after we analyzed all the binary events in the archival data. The followings are the brief comments about the each planetary event and planetary candidate with $4 < \Delta\chi^2_{\rm B-P} < 25$.

MOA-2007-BLG-189: this event was found as a planetary event for the first time after the systematic analysis of all the binary events in the archival MOA-II data. Although the mass ratio is smaller than the mass ratio criteria $q = 0.03$, the event timescale is long; $t_{\rm E} = 186$ days. Long $t_{\rm E}$ is preferred by a massive lens star in the Bayesian analysis, so the planet mass results in almost the boundary of the brown dwarf. The light curve has a residual around HJD$' \equiv$ HJD $-$ 2450000 $=$ 4330. This could be explained by a parallax effect (an effect of the orbital motion of the Earth), xallarap effect (an effect of the orbital motion of the possible binary source star), or orbital motion of the planet (in the lens system). A further analysis including these high-order effects will reveal the nature.

MOA-2007-BLG-192: the anomaly was characterized by the only survey data of OGLE and MOA. Despite the sparse data, it was found that about 3 $M_\oplus$ planet orbits around a very late type star from the light curve analysis and a Bayesian analysis (Bennett et al. 2008). Adaptive optics images taken with the Very Large Telescope NACO instrument are used to constrain the Bayesian analysis, which confirm the lens star as an M-dwarf (Kubas et al. 2012).

MOA-2007-BLG-308: although the initial anomaly alert failed to reach the MOA observers, they noticed independently the anomaly of the steep rise at HJD$' \sim 4303$. Sumi et al. (2010) estimated that a planet with $m_{\rm P} = 20^{+7}_{-8}\ M_\oplus$ orbits around a late type star with $M = 0.64^{+0.21}_{-0.26}\ M_\odot$.

MOA-2007-BLG-379: this is a high-magnification events with a planet of mass ratio $q \sim 3 \times 10^{-4}$. A detail analysis is ongoing.

MOA-2008-BLG-288: the anomaly was characterized by the only survey data of OGLE and MOA. The caustic exit around HJD$' \sim 4645$ was well covered by MOA. The mass ratio is $q \sim 0.012$.

MOA-2008-BLG-379: the anomaly was characterized by the only survey data of OGLE and MOA (Suzuki et al. 2014). Although $t_{\rm E}$ and u_0 are degenerate with MOA data alone (thus, the magnification in Figure 5.3 is higher compared to Figure 4.2), the light curve modeling confirms the mass ratio of a planetary range. See Chapter 4.

MOA-2009-BLG-266: the anomaly was noticed by the MOA observers in real time. Immediately after the anomaly alert was issued by MOA around HJD$' \sim 5086$, follow up observations were conducted from various observatories. Muraki et al. (2011) found both the finite source and parallax effects, and derived the mass of and distance to the lens system; $D_{\rm L} = 3.04 \pm 0.33$ kpc, $M_{\rm L} = 0.56 \pm 0.09\ M_\odot$, $m_{\rm P} = 10.4 \pm 1.7\ M_\oplus$, and $a = 3.2^{+1.9}_{-0.5}$ AU.

MOA-2009-BLG-319: the peak of this high-magnification event was intensively monitored by MOA-II telescope. Miyake et al. (2011) estimated that a planet with $m_{\rm P} = 50^{+44}_{-24}\ M_\oplus$ orbits around a late type star with $M = 0.38^{+0.34}_{-0.18}\ M_\odot$.

MOA-2009-BLG-387: the whole anomaly was covered by the combination of MOA and follow-up telescopes around the world. This intensive monitoring yielded the precise measurement of finite source effect, but the parallax effect was degenerated with the orbital motion of the planet. Batista et al. (2009) estimated that a planet with $m_{\rm P} = 2.6^{+4.1}_{-1.6}\ M_{\rm Jup}$ orbits around a late type star with $M = 0.19^{+0.30}_{-0.12}\ M_\odot$ (with 90 % confidence).

MOA-2010-BLG-117: this event is definitely a planetary event with mass ratio of $q \sim 4 \times 10^{-4}$. But, the planetary model does not fit to the data between HJD$' = 5405 - 5410$, which could be explained by an additional companion to the lens or source star.

MOA-2010-BLG-328: the anomaly in this event was found by the MOA observers about 20 days after the primary peak. Furusawa et al. (2013) estimated that a planet with $m_{\rm P} = 9.2 \pm 2.2\ M_\oplus$ orbits around a late type star with $M = 0.11 \pm 0.01\ M_\odot$.

MOA-2010-BLG-353: this event was found as a planetary event for the first time after the systematic analysis of all the binary events in the archival MOA-II data. The primary magnification is relatively low, and the anomaly signal seems week. But, an optimized data will increase the anomaly signal to the primary magnification. The mass ratio is $q \sim 1.7 \times 10^{-3}$.

MOA-2010-BLG-477: the whole anomaly part was covered many follow-up telescopes. Bachelet et al. (2012) estimated that a planet with $m_{\rm P} = 1.5^{+0.8}_{-0.3}\ M_{\rm Jup}$ orbits around a primary star with $M = 0.67^{+0.33}_{-0.13}\ M_\odot$.

MOA-2011-BLG-028: the anomaly, which was covered by only MOA and OGLE, happened when the source star passed close to the planetary caustic located outside of the Einstein ring radius. Since most of the discovered planetary caustic crossing or approach occur inside of the Einstein ring radius, this geometry might be relatively rare. The mass ratio is $q \sim 1.2 \times 10^{-4}$.

MOA-2011-BLG-197: the anomaly was found by the MOA observers and well covered by many telescopes around the world. The event timescale is relatively longer and the light curve is intensively monitored, so the high-oder effects might be detectable. The mass ratio is $q \sim 3.5 \times 10^{-3}$.

MOA-2011-BLG-262: this event has not only the planetary mass ratio $q \sim 5 \times 10^{-4}$, but also a short event timescale. Thus, the primary star might be less massive. Bennett et al. (2013) found that two different models can explain the light curve. They estimated that the lens system consists of a primary with $M_{\rm L} = 0.11^{+0.21}_{-0.06}\ M_\odot$ and a companion with $m_{\rm P} = 17^{+28}_{-10}\ M_\oplus$, or a primary with $M_{\rm L} \sim 3\ M_{\rm Jup}$ and a companion with $m_{\rm P} \sim 0.5\ M_\oplus$.

MOA-2011-BLG-322: the light curve of online MOA data seems messy due to the bright blending flux, which comes from unrelated stars or lens star itself. Shvartzvald et al. (2013) estimated that a planet with $m_{\rm P} = 11.6^{+13.4}_{-5.6}\ M_{\rm Jup}$ orbits around a primary star with $M = 0.39^{+0.45}_{-0.19}\ M_\odot$.

MOA-2012-BLG-288: many follow-up groups observed this event over the peak since the high-magnification alert was issued before the peak. Some data points are below the best fit model around $\mathrm{HJD}' = 6069$ due to the saturation. The mass ratio is $q \sim 2.9 \times 10^{-3}$.

MOA-2012-BLG-355: a variable star projected close to the source and lens stars contaminates the light curve, thus it seems noisy. A re-reduced data without the systematics is necessary to determine the parameter of the light curve model. The mass ratio is $q \sim 8.8 \times 10^{-4}$.

MOA-2012-BLG-505: although the anomaly in this event was missed in real-time, it was characterized as a planetary event thanks to the high cadence MOA-II observation. The mass ratio is $q \sim 8.3 \times 10^{-4}$.

MOA-2012-BLG-527: the MOA observers found the anomaly at $\mathrm{HJD}' = 6150$, and the anomaly alert was issued immediately after that. The mass ratio is $q \sim 9.5 \times 10^{-4}$.

MOA-2010-BLG-330: the peak of this event is perturbed by a central caustic. A re-reduce data is necessary to determine the parameter of the light curve model. The mass ratio is $q \sim 3.5 \times 10^{-3}$.

MOA-2011-BLG-291: although the light curve is seemingly single lens event, the data around the peak has a deviation from the single model by $\Delta\chi^2_{\rm S-P} > 100$ with online MOA data alone. The mass ratio is $q \sim 5 \times 10^{-4}$.

MOA-2012-BLG-100: the light curve around the peak is asymmetric due to the resonant caustic crossing. The mass ratio is $q \sim 1.4 \times 10^{-3}$.

Table 5.1: The List of Planetary Events with $\Delta\chi^2_{\rm B-P} > 25$

Event name	$t_{\rm E}$ (days)	u_0	q ($\times 10^{-3}$)	s	$M_{\rm L}$ ($M_\odot$)	$m_{\rm P}$ ($M_\oplus$)	a (AU)	Reference	OGLE ID
MOA-2007-BLG-189	186	0.07	13.7	0.97	0.66	3006	3.1	–	–
MOA-2007-BLG-192	75	0.004	0.2	1.0	0.08	3	0.7	(1)	–
MOA-2007-BLG-308	58	0.08	0.09	0.93	0.64	20	3.3	(2)	(a)
MOA-2007-BLG-379	121	0.002	0.3	0.8	0.35	33	–	–	(b)
MOA-2008-BLG-288	34	0.27	12	0.88	0.37	1462	2.1	–	(c)
MOA-2008-BLG-379	42	0.006	6.9	1	0.56	1303	3.3	(3)	(d)
MOA-2009-BLG-266	61	0.13	0.06	0.91	0.56	10	3.2	(4)	–
MOA-2009-BLG-319	17	0.006	0.4	0.98	0.38	50	2.4	(5)	–
MOA-2009-BLG-387	40	0.09	13.2	0.91	0.19	826	1.8	(6)	–
MOA-2010-BLG-117	185	0.2	0.4	1.04	0.67	112	2.9	–	–
MOA-2010-BLG-328	70	0.07	0.5	1.2	0.11	10	1.0	(7)	–
MOA-2010-BLG-353	15	0.5	1.7	1.2	0.27	152	2.4	–	–
MOA-2010-BLG-477	47	0.003	2.2	1.12	0.67	477	2	(8)	–
MOA-2011-BLG-028	31	1.1	0.12	1.8	0.5	20	5.1	–	(e)
MOA-2011-BLG-197	52	0.13	3.5	1.0	0.6	645	3.3	–	(f)
MOA-2011-BLG-262	4	0.01	0.5	1	0.11	17	0.95	(9)	(g)
MOA-2011-BLG-322	23	0.046	28	1.8	0.39	3686	4.3	(10)	(h)
MOA-2012-BLG-288	30	0.004	2.9	2.4	0.49	475	6.7	–	(i)
MOA-2012-BLG-355	41	0.19	0.39	0.88	0.56	72	2.8	–	–
MOA-2012-BLG-505	4	0.18	0.65	0.83	0.06	11.9	0.59	–	–
MOA-2012-BLG-527	65	0.1	0.21	0.95	0.65	45	3.0	–	(j)

Reference. (1) Bennett et al. (2008); (2) Sumi et al. (2010); (3) Suzuki et al. (2014); (4) Muraki et al. (2011); (5) Miyake et al. (2011); (6) Batista et al. (2009); (7)Furusawa et al. (2013); (8) Bachelet et al. (2012); (9) Bennett et al. (2013); (10) Shvartzvald et al. (2013)

OGLE ID. (a) OGLE-2007-BLG-368; (b) OGLE-2007-BLG-349; (c) OGLE-2008-BLG-335; (d) OGLE-2008-BLG-570; (e) OGLE-2011-BLG-0203; (f) OGLE-2011-BLG-0265; (g) OGLE-2011-BLG-0703; (h) OGLE-2011-BLG-1127;(i) OGLE-2012-BLG-0563; (j) OGLE-2012-BLG-0950

Table 5.2: The List of Planetary Candidates with $4 < \Delta\chi^2_{\rm B-P} < 25$

Event Name	$t_{\rm E}$ (days)	u_0	q ($\times 10^{-3}$)	s	$M_{\rm L}$ ($M_\odot$)	$m_{\rm P}$ ($M_\oplus$)	a (AU)	OGLE ID
MOA-2010-BLG-330	47	0.002	3.5	2.0	0.58	682	6.3	–
MOA-2011-BLG-291	44	0.004	0.5	0.8	0.57	94.6	2.5	–
MOA-2012-BLG-100	118	0.049	1.4	0.97	0.66	316	3.3	(k)

OGLE ID. (k) OGLE-2012-BLG-0295

Table 5.3: The List of Planetary Candidates with $0 < \Delta\chi^2_{\rm B-P} < 4$

Event Name	$t_{\rm E}$ (days)	u_0	q ($\times 10^{-3}$)	s	$M_{\rm L}$ ($M_\odot$)	$m_{\rm P}$ ($M_\oplus$)	a (AU)	OGLE ID
MOA-2010-BLG-190	66	0.01	14.9	0.7	0.62	3089	2.3	–
MOA-2012-BLG-155	27	0.07	19.6	0.6	0.46	2986	1.7	(l)
MOA-2012-BLG-201	43	0.05	3.4	1.1	0.57	648	3.3	(m)

OGLE ID. (l) OGLE-2012-BLG-0313; (m) OGLE-2012-BLG-0501

5.2 Detection Efficiency to Planets

In microlensing event, detection efficiency, $\epsilon(\log s, \log q)$ is the probability that a planet with its mass ratio, q at the distance from the host star, s is detected if one planet exist at the parameter space. We use the logarithm expression for the convenience and assume the planet distribution is uniform on $\log s$ and $\log q$. Following Rhie et al. (2000), $\Delta\chi^2_{\rm S-P} = \chi^2_{\rm S} - \chi^2_{\rm P}$ is used for the detection. This assessment of χ^2 excess is same with the significance in Section 5.1.3. We divide the angle of the source trajectory, α into 90 grids within $0 \leq \alpha \leq 2\pi$ and define $\epsilon(\log s, \log q)$ as the fraction of $\Delta\chi^2_{\rm S-P}(\log s, \log q, \alpha) > \chi^2_{\rm thres}$. Since the microlensing is less sensitive to inner planets $s < 0.1$ and outer planets $s > 10$, s is logarithmically divided into 40 bins within $0.1 \leq s \leq 10$. As for the grid of q, because it is known that efficiency is smoothly depending on q, we divided q logarithmically into 6 bins within $10^{-5} \leq q \leq 10^{-2}$ to reduce computation time.

5.2.1 Threshold for the Planet Detection

Gould et al. (2010b) that analyzed high-magnification events used very conservative value for the detection threshold, $\chi^2_{\rm thres} = 500$. Such a conservative value is required because the high-magnification events in Gould et al. (2010b) are densely covered by the small aperture and unfiltered telescopes over the peak where the anomaly occurs. Also, especially in the high-magnification events, the data points over the peak strongly affect the estimation of single lens model parameters. In the low-magnification events, however, the anomaly, which often occurs at the wing of the light curve, is irrelevant to the estimation of the single lens model parameters. This should leads to lower threshold to identify the planet signal in the low-magnification events (Yee et al. 2013). In our analysis, $\chi^2_{\rm thres} = 500$ is too conservative because the planets in our analysis are discovered through low-magnification event, which is a different channel from Gould et al. (2010b), and we use only survey data. The anomalies in MOA-2007-BLG-308, MOA-2009-BLG-266 and MOA-2011-BLG-028 should be found in even only survey data because actually they were found from MOA data in realtime. We set the detection threshold $\chi^2_{\rm thres} = 100$ in our analysis. With this threshold, we assume that the detection of the anomaly can trigger follow-up observations and confirm the planetary parameters.

The lower detection threshold yields higher detection efficiency and more planet detections, and vice versa. But, the average number of planets per one star, which is described in Section 5.6, should be consistent with the different detection thresholds, unless the detection threshold is too low to find a lot of false positive signals. We will compare the result with different detection thresholds in Section 5.8.

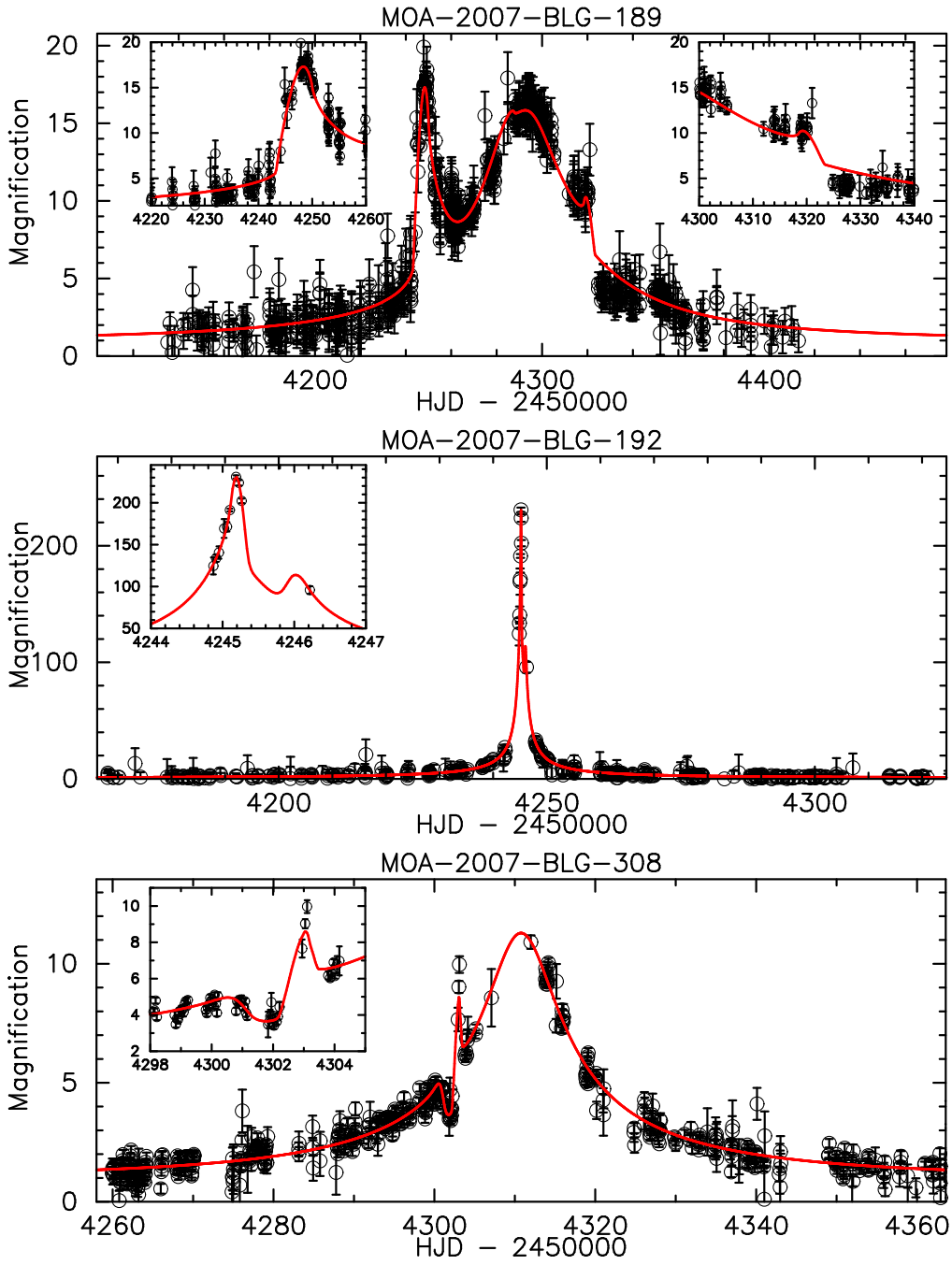

Figure 5.2: Light curves of the planetary events: MOA-2007-BLG-189, MOA-2007-BLG-192, and MOA-2007-BLG-308. The black plots show MOA data. The red lines show the best fit model with finite source effect using only MOA data. The insets show the zoom of anomalies caused by the planetary companion.

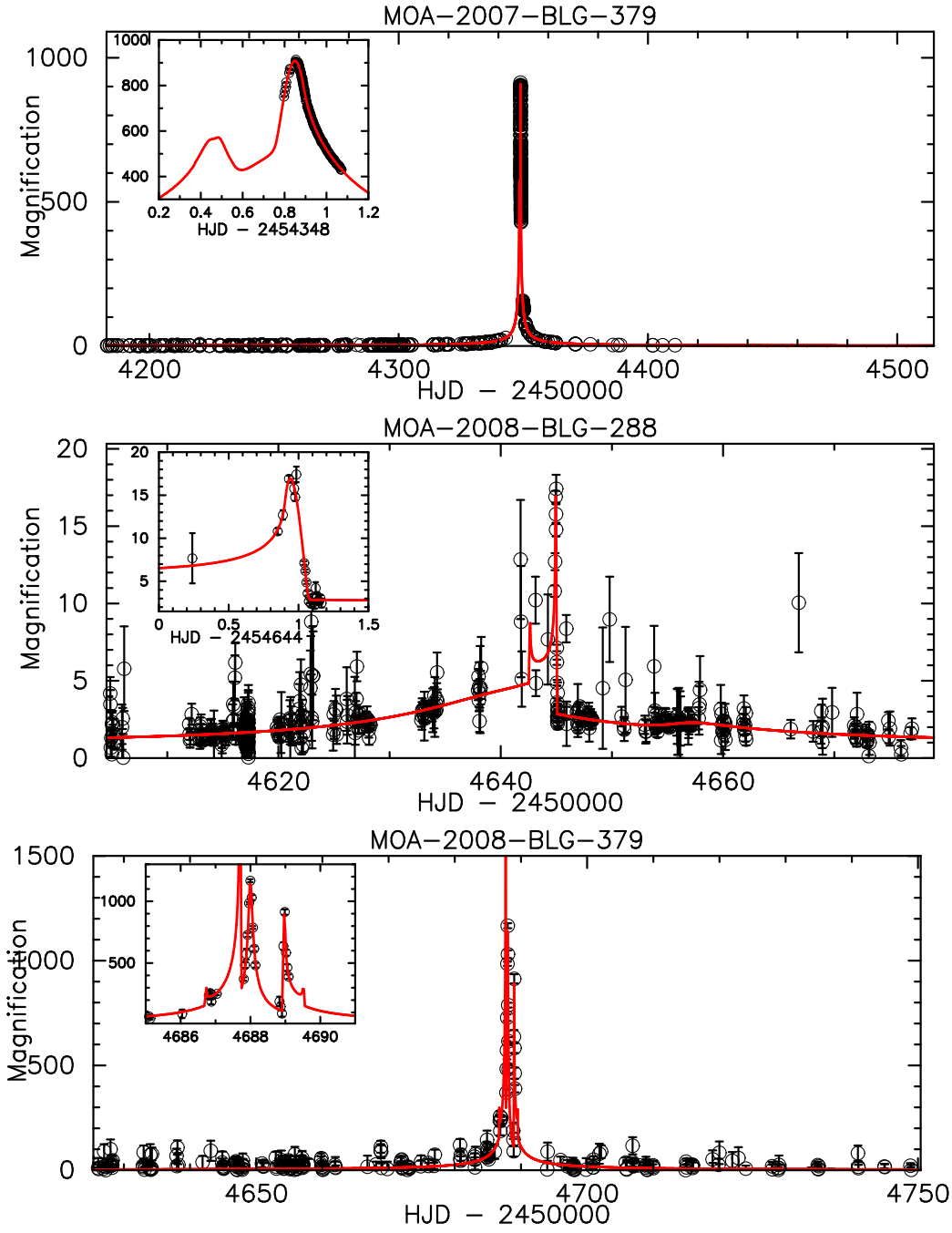

Figure 5.3: Same as Figure 5.2, but for MOA-2007-BLG-379, MOA-2008-BLG-288, and MOA-2008-BLG-379.

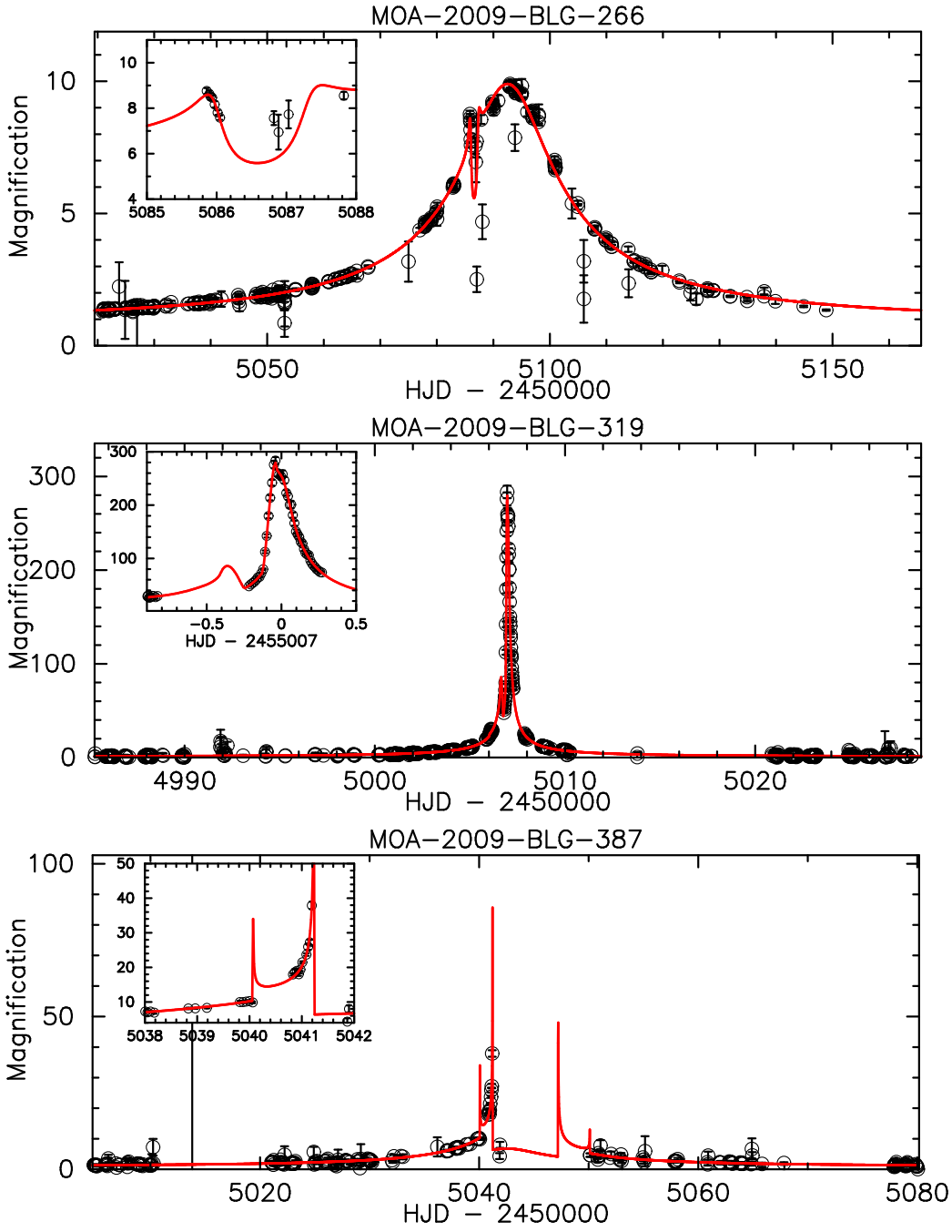

Figure 5.4: Same as Figure 5.2, but for MOA-2009-BLG-266, MOA-2009-BLG-319, and MOA-2009-BLG-387.

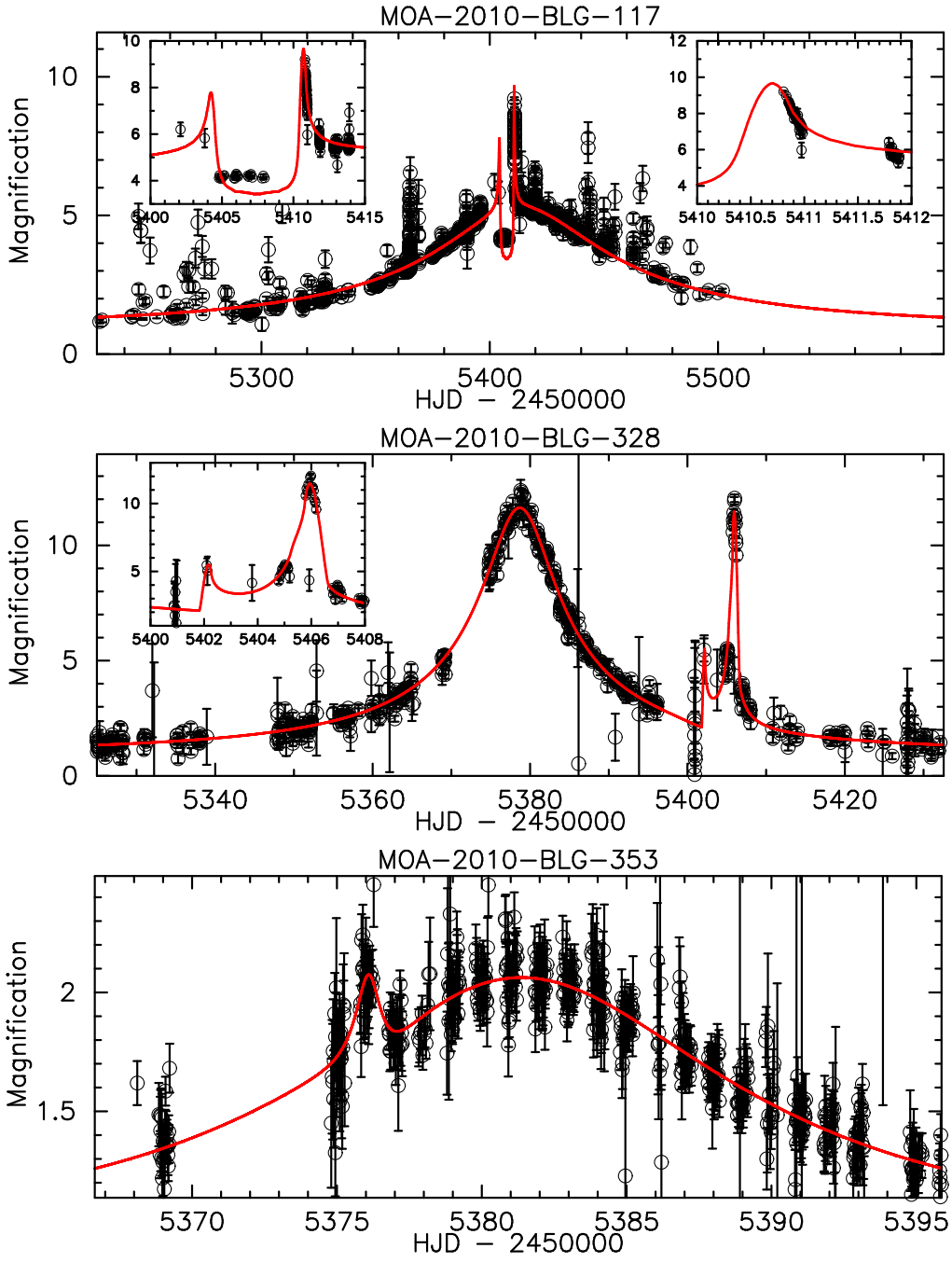

Figure 5.5: Same as Figure 5.2, but for MOA-2010-BLG-117, MOA-2010-BLG-328, and MOA-2010-BLG-353.

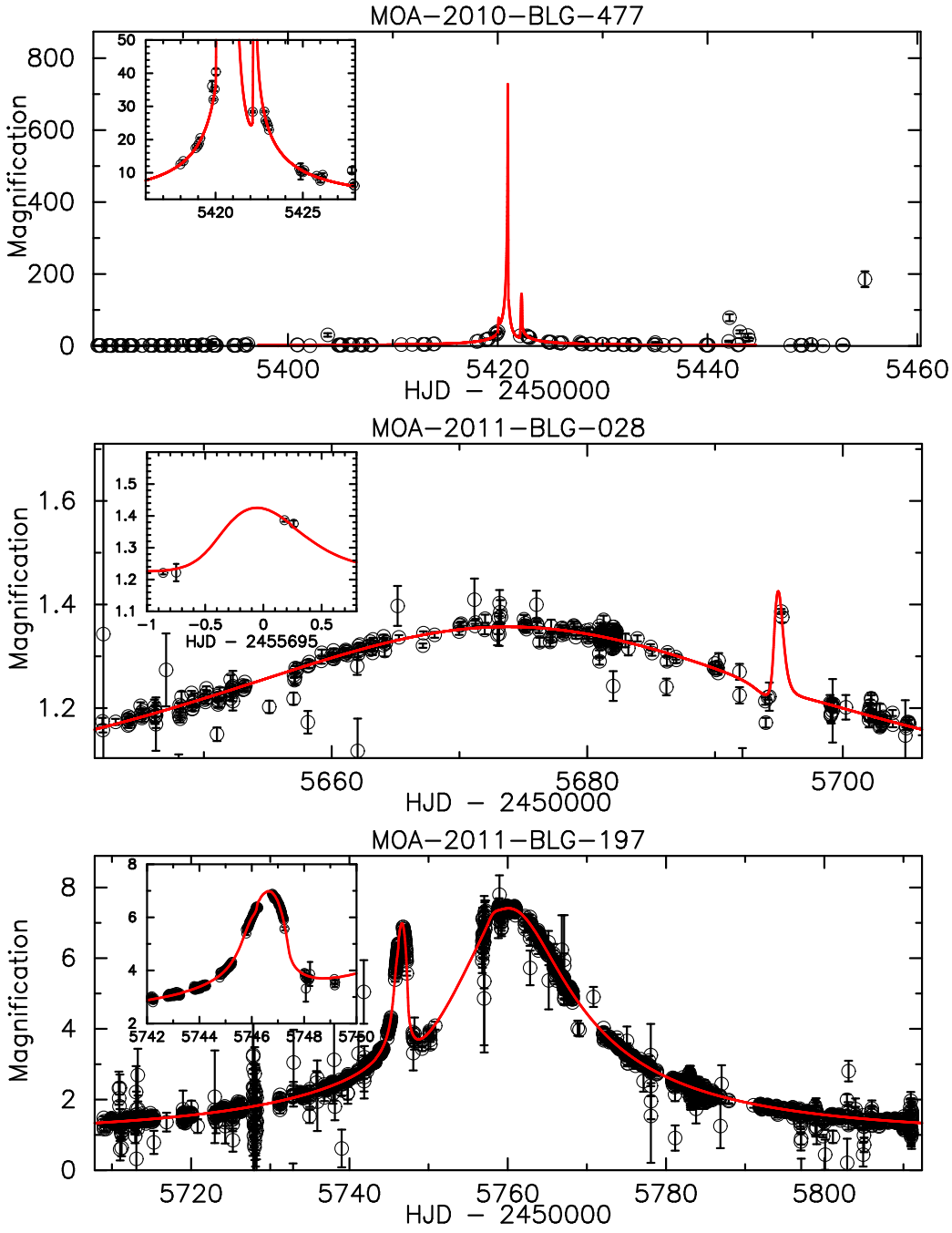

Figure 5.6: Same as Figure 5.2, but for MOA-2010-BLG-477, MOA-2011-BLG-028, and MOA-2011-BLG-197.

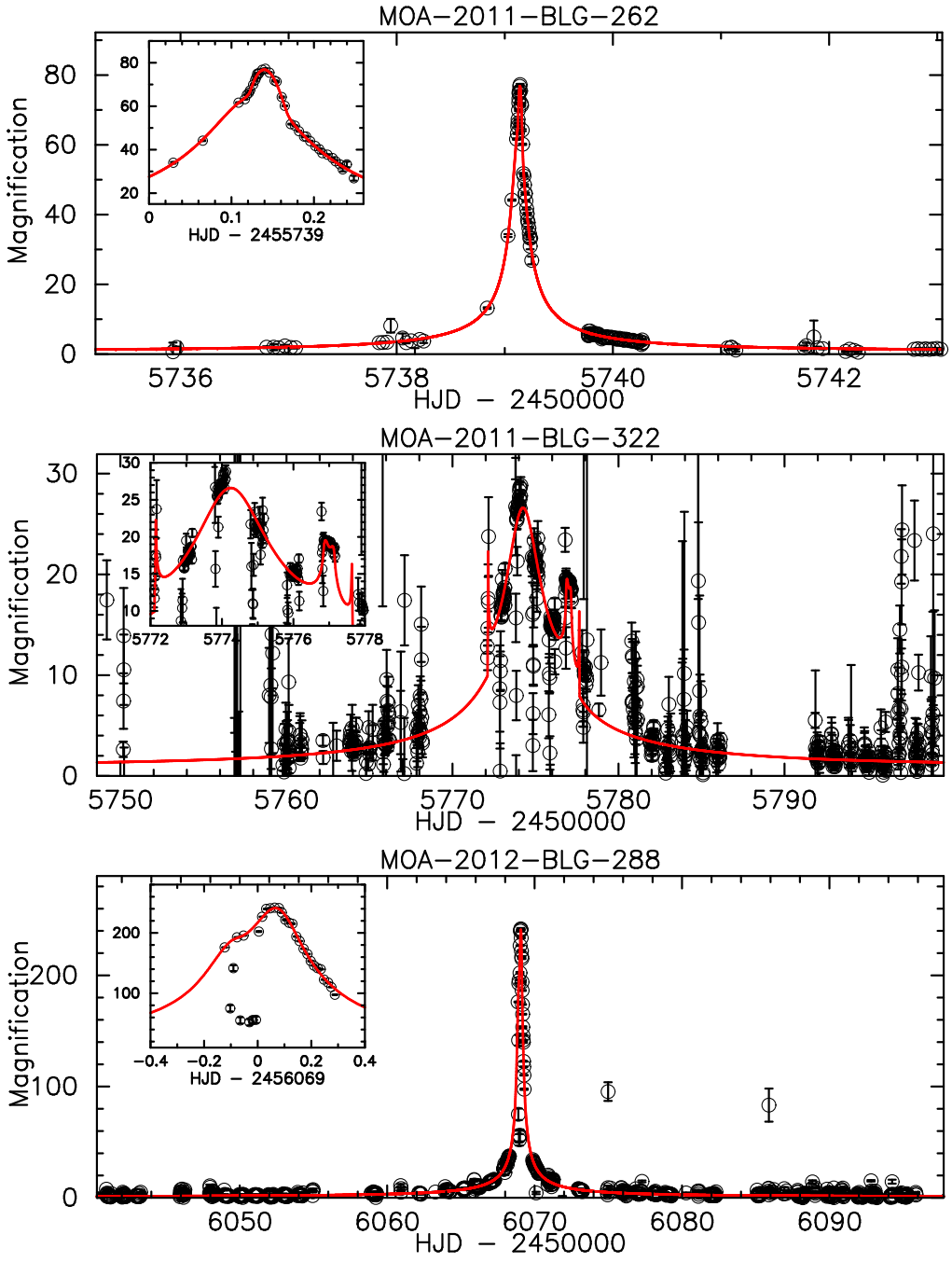

Figure 5.7: Same as Figure 5.2, but for MOA-2011-BLG-262, MOA-2011-BLG-322, and MOA-2012-BLG-288.

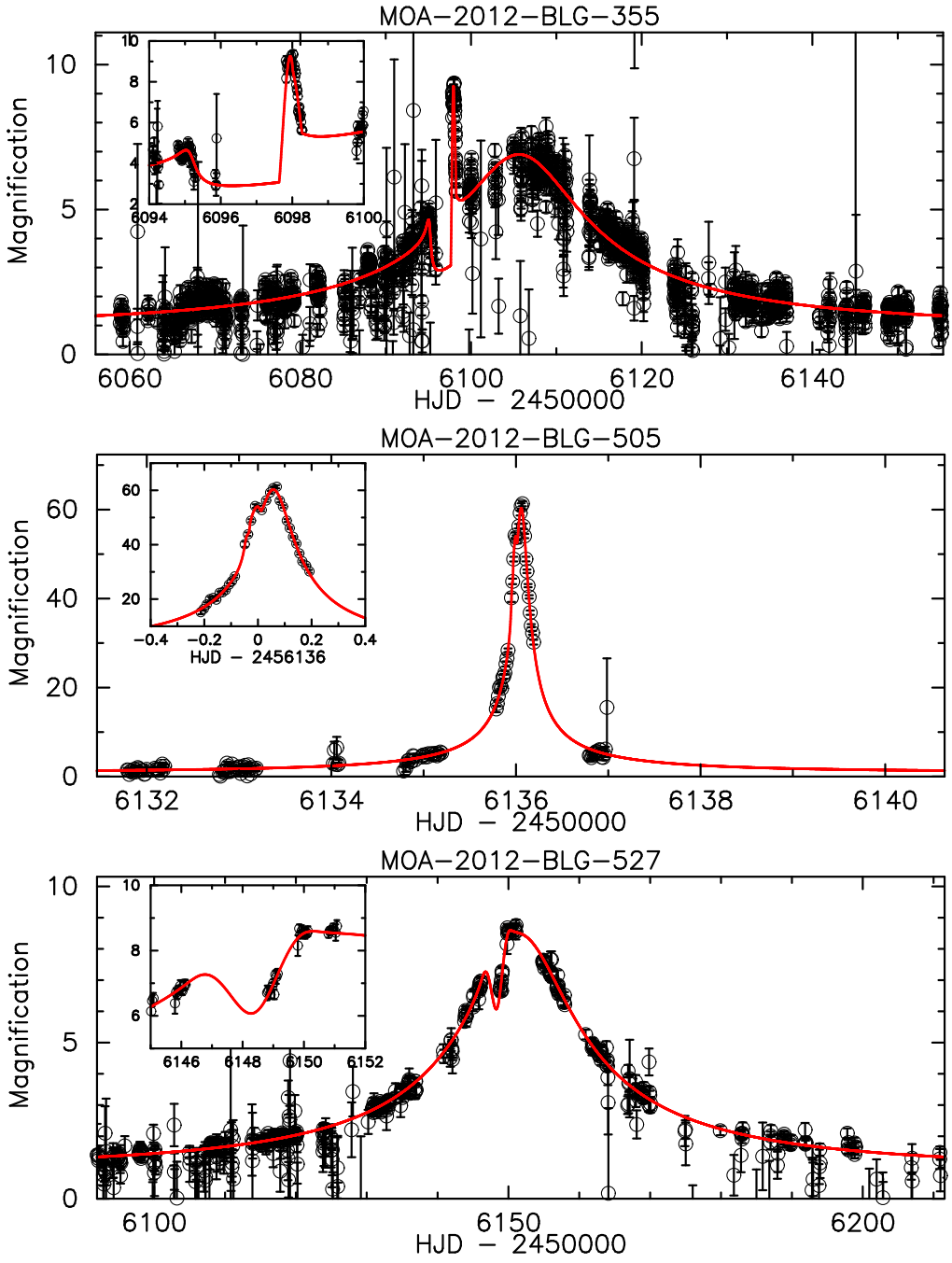

Figure 5.8: Same as Figure 5.2, but for MOA-2012-BLG-355, MOA-2012-BLG-505, and MOA-2012-BLG-527.

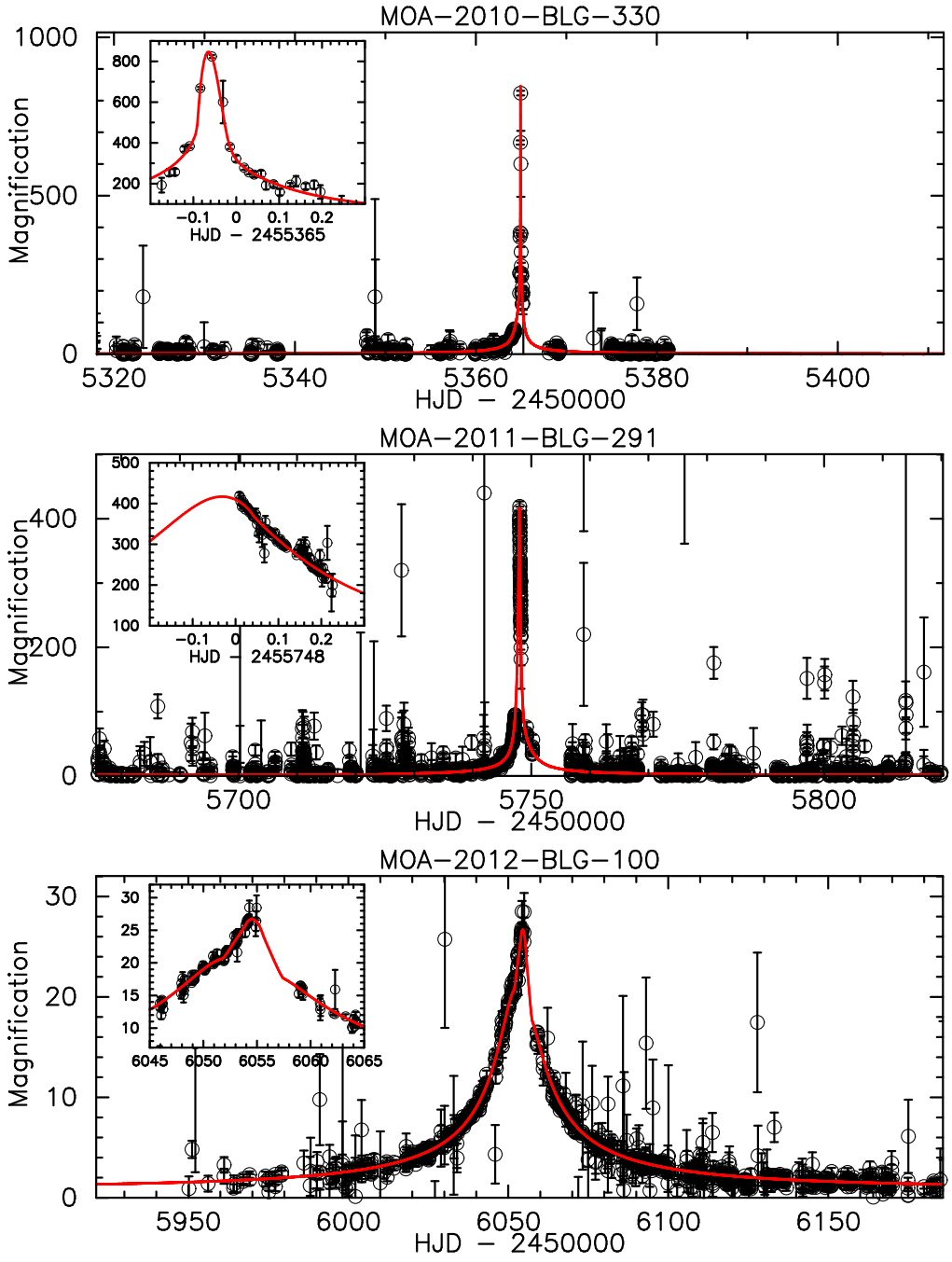

Figure 5.9: Same as Figure 5.2, but for planetary candidates of MOA-2010-BLG-330, MOA-2011-BLG-291 and MOA-2012-BLG-100.

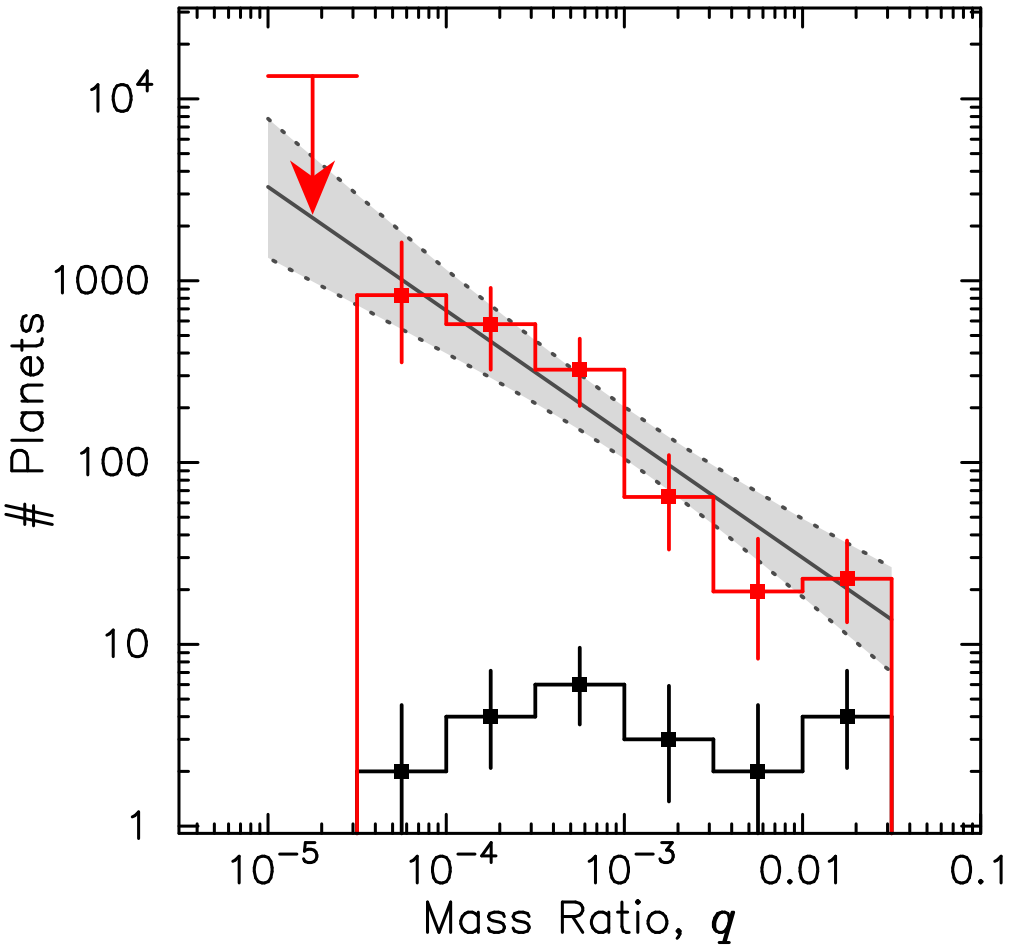

Figure 5.10: Mass ratio distribution of the planets in this analysis. The black histogram shows the 21 detected planets. The red histogram shows the number of planets corrected by the detection efficiency. The red arrow shows the upper limit in the smallest mass ratio bin, where we have null detection. The gray solid line shows the power law fit to the planet frequency (same with Figure 5.13) scaled to the red histogram. The gray shadow area with dotted lines are 68 % confidence interval. Note that the fitting uses unbind data.

5.2.2 Source Star Radius

We include a finite source effect in the model to compute detection efficiency. The finite source effect is given as an additional parameter $\rho = \theta_*/\theta_{\rm E}$, the source star angular radius divided by the angular Einstein radius. The finite size of the source star affects the detection efficiency by both decreasing the light curve deviation and extending the detectable region (Bennett & Rhie 1996). For the published events, we use the finite size of the source star in the each paper. For the events with high-magnfication or giant source star, we used the ρ derived from single lens model fitting. For the other events, we need to derive ρ by estimating both angular source star radius θ_* and angular Einstein readies $\theta_{\rm E}$. In the typical microlensing events, θ_* can be estimated from the source star color and magnitude (Kervella and Fouqué 2008). In 2007-2012, however, we do not have the information of source star color, since MOA surveyed with using only MOA-Red wide-band filter, which is equivalent with the sum of the standard Kron/Cousins R and I-band.

To estimate intrinsic source star color, we use color-magnitude diagram (CMD) toward the Baade's window taken by the *Hubble Space Telescope* (*HST*) (Holtzman et al. 1998). The procedure we use is the following three steps. First, from the reference images of V and I -band we make CMD and estimate reddening and extinction using red clump giant (RCG) as a standard candle. Here, we adopt the Galactic bulge RCG magnitude $M_{I,{\rm RC},0} = -0.15 \pm 0.05$ from Bensby et al. (2011) and color $(V-I)_{\rm RC,0} = 1.06 \pm 0.06$ from Bensby et al. (2011). Second, using RCG color and magnitude from *HST* $(V-I, I)_{{\rm RC},HST} = (15.15, 1.62)$ (Bennett et al. 2008), we convert the dereddened source star magnitude $I_{\rm S}$ to the *HST* frame $I_{{\rm S},HST}$ and estimate source star color $(V-I)_{{\rm S},HST}$ by averaging corresponding color. Finally, we convert $(V-I, I)_{{\rm S},HST}$ to $(V-I, I)_{\rm S}$ and estimate intrinsic source star color and magnitude $(V-I, I)_{\rm S,0}$ by correcting the reddening and extinction (Rattenbury et al. 2007).

Using $(V-I, I)_{\rm S,0}$ with the relation of optical color and brightness-radius (Kervella and Fouqué 2008), we can estimate $\rho = \theta_*/\theta_{\rm E} = \theta_*/(\mu \times t_{\rm E})$ assuming that a source-lens relative proper motion μ is the typical value of the bulge-source-bulge-lens event, $\mu = <\mu> \simeq 5.2$ mas yr^{-1} (Bennett et al. 2013).

5.2.3 Detection Sensitivity in Mass Ratio

We compute the detection efficiency $\epsilon(\log s, \log q)$ in each event, which we chose in Section 5.1.2, and define the detection sensitivity as the summation of the detection efficiency in each event,

$$S(\log s, \log q) \equiv \sum \epsilon(\log s, \log q), \tag{5.1}$$

which is the number of total expectation of planets if we assume that the flat distribution for planets on log$s$ and log$q$.

Figure 5.11 shows $S(\log s, \log q)$ that has a triangular shape in the sensitivity contour as many previous studies show (Rhie et al. 2000, Gaudi et al. 2002, Dong et al. 2006, Yee et al. 2009, Batista et al. 2009, Gould et al. 2010b, Choi et al. 2012). This figure has a small difference with that of the previous works in the symmetricity of log$s$. Most of the previous works analyzed only high-magnification events in which the anomaly would arise from the central caustic and resonant caustic. The high-magnification events are densely covered by the follow-up telescopes over the peak of the light curve due to the potential high sensitivity to the planets. This provides the high sensitivity to the planet irrelevant to separation s. On the other hand, in the low-magnification events, which is dominant in our sample, the anomaly would arise from the planetary caustics or resonant caustic. Our events have enough sensitivities to the planets, but they are not very high compared to the high-magnification events. Because the anomaly in $s < 1$ is relatively large due to the negative perturbation (unless the caustic sizes are too small for the source star size), the sensitivity in $s < 1$ is slightly higher than that of $s > 1$. To get the total sensitivity as a function of log$q$, we integrate $S(\log s, \log q)$ over log$s$

$$S(\log q) = \int_{\log s_-}^{\log s_+} S(\log s, \log q) d \log s, \tag{5.2}$$

where $s_- \leq s \leq s_+$ is $0.1 \leq s \leq 10$. Figure 5.12 shows $S(\log q)$, where we interpolate the sensitivity with a quartic polynomial, $S = a_1 x^4 + a_2 x^3 + a_3 x^2 + a_4 x + a_5$, where $x = \log q$.

5.3 Planetary Mass Ratio Function

We define mass ratio function f as a number of planets per star per decade of massratio q per decade of normalized separation s,

$$f \equiv \frac{dN}{d \log s \; d \log q} = A \left(\frac{q}{q_0} \right)^n, \tag{5.3}$$

where N is an averaged number of planets around a star, and we assume that the mass ratio function can be described as a power law with a normalization factor A and a slope of the power law n. To estimate A and n, we use a likelihood analysis. The likelihood function is written as,

$$L(A, n) = -N_{\rm exp} + \sum_i^{N_{\rm obs}} \ln f(q_i) S(\log q_i); \quad N_{\rm exp} = \int_{q_-}^{q_+} dq f(q) S(\log q) \tag{5.4}$$

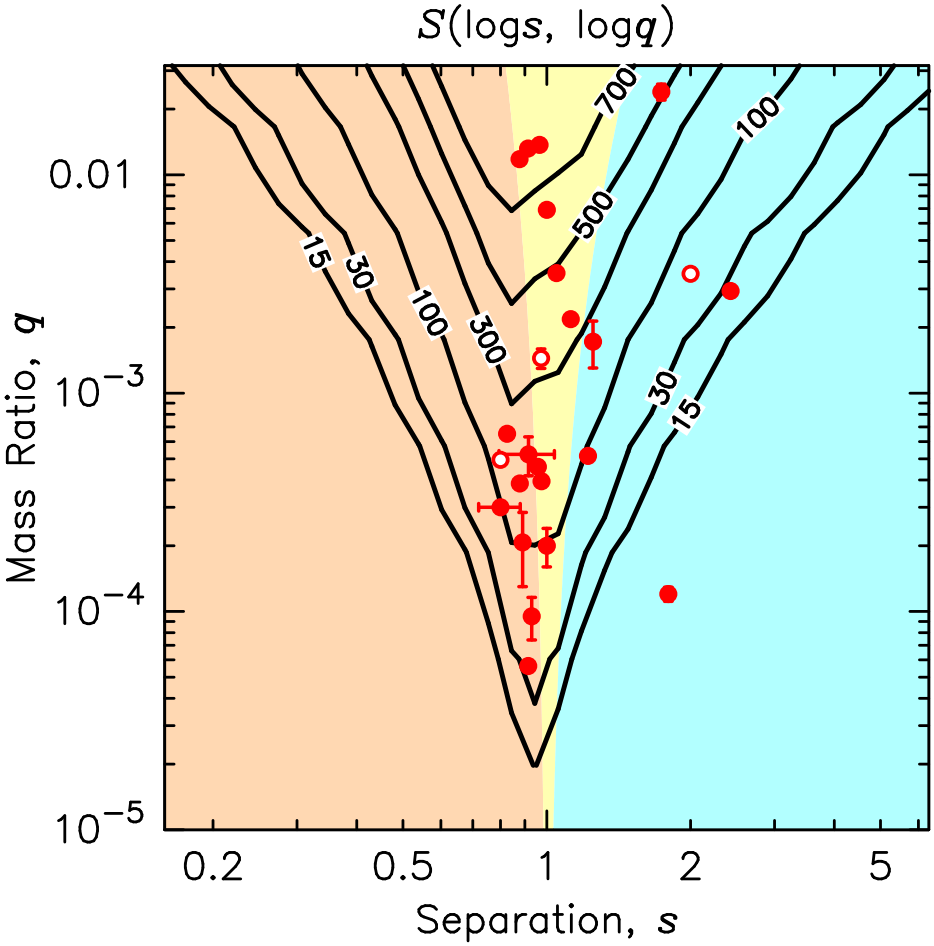

Figure 5.11: Detection sensitivity as a function of log$s$ and log$q$, $S(\log s, \log q)$. The detection sensitivity is the summation of the detectable planets if one planet exists at each log$s$, log$q$ bin. The contours show the expected number of 15, 30, 100, 300, 500 and 700 planets from outside to inside. The red filled circles with the error bars indicates the 21 planets to be included this analysis. The red open circles are the planet candidates with $4 < \Delta\chi^2_{\rm B-P} < 25$ discovered in the systematic modeling, but below the selection threshold. The background color shows the geometry of caustics: the pale red for the close geometry, the pale yellow for the the resonant caustic, and the light blue for the wide geometry (see also Figure 2.4).

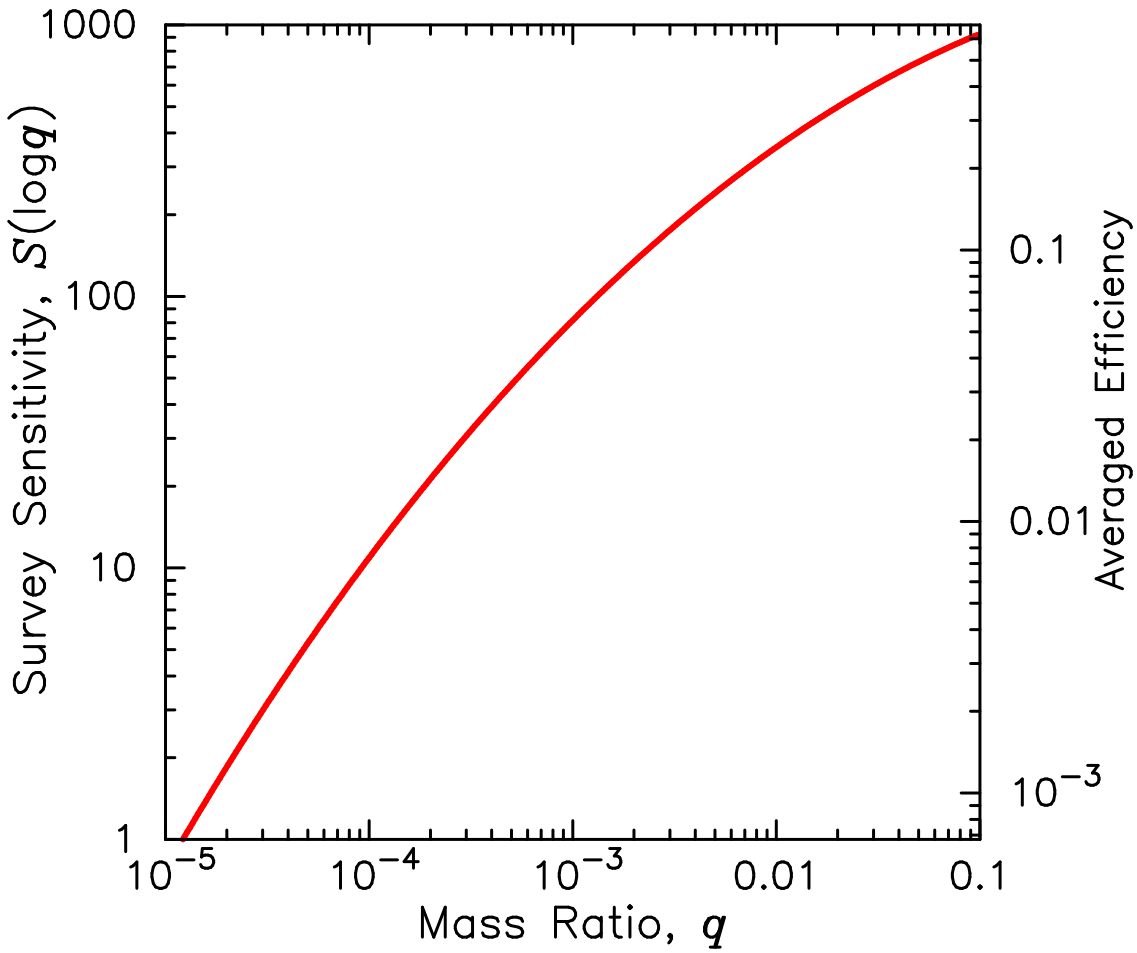

Figure 5.12: Detection sensitivity as a function of $\log q$ $S(\log q)$, which is derived by integrating $S(\log s, \log q)$ over $\log s$ within $0.1 \leq s \leq 10$. The right hand vertical axis shows the averaged detection efficiency, which is the survey sensitivity divided by the number of total observed events.

where $N_{\rm obs}$ is 21, the number of the detected planets with the separation of $0.1 < s < 10$, and the mass ratio domain is $-4.7 < \log q < -1.5$. We maximize this likelihood function and find

$$A = 0.09 \pm 0.02 \quad (5.5)$$

$$n = -0.69 \pm 0.12, \quad (5.6)$$

with a pivot point $q_0 = 1 \times 10^{-3}$. Figure 5.10 shows the histogram of the mass ratios corrected by the detection efficiency and the derived mass ratio function. Note that the binned histogram is not used for the calculation, but for a view. Figure 5.13 compares the mass ratio function to the previous microlensing works and results from RV methods. The estimated slope of $n = -0.69 \pm 0.12$ is consistent with -0.68 ± 0.2 by Sumi et al. (2010), who estimated the power law index of mass ratio function from 10 planetary microlensing events with rough estimates of detection efficiency. The normalization of $A = 0.09 \pm 0.02$ at $q = 1 \times 10^{-3}$ is also consistent with the previous microlensing work, 0.36 ± 0.15 at $q \sim 5 \times 10^{-4}$ estimated by Gould et al. (2010b), but our value is slightly lower even with considering the mass ratio offset. Cumming et al. (2008) and Howard et al. (2010), which are RV results, surveyed close-in planets around solar type stars. Another RV result, Johnson et al. (2010a) also targeted close-in planets but around late type stars. It is natural that these RV results seem to be inconsistent with the estimates by microlensing because the semi-major axis of planets are very different. By contrast, Bonfils et al. (2013), an RV result for M-dwarfs, estimated the planet frequency with long orbital period, where planets are also detectable by microlensing. Montet et al. (2013) is also an RV result for M-dwarfs, but they estimated the frequency of planets with long orbital period by combining the constraints from their direct imaging observations. These RV results for the planets with long orbital period are consistent with our microlensing result.

5.4 Detection Efficiency in Physical Mass

5.4.1 Event Timescale and Host Star Mass Distribution

Microlensing method can measure the mass of the lens system directly only in some cases. Instead, from the light curve modeling we can know the event timescale $t_{\rm E}$ which is proportional to the square root of the lens mass $M_{\rm L}$. Figure 5.1 shows the $t_{\rm E}$ cumulative distribution of our sample selected in Section 5.1.2. From this figure, we find that the distribution of $t_{\rm E}$ in our sample is almost same with that of Cassan et al. (2012), which also used survey data from OGLE.

To examine the host star mass $M_{\rm L}$, we estimate the probability distribution of the host star mass from the Bayesian analysis with the measured value of $t_{\rm E}$ in each

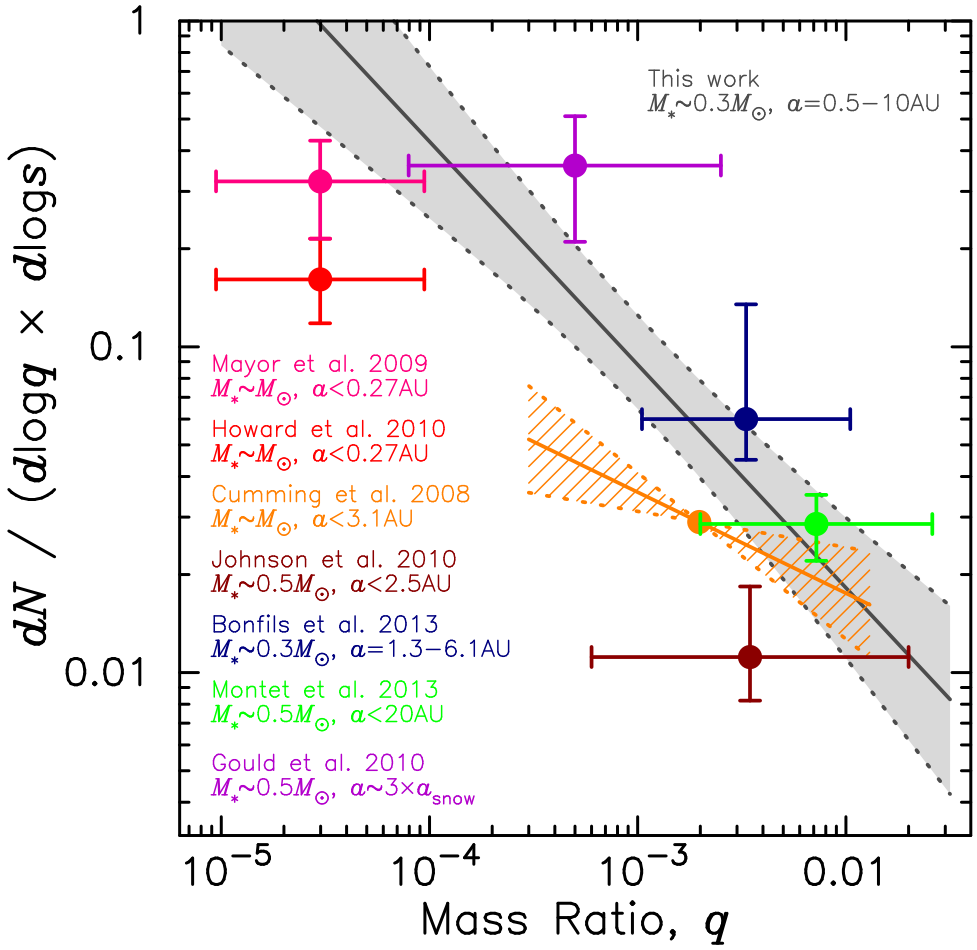

Figure 5.13: Planetary mass ratio function compared to the planet frequency estimated by RV method and previous microlensing. The gray solid line shows our planetary mass ratio function, $f = A(q/q_0)^n$, where $A = 0.10 \pm 0.02$ and $n = -0.68^{+0.12}_{-0.11}$, with 1 sigma uncertainty of the light gray area. Although our mass ratio function is consistent with the previous microlensing results (Gould et al. 2010b), the median value of normalization is slightly lower. Cumming et al. (2008) and Howard et al. (2010), which are RV results, surveyed close-in planets around solar type stars. Another RV result, Johnson et al. (2010a) also targeted close-in planets but around late type stars. It is natural that these RV results seem to be inconsistent with the estimates by microlensing because the semi-major axis of planets are very different. By contrast, Bonfils et al. (2013), the RV result for M-dwarfs, estimated the planet frequency with long orbital period, where planets are also detectable by microlensing. Montet et al. (2013) is also an RV result for M-dwarfs, but they estimated the frequency of planets with long orbital period by combining the constraints from their direct imaging observations. These RV results for the planets with long orbital period are consistent with our microlensing result.

event, as we do in the events with neither finite source nor parallax effects. We use the mass function of Sumi et al. (2011:Table S3), model #1 and the Galactic model (Han & Gould 2003) assuming the distance to the Galactic center is 8 kpc.

The resulted host star mass ranges $0.09 < M_{\rm L}/M_{\odot} < 0.73$ with 68 % confidence interval. The median value is $M_{\rm L} = 0.32\ M_{\odot}$. This range of the host star distribution is consistent with Cassan et al. (2012) that probed stars with the mass range from 0.14 to 1.0 $M_{\odot}$. The difference of the high mass cut comes from the difference of the mass function. We use $M_{\rm L}$ in the each event to compute the detection sensitivity as a function of planetary mass in Section 5.4.2.

5.4.2 Detection Sensitivity in Planetary Mass

What we can derive from $S(\log q)$ is mass ratio function. Although the mass ratio function is important and irrelevant to the Galactic model, a planetary mass function is also interesting to compare our result with the result from other observations and simulations. To estimate the planetary mass function, $S(\log q)$ should be converted to $S(\log m_{\rm P})$, the sensitivity as a function of the logarithm of physical planetary mass. Following Dominik (2006), we use the host star mass $M_{\rm L}$ and the distance to the lens system $D_{\rm L}$ estimated in Section 5.4.1 to derive $\epsilon(\log r_{\perp}, \log m_{\rm P})$, where $r_{\perp}$ is the projected separation in AU. Assuming random inclination and phase with circular orbit, we convert $\epsilon(\log r_{\perp}, \log m_{\rm P})$ to $\epsilon(\log a, \log m_{\rm P})$, where a is the physical three-dimensional separation.

Figure 5.14 shows $S(\log a, \log m_{\rm P})$, which is a summation of $\epsilon(\log a, \log m_{\rm P})$ in each event. Although more Jupiter mass planets are expected than Neptune mass planets from the 6 years observations, the observed planet distribution is rather flat. From this, we can expect that cold Neptunes are common than giant planets as expected in Sumi et al. (2010). The top panel in Figure 5.15, shows $S(\log m_{\rm P})$ that is given by integrating $S(\log a, \log m_{\rm P})$ over $\log a$.

5.5 Planetary Mass Function

The event timescale $t_{\rm E}$ is a degenerate combination of the mass, distance and velocity of the lens. If both finite source and parallax effects are detected in the light curve, the degeneracy can be broken (Muraki et al. 2011, Tsapras et al. 2013). Otherwise, we use Bayesian analysis to estimate the parameters using a Galactic model (Suzuki et al. 2014:e.g.). In most of the planetary events, finite source effect is detected but parallax effect is not robustly detected (Miyake et al. 2011, Furusawa et al. 2013). In some of the planetary events very high precision adaptive optics images were taken and the results were included in the Bayesian analysis as constraints (Sumi et al. 2010, Janczak et al. 2010). But the mass uncertainty

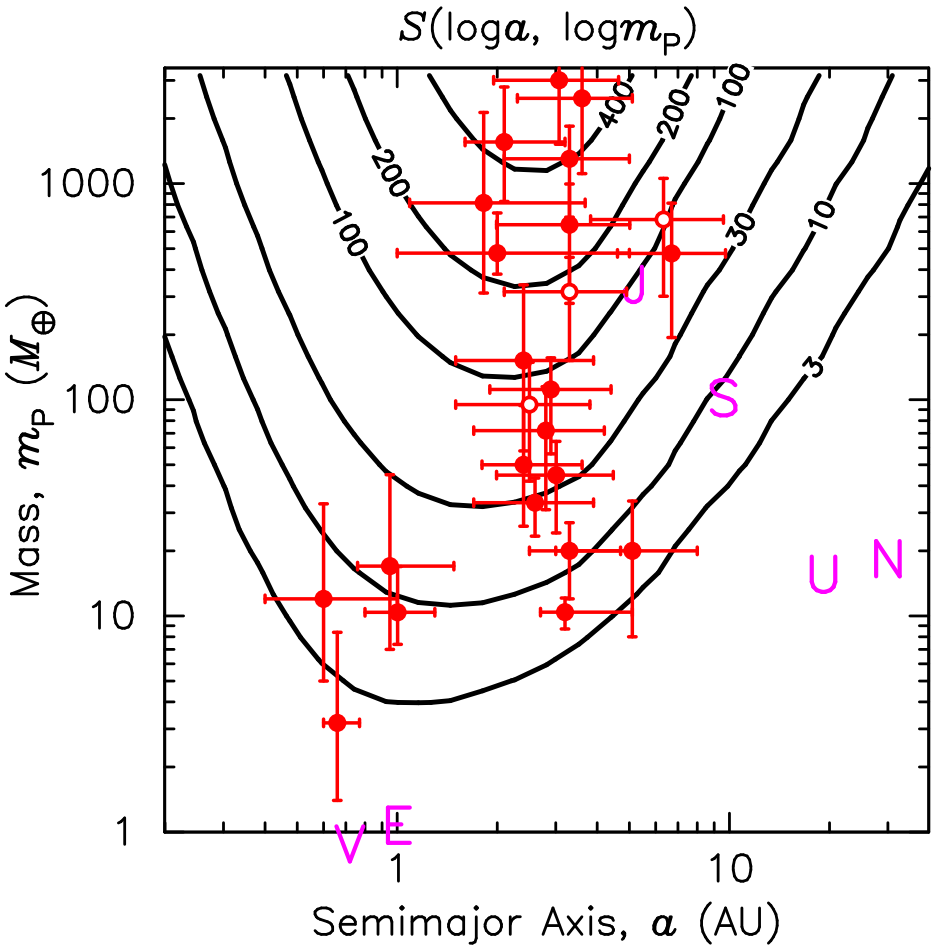

Figure 5.14: Detection sensitivity as function of semi major axis and mass, $S(\log a, \log m_{\rm P})$. This is estimated by the Bayesian analysis using $S(\log s, \log q)$ in each events. The contours show the expected number of the planets in 2007–2012 if we assume that one planet exists at the each $\log a$, $\log m_{\rm P}$ bin. The red filled circles are the 21 planets listed in Table 5.1. The red open circles show the planet candidates with $4 < \Delta\chi^2_{\rm B-P} < 25$ listed in Table 5.2. The alphabets indicate the initial of the solar system planets.

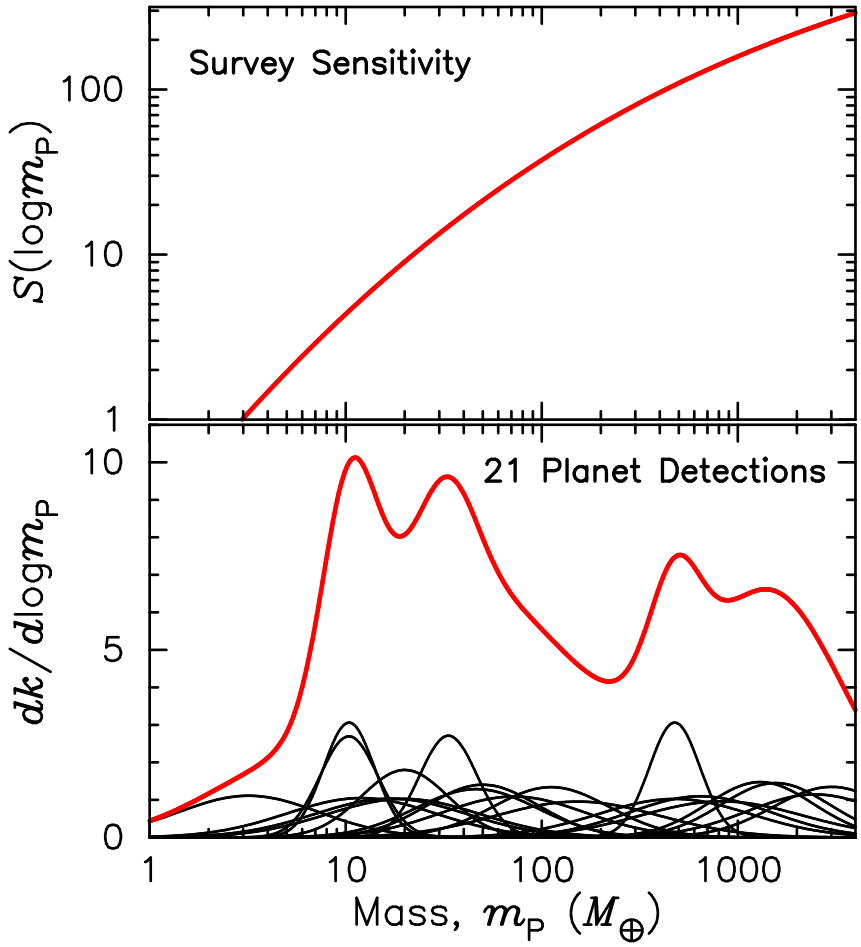

Figure 5.15: Top: Survey sensitivity $S(\log m_{\rm P})$, which is the number of planets expected by our survey observations within 0.5-10 AU. Bottom: Mass distribution of the 21 planets. The black curves show the each detection that has a gaussian distribution. The planet mass and its error are cited from the each paper. The summation of the black curves are drawn in the red curve.

from the Bayesian estimate with the constraints is larger than that of the events with both finite source and parallax effects detected, where the degeneracy in $t_{\rm E}$ is totally broken. Taking into account the mass uncertainty, we estimate planetary mass function F, the number of planets per star per decade of planet mass $m_{\rm P}$ and per decade of three-dimensional separation a,

$$F \equiv \frac{dN}{d\log a\, d\log m_{\rm P}}. \tag{5.7}$$

Following Cassan et al. (2012), we estimate posterior probability $P(\log F|k)$ using Bayesian estimate,

$$P(\log F|k) = \frac{P(k|E)P(\log F)}{\int P(k|E)P(\log F)\mathrm{d}\log F}, \tag{5.8}$$

where $P(k|E)$ is a Poisson distribution,

$$P(k|E) = \frac{E^k \exp(-E)}{k!}, \tag{5.9}$$

the probability of k detections. E is the expected number of the detection with any given planetary mass function F,

$$E = \iint S(\log a, \log m_{\rm P})F(\log a, \log m_{\rm P}) d\log a\, d\log m_{\rm P}. \tag{5.10}$$

We adopt a uniform prior distribution $P(\log F) = 1$ as the previous works do so. Here, the integration range for the semi-major axis is $0.5 < a < 10$ AU, where the detection sensitivity is enough high.

Figure 5.15 shows the planetary distribution of the 21 planets in our sample. Each detection has a normal distribution with the error bars from the discovery paper if the event has been already published. As for the other planetary events, we use the error bars from our Bayesian estimate. They are normalized such that each distribution satisfies,

$$\int \left(\frac{dk}{d\log m_{\rm P}}\right)_i d\log m_{\rm P} = 1. \tag{5.11}$$

The summation of the each detection $dk/d\log m_{\rm P}$ are shown in red curve in Figure 5.15.

Dividing $\log m_{\rm P}$ into 75 bins within $0.5 < \log m_{\rm P} < 3.5$, we calculate $P_j(\log F|k)$ in the jth mass bin. The calculated $P_j(\log F|k)$ are shown in Figure 5.16.

Assuming that the planetary mass function is described by power law

$$F = F_0(m_{\rm P}/m_0)^{\alpha}, \tag{5.12}$$

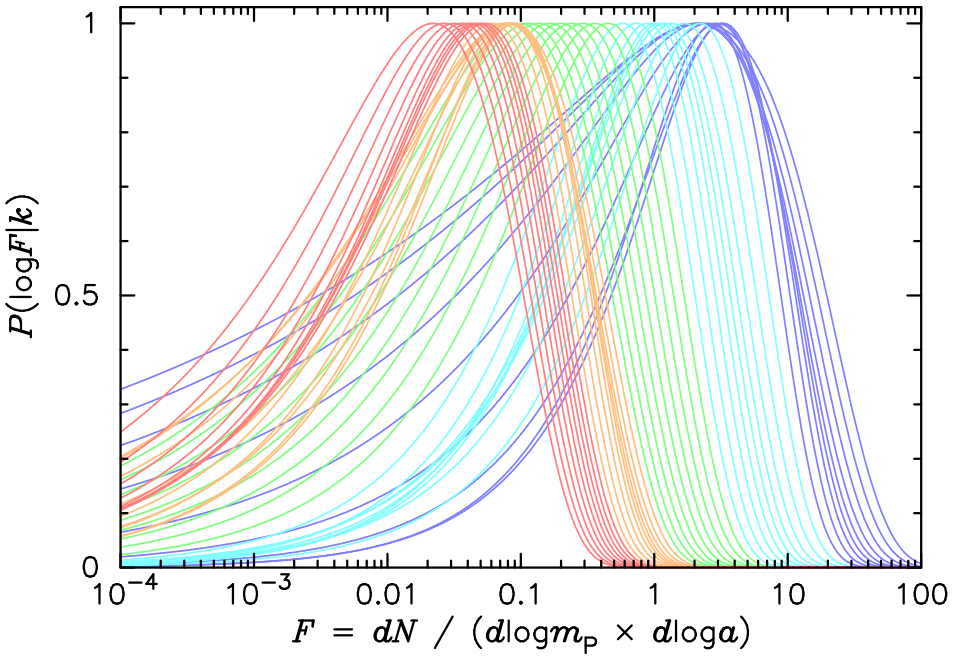

Figure 5.16: Posterior probability $P(\log F|k)$. This figure is basically same with Cassan et al. (2012:Figure S4). Each curve shows ith probability of $P_j(\log F|k)$. We divide $\log m_{\rm P}$ into 75 bins within $0.5 < \log m_{\rm P} < 3.5$. The blue curves are the probability for low-mass planets and red curves are for high-mass planets.

we maximize the likelihood function to estimate the normalization factor F_0 and the power law index α. The likelihood function can be written as,

$$\mathcal{L}(F_0, \alpha) = \prod_j P_j(\log F|k) \tag{5.13}$$

and we find

$$F_0 = 10^{-0.67\pm0.10} \tag{5.14}$$

$$\alpha = -0.78 \pm 0.12, \tag{5.15}$$

with a pivot point of the Saturn mass $m_0 = 95.2 M_\oplus$, which is a same value with Cassan et al. (2012) to allow a direct comparison. The likelihood contours for the normalization and slope are drawn in Figure 5.17. Our power law mass function is drawn in Figure 5.18 with the previous microlensing results (Gould et al. 2010b, Cassan et al. 2012), the RV results targeting more massive solar type stars (Cumming et al. 2008, Mayor et al. 2009, Howard et al. 2010) and the RV results targeting M-dwarfs (Johnson et al. 2010a, Bonfils et al. 2013, Montet et al. 2013). The estimated planetary mass function is very similar to that of Cassan et al. (2012), $F = 10^{-0.62\pm0.22}(m_{\rm P}/m_0)^{-0.73\pm0.17}$. The uncertainties of the normalization and slope in our planetary mass function are about half of Cassan et al. (2012) since the number of included planets in our analysis are almost three times of them.

As mentioned in Section 5.3, the RV (Cumming et al. 2008, Mayor et al. 2009, Howard et al. 2010) surveys solar type star and finds close-in planets. Thus, the difference in the planetary mass function between microlensing and these RV can be seen. Johnson et al. (2010a) derives the frequency of close-in planets (hot Jupiters) around M-dwarfs, and shows the least frequency. This is consistent with the relation $dN = C m_{\rm P}^{-0.31\pm0.2} P^{0.26\pm0.1}\, d\ln m_{\rm P}\, d\ln P$ (Cumming et al. 2008), and the positive correlation of the planet frequency depending on the host star mass (Johnson et al. 2010b). Bonfils et al. (2013) probed planets around M-dwarfs by RV method and derived the frequency of giant planets with long orbital period of 1.3-6.1 AU. The planets with this long orbital period could be detectable by microlensing, and the derived frequency is consistent with our planet mass function. Montet et al. (2013) combined RV results with the constraints from the direct imaging method and found that the frequency of planet with $a < 20$ AU orbiting M-dwarfs is consistent with Cassan et al. (2012). Our plant mass function also agrees with Montet et al. (2013). Thus, the frequency of giant planets around M-dwarfs could be positive correlation with the orbital period; the frequency is increasing with the increase of orbital period. But, we can not constrain that how far this positive correlation lasts to the longer orbital period. The relative frequency of giant planets to Neptune-like planets is small, as seen in Section 5.6.

Note that this result is dependent on a prior probability that we used in estimating the lens star mass. We assume that the probability of a star having a planet of certain mass ratio is uniform on the star mass.

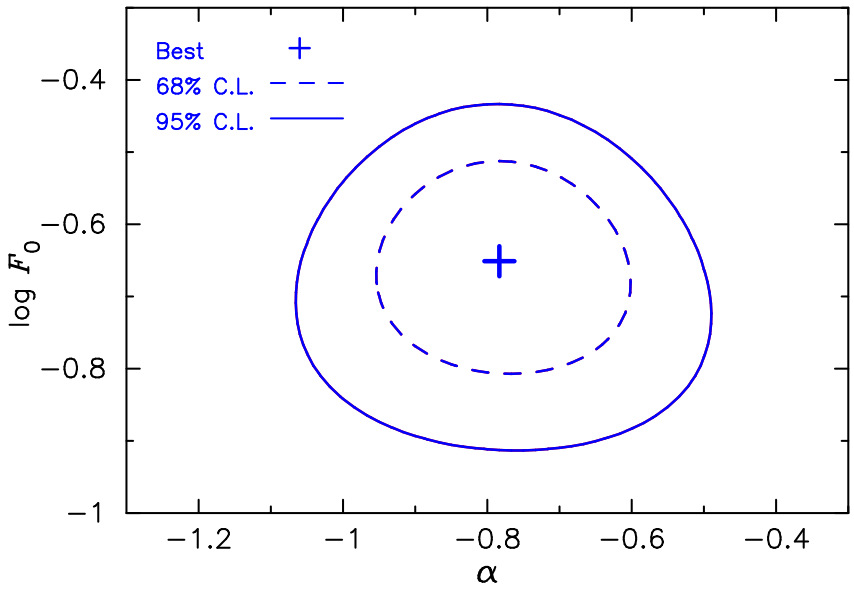

Figure 5.17: Likelihood contours for the normalization and the slope of the planetary mass function. The contours indicate the 68% and 95% confidence intervals. The plus mark shows the maximum likelihood point.

5.6 Planet Abundance

We define the planet abundance N, as the average number of planets per star. Planet abundance can be estimated by integrating our planetary mass function following,

$$N = \iint F_0 \left(\frac{m_{\rm P}}{m_0}\right)^{\alpha} d\log a \, d\log m_{\rm P}. \tag{5.16}$$

The interval of integration for a is from 0.5 to 10 AU for the 21 planet detections. We derive $N = 0.15^{+0.04}_{-0.03}$ for Jupiter like planets ($0.3-10\ M_{\rm Jup}$), and $N = 0.52^{+0.18}_{-0.15}$ for Neptune like planets ($10-30\ M_{\oplus}$). For the planets with mass from 5 $M_{\oplus}$ to 10 $M_{\rm Jup}$, we find $N = 1.6^{+0.52}_{-0.42}$. These values are consistent with Cassan et al. (2012) and the uncertainties are smaller than Cassan's ones.

Montet et al. (2013) first compared the microlesing result with the RV result constrained by the direct imaging. They derived that on average M-dwarf stars

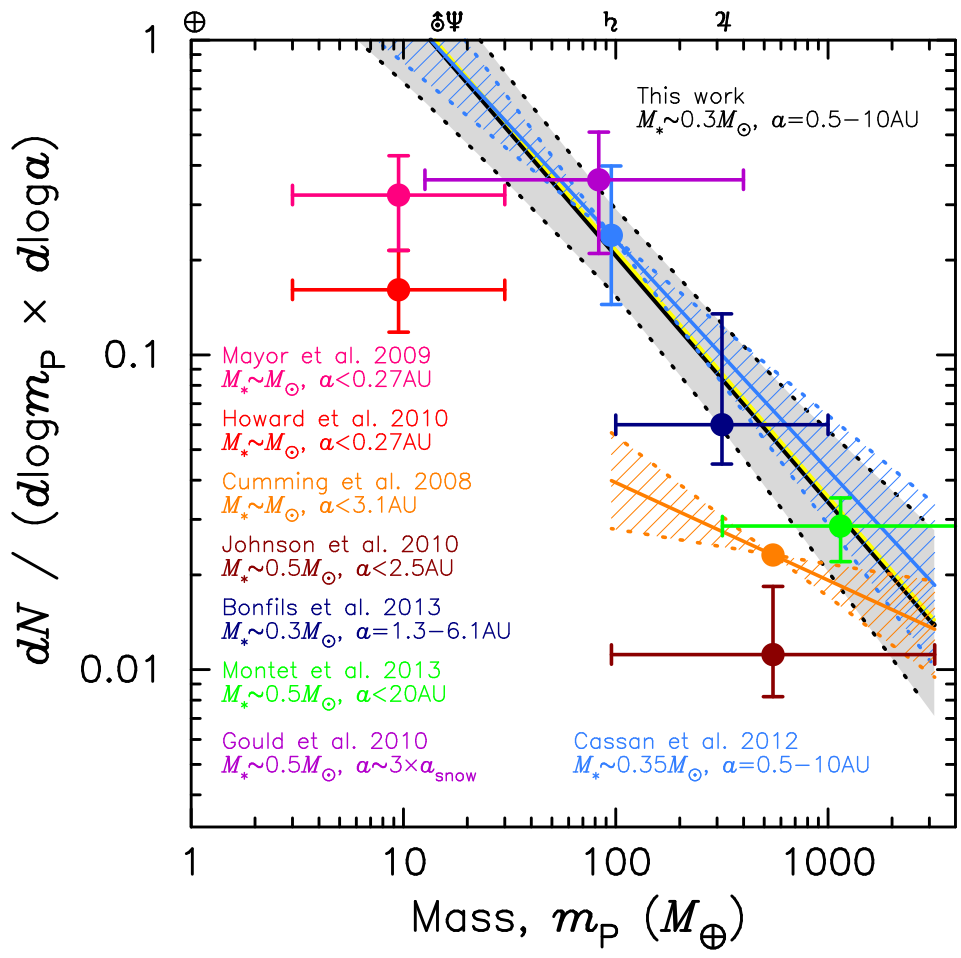

Figure 5.18: Planetary mass function described with the power law $dN/(d\log a\ d\log M) = F_0(M/M_0)^\alpha$. The yellow solid line is our best fit. We find the median values of $F_0 = 10^{-0.67\pm0.10}$ and $\alpha = -0.78 \pm 0.12$, plotted with the black solid line surrounded by 68% confidence interval of the light gray region between the black dotted lines. The violet point indicates the planet frequency derived by Gould et al. (2010b) who analyzed only high magnification events. The blue solid line and shaded region indicate the planetary mass function by Cassan et al. (2012). Our result is consistent with both of them. The orange solid line and shaded region indicate planetary mass function estimated from RV method by Cumming et al. (2008), who targeted close-in planets orbiting solar type stars. Mayor et al. (2009) and Howard et al. (2010) also surveyed close-in planets around solar type stars. Johnson et al. (2010a) probed close-in planets orbiting M-dwarfs. Since these RV paper probes inner planets, the planet frequency is different from that of microlensing. However, Bonfils et al. (2013) and Montet et al. (2013) surveyed planets with long orbital periods around M-dwarfs, and they are consistent with our result. The symbols on the top show the mass of our solar system planets: Earth, Uranus, Neptune, Saturn and Jupiter from the left to right.

have 0.083 ± 0.019 giant planets with 1 $M_{\rm Jup} < m_{\rm P} < 13$ $M_{\rm Jup}$ and $a < 20$ AU. To compare our result with Montet et al. (2013), we calculate the planet frequency with the parameter space of 1 $M_{\rm Jup} < m_{\rm P} < 13$ $M_{\rm Jup}$ and 0.5 AU $< a < 20$ AU. Then, we find that the frequency is 0.06 ± 0.02 for the giant planets and this is consistent with Montet et al. (2013). Note that the parameter space for a in our result is narrower than that of Montet et al. (2013).

5.7 Dependence of Planet Frequency on $t_{\rm E}$

Our planetary mass function and planet abundance are consistent with the previous microlensing results. But, these results are strongly depending on the Bayesian analysis, which is used to estimate the lens star mass and distance to the lens. It is a problem that we assume a prior potability of that a star hosting a planet with a certain mass ratio is uniform on the primary star mass. We do not know the true dependence of planets on the mass of host stars which cause microlensing events, so we used the uniform prior in the Bayesian analysis. Thus, the estimated lens mass could have offsets to the actual mass. One example of such a case is a planetary event MOA-2011-BLG-293. Yee et al. (2012) estimated that the lens star is possibly K-dwarf with mass of $0.59^{+0.35}_{-0.29}$ $M_{\odot}$ orbited by a giant planet with mass of $3.3^{+1.9}_{-1.6}$ $M_{\rm Jup}$ (Batista et al. 2014). But, the high resolution follow-up observation by using Keck adaptive optics (AO) (Batista et al. 2014) resolved the flux from the lens star, and found that the lens star is G-dwarf with mass of 0.86 ± 0.06 $M_{\odot}$ orbited by a planet with mass of 4.8 ± 0.3 $M_{\rm Jup}$. Thus, care must be taken for the results that rely on the Bayesian analysis.

What we can know from the light curve analysis in the most of microlensing events is $t_{\rm E}$, where the lens mass, distance to the lens and transverse velocity are degenerate. For the planetary events, we can derive the mass ratio q and separation s from the light curve model fitting without assuming the prior probabilities. If we have enough sample of the events without the degeneracy in $t_{\rm E}$, i.e. the events with both the finite source and parallax effects (Muraki et al. 2011, Tsapras et al. 2013:e.g.), we can discuss the dependency of the planet frequency on the host star mass and distance to the host star. Although we cannot investigate the dependency of a planet frequency on the host star mass in our sample without any assumed priors, it is interesting to see a dependency of the planet frequency on the event timescale $t_{\rm E}$. Providing a large sample of planet discoveries over different $t_{\rm E}$, this could be possible. The most probable value of the event timescale in single lens events is $t_{\rm E} \sim 20$ days because the most probable lens is an M-dwarf located bulge (see Equation 2.14). But, the discovered planetary events have longer event timescale ~ 60 days, as seen in Figure 5.1. The higher detection efficiency in large $t_{\rm E}$ events might explain this trend. Also, massive host stars or stars located in the

disk with $D_{\rm L}$ of a few kpc possibly make $t_{\rm E}$ longer. Thus, if the planet frequency depends on the host star mass or distance to the lens, these could explain the trend of longer event timescale in the planetary events.

To see the correlation of planet frequency with event timescale $t_{\rm E}$, we should correct the number of detected planets by the detection efficiencies. Figure 5.19 shows the detection efficiencies $\log\varepsilon(\log t_{\rm E}, \log q)$ on a $t_{\rm E}$ - q plane. The detection efficiencies are averaged over $-0.5 < \log s < 0.5$, where the microlensing method is the most sensitive to planets. The events with longer timescale have higher detection efficiency. For the larger mass ratios, the detection efficiency becomes higher. We can see a "hot spot" at $q \sim 10^{-4}$ and $t_{\rm E} \sim 6$ days. For the events of $t_{\rm E} \sim 6$ days with moderate high-magnificaiton or more, the peak of the light curves are fully covered by the high cadence survey observation if the magnification reaches to the peak at midnight and the weather is mild. Unless the good coverage of the light curve, these events fail to the event selection in Section 5.1.2. Thus, the averaged detection efficiency in this area results in relatively high.

We divide the planetary events into two mass ratio ranges; the 12 planets for $-4.5 < \log q < -3$, and 9 planets for $-3 < \log q < -1.5$. Most of the planets in the former range are thought of as terrestrial or cold Neptune planets. The planets in the latter range are gas giant planets. As we studied in Section 5.3, we define $f_{t_{\rm E}}$ as a number of planets per star per logarithmic event timescale,

$$f_{t_{\rm E}} \equiv \frac{dN}{d\log t_{\rm E}} = C_0 \left(\frac{t_{\rm E}}{t_{\rm E\,0}} \right)^{\beta}, \tag{5.17}$$

where N is an averaged number of planets around a star in the mass ratio, separation, and event timescale domain, and C_0 and β are the normalization and slope for an assumed power law function, respectively. To estimate C_0 and β, we use a likelihood analysis. The likelihood function is just the Poisson probability of finding the observed number of events, $N_{\rm obs}$, times the product of the probability of finding events with each of the observed event timescale, $t_{{\rm E}\,i}$. The likelihood function is written as,

$$\mathcal{L}(C_0, \beta) = e^{-N_{\rm exp}} \prod_i^{N_{\rm obs}} f_{t_{\rm E}} \varepsilon(t_{{\rm E}\,i}); \quad N_{\rm exp} = \int_{t_{\rm E}-}^{t_{\rm E}+} dt_{\rm E} f_{t_{\rm E}} \varepsilon(t_{{\rm E}\,i}), \tag{5.18}$$

where $\varepsilon(t_{\rm E})$ is the detection efficiency in each $t_{\rm E}$ bin, and $N_{\rm exp}$ is the number of events expected for the given C_0 and β values (Alcock et al. 1996:e.g.). We find that the slope of the function $f_{t_{\rm E}}$ for planets with $-4.5 < \log q < -3$ is flat, $\beta = 0.13^{+0.34}_{-0.31}$, but the slope for planets with $-3 < \log q < -1.5$ has a positive correlation with $\log t_{\rm E}$, $\beta = 0.80 \pm 0.46$. Although the estimation is rough, the positive correlation is seen only for giant planets.

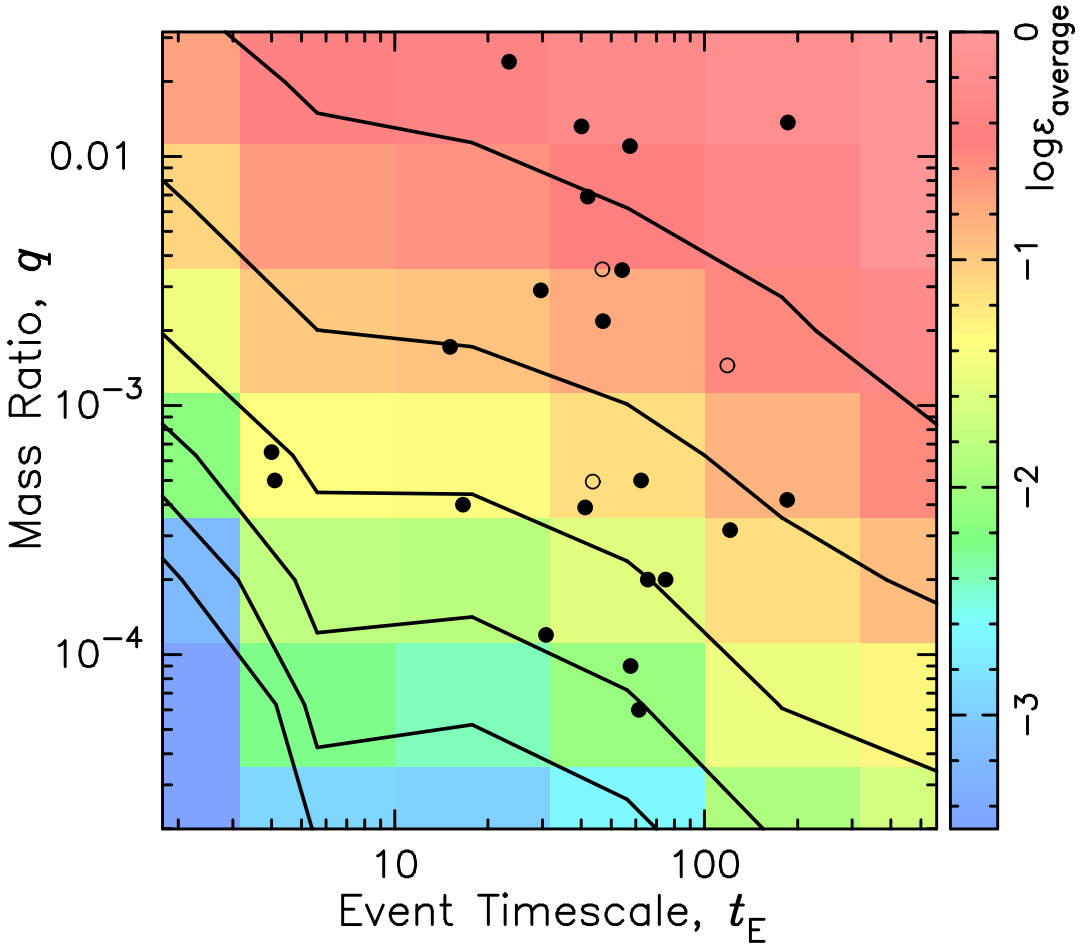

Figure 5.19: Detection efficiencies in different mass ratios as a function of $t_{\rm E}$. The filled circles show the locations of 21 planets listed in Table 5.1. The open circles show the locations of 3 planet candidates listed in Table 5.2. The color map indicates the logarithmic detection efficiencies. The black lines indicate the average detection efficiencies of $\log\varepsilon(\log t_{\rm E}, \log q) = -0.5$, -1.0, -1.5, -2.0, -2.5, and -3.0, from the top right to the bottom left.

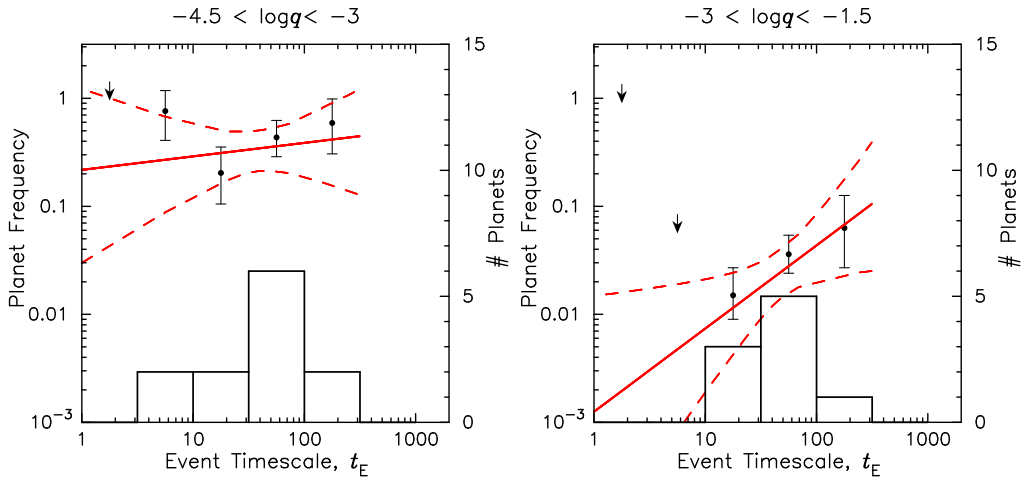

Figure 5.20: Planet frequency as a function of the $t_{\rm E}$. Left: for planets with $-4.5 < \log < -3$. The histogram shows the $t_{\rm E}$ distribution for the planetary events with right-hand scale. The plots with error bars are planet frequency corrected by the detection efficiencies in each $\log t_{\rm E}$ bin. The red solid line shows the power law fit to the plots and dashed lines show the 68 % confidence interval. Right: same as the left panel, but for planets with $-3 < \log < -1.5$. The arrows are upper limits with 95 % confidence level.

As discussed in Gould et al. (2010b), the lens stars in the longer timescale events favor nearby disk stars over bulge stars, or favor massive host stars. Thus, the higher planet frequencies in the longer timescale events indicate that planetary systems favor nearby disk stars over bulge stars, or favor massive host stars. If the giant planet frequency is flat with the distance to the lens star, the giant planet frequency could depend on the lens star mass, $f \propto t_{\rm E}^{0.80} \propto (M_{\rm L}^{0.5})^{0.80} \propto M_L^{0.40\pm0.23}$, since $t_{\rm E}$ is proportional to square root of the lens star mass (See Equation 2.14). Johnson et al. (2010b) studied the planet occurrence correlation with the host star mass and metallicity. Their function is $f(M, F) = CM^{(1.0\pm0.3)}10^{(1.2\pm0.2)F}$, where M is the host star mass and $F \equiv$ [Fe/H]. Our rough estimate is about 2σ lower than their value, which were estimated from their sample stars with a mass range from M-dwarf to A-type star. The host star masses are unknown in our sample, but most of them could be late type stars, such as M- and K-dwarfs, and very few of them could be A-type stars. This difference in the host star mass range could affect the slope of the giant planet frequency as a function of the host star mass. Montet et al. (2013) estimates the correlation of the planet frequency with the host star mass by using only M-dwarf star sample. They finds no positive correlation with the host star mass in their M-dwarf sample.

To understand the dependence of giant planet frequency on the late type host star mass, much larger sample is required. Unfortunately, the host star mass in

normal microlensing events is unknown. If the event timescale depends on only lens star mass ($t_{\rm E} \propto \sqrt{M}$), we can assume the longer timescale events have massive lens stars. But actually, the distance to the lens and transverse velocity are also degenerate in $t_{\rm E}$. Thus, longer timescale events could be contaminated by lens stars with small masses, and vice versa. Nevertheless, the slope of the event timescale function for giant planets has positive value, which are estimated after the correction by detection efficiency. Large sample of the events with determination of lens star masses will reveal the correlation.

5.8 Uncertainty in the Selection Criteria

Our result is based on the 21 planet detections that are selected by the event selection criteria (Cut-1– Cut-5), the detection criteria ($\Delta\chi^2_{\rm S-P}$) and the binary-planetary criteria ($\Delta\chi^2_{\rm B-P}$) in Section 5.1.3. The event selection criteria are not relevant to the existence of planets. The detection criteria, $\Delta\chi^2_{\rm S-P} > 100$, beyond which the light curve is recognized as anomaly, affects the number of included planets. More conservative (lower) criteria decrease (increase) the number of planets and detection efficiencies. The lower (higher) detection efficiencies lead to higher (lower) planet frequency, and the smaller (larger) number of included planets leads to lower (higher) planet frequency. Thus, the change of the detection criteria should not change the planet frequency. We use another criteria, the binary-planetary criteria to classify the planetary events with $q < 0.03$ from stellar binary events with $q > 0.03$. $\Delta\chi^2_{\rm B-P} > 25$ are used for the binary-planetary criteria in the selection. To verify this criteria, we need a simulation where we investigate how high criteria we should use to determine that the model fitting to a given artificial planetary or binary light curves can find out the true mass ratios. This simulation takes computation time. To skip this, we set a secure criterion of $\Delta\chi^2_{\rm B-P} > 25$. Despite a less conservative criterion, the events selected with $25 > \Delta\chi^2_{\rm B-P} > 4$ could be also planetary events.

Here, we estimate the planet abundance using the different criteria to check the validity of the criteria for the planet selection. We use 4 or 25 for $\Delta\chi^2_{\rm B-P}$ and 100 or 200 for $\Delta\chi^2_{\rm S-P}$. Estimated values for the planet abundance are listed in Table 5.4. The values with any combination of the different criteria are consistent with the results in Section 5.6, which are estimated by using $\Delta\chi^2_{\rm B-P} > 25$ and $\Delta\chi^2_{\rm S-P} > 100$. Thus, our results do not depends on the selection criteria for the planetary events.

Table 5.4: Planet Abundance with Different Selection Criteria

Criteria	$0.3 - 10\,M_{\rm Jup}$	$10 - 30\,M_{\oplus}$	$5\,M_{\oplus} - 10\,M_{\rm Jup}$
$\Delta\chi^2_{\rm B-P} > 25$, $\Delta\chi^2_{\rm S-P} > 100$	$0.15^{+0.04}_{-0.03}$	$0.52^{+0.18}_{-0.15}$	$1.6^{+0.52}_{-0.42}$
$\Delta\chi^2_{\rm B-P} > 25$, $\Delta\chi^2_{\rm S-P} > 200$	$0.16^{+0.05}_{-0.04}$	$0.54^{+0.22}_{-0.17}$	$1.6^{+0.65}_{-0.49}$
$\Delta\chi^2_{\rm B-P} > 4$, $\Delta\chi^2_{\rm S-P} > 100$	$0.17^{+0.04}_{-0.04}$	$0.56^{+0.19}_{-0.15}$	$1.7^{+0.54}_{-0.44}$
$\Delta\chi^2_{\rm B-P} > 4$, $\Delta\chi^2_{\rm S-P} > 200$	$0.18^{+0.05}_{-0.04}$	$0.56^{+0.22}_{-0.17}$	$1.7^{+0.65}_{-0.50}$

5.9 Discussion

Our result in Section 5.6 indicates that cool Neptunes are factor 3.5 more common than gas giants within $0.5 - 10$ AU where microlensing method is sensitive to planets. This is consistent with the previous microlensing studies (Gould et al. 2010b, Sumi et al. 2010, Cassan et al. 2012). We found that M or K-type dwarfs, which are the majority of the host stars in our sample, have on average 1.6 planets beyond the snow line. This is also consistent with Cassan et al. (2012). Moreover, the estimated frequencies of gas giant planets agree with the RV results for long orbital period planets around M-dwarfs by Bonfils et al. (2013) and Montet et al. (2013), who combined the RV results with the constraints from direct imaging. These results indicate that the planet frequency beyond the snow line is higher than that of close-in planets, and the frequency of Neptune-like planets is higher than that of Jupiter-like planets. This is consistent with the result of Cumming et al. (2008), $dN = Cm_{\rm P}^{-0.31\pm0.20}P^{0.26\pm0.1}d\ln m_{\rm P}\,d\ln P$. But, our slope for the planet mass (see Equation 5.15) is steeper than Cumming's one. This seems to indicate that the small planets are much more common beyond the snow line. This basically agrees with the planet population synthesis simulation based on core accretion model (Ida & Lin 2004a, Mordasini et al. 2009).

However, we should note that our estimate of planetary mass function is depending on the prior that assumes the uniform probability of stars being orbited by a certain mass ratio planet. Actually, the number of detected planets by microlensing are increasing, but the mass measurements in the most of them are depending on the assumed prior. This is because the lens mass, distance to the lens, and transverse velocity are degenerate in event timescale $t_{\rm E}$, so the mass of lens star and planet are estimated by the Bayesian analysis with the prior except for the special case, where the lens mass can be directly derived with the detection of both the finite source and parallax effects. Microlensing has found 10 planetary systems where gas giant planets orbit around late type stars (Bennett et al. 2006, Dong et al. 2009a, Bennett et al. 2010, Dong et al. 2009b, Suzuki et al. 2014,

Batista et al. 2009, Bachelet et al. 2012, Yee et al. 2012, Kains et al. 2013, Tsapras et al. 2013).

In the 6 planetary systems of them, the masses of the systems are estimated by the Bayesian analysis with the prior. One of them, MOA-2011-BLG-293, whose primary star mass was estimated as $M_{\rm L} = 0.59^{+0.35}_{-0.29}\ M_\odot$ at first (Yee et al. 2012, Batista et al. 2014), was observed by using Keck AO, and the mass of the primary star was identified as $M_{\rm L} = 0.86 \pm 0.06\ M_\odot$ (Batista et al. 2014). Thus, to confirm the primary star and planet mass, such follow-up observations with a high-resolution imaging should be conducted for the planetary events whose mass measurements are depending on the prior assumption.

The masses of the other 4 systems are derived without the prior, and one of them is a system with two gas giants orbiting an M-dwarf. The formation of these planets should be explained theoretically. The population synthesis based on the core accretion model predicts the formation of giant planets around M-dwarfs (Ida & Lin 2005), but they expect that gas giants around late type stars are rare compare to the gas giants around massive stars. Laughlin et al. (2004) also expects only a few gas giant planets around M-dwarfs. Kennedy & Kenyon (2008) estimates the occurrence of gas giant planets is 1% around M-dwarfs. A precise mechanism for the formation of gas giant planets around low mass stars is still an open question. Statistical studies by using only planets with secure mass measurements will allow the complete comparison of the observational results with the population synthesis simulation, and tell us the real abundance of planets beyond the snow line.

In Section 5.3, we derived the mass ratio function, $dN/d\log\!s\, d\log\!q = 0.09 \pm 0.02(q/q_0)^{-0.69\pm0.12}$. The mass ratio can be derived by the light curve model fitting without the prior probabilities, so this could be more secure than the planetary mass function. With use of the planetary mass ratio function, we derive the planet abundance N_q: the averaged number of planet per star in a mass ratio and separation domain. Following Section 5.6, we integrate the mass ratio function, Equation (5.3) in the mass ratio and separation domain, where the separation domain is $0.3 < s < 3$. The results of the integration are listed in Table 5.5. The averaged number of planets per star for planets with $10^{-5} < q < 10^{-2}$, $N_q = 1.3^{+0.70}_{-0.48}$ is consistent with the result of $N = 1.6^{+0.52}_{-0.42}$ in Section 5.6. But, the abundance for planets with $10^{-3} < q < 10^{-2}$ and $10^{-2} < q < 10^{-3}$, which roughly correspond to gas giants and Neptune-like planets, respectively, are about factor 3 lower than the abundance for planets with $0.3 < m_{\rm P}/M_{\rm Jup} < 10$ and $10 < m_{\rm P}/M_\oplus < 30$. This is partly because the integration domain for log$s$ is factor 1.3 narrower than log$a$. The remaining difference is explained by the difference between the mass ratio function and planetary mass function. Nevertheless, the conclusions of this paper do not change. The values in Table 5.5 are consistent

Table 5.5: Planet Abundance with mass ratio domain

Mass Ratio	N_q (per star)
$10^{-3} < q < 10^{-2}$	$0.045^{+0.011}_{-0.010}$
$10^{-4} < q < 10^{-3}$	$0.22^{+0.07}_{-0.06}$
$10^{-5} < q < 10^{-4}$	$1.0^{+0.64}_{-0.42}$
$10^{-5} < q < 10^{-2}$	$1.3^{+0.70}_{-0.48}$

with the RV results for planets with long orbital period (Bonfils et al. 2013, Montet et al. 2013). Also, our values are higher than the RV results for close-in planets (Cumming et al. 2008, Howard et al. 2010, Mayor et al. 2009, Johnson et al. 2010a).

The power law mass ratio function seems to agree with the planet distribution corrected by the detection efficiencies (see Figure 5.10). There seems to be no "planet desert", which is a deficit of planets with dozens of $M_\oplus$ expected to be located inner than the snow line (Ida & Lin 2004a). Since our survey is sensitive to planets beyond the snow line, the feature of no planet desert agrees with the population synthesis by Ida & Lin (2004a). But we should note that the mass of the primary stars ranges from M-dwarf to G-dwarf. Thus, the specific structures in the mass ratio distribution could be smoothed over, even if they exist. Also, the frequency of planet with $q \sim 10^{-5}$ is hardly constrained due to the very low detection sensitivity to such small planets. To clarify these problem, we should observe much more microlensing events. Statistical studies by using the planets with mass measurements will reveal the specific structure of mass ratio function toward the smaller mass ratio.

Chapter 6

Conclusion

We report the discovery and analysis of a planetary microlensing event MOA-2008-BLG-379. As is often the case with high magnification microlensing events, there are two degenerate models: a close model with a planet-host separation of $s = 0.903$ and a wide model with $s = 1.119$. Both have a mass ratio of $q \simeq 7 \times 10^{-3}$. Our Bayesian analysis indicates that the lens system consists of a G, K, or M-dwarf orbited by super-Jupiter mass planet. The most likely physical properties for the lens system, according to the Bayesian analysis, are that the host is a late K-dwarf, and the planet has a mass of about 4 Jupiter masses with a projected separation of about 3 AU. However, these values are dependent on our prior assumption that stars of different masses have equal probabilities to host a planet of the observed mass ratio and separation.

We also report the planet abundance N, which is the average number of planets per star estimated from the planet mass function, from the statistical analysis of the archival MOA-II data in 2007–2012. We calculate the detection efficiency in 1492 microlensing events including 21 planet detections. We find that $N = 0.15^{+0.04}_{-0.03}$ for Jupiter-like planets ($0.3 - 10\ M_{\rm Jup}$), and $N = 0.52^{+0.18}_{-0.15}$ for Neptune-like planets ($10 - 30\ M_{\oplus}$) within $0.5 < a < 10$ AU. For the planets with mass from 5 $M_{\oplus}$ to 10 $M_{\rm Jup}$, we find $N = 1.6^{+0.52}_{-0.42}$ within $0.5 < a < 10$ AU. Our result is consistent with the previous microlensing results (Sumi et al. 2010, Gould et al. 2010b, Cassan et al. 2012) and the RV results for planets with long orbital period (Bonfils et al. 2013, Montet et al. 2013). By contrast, the planet occurrence for close-in planets probed by RV shows lower values (Cumming et al. 2008, Howard et al. 2010, Mayor et al. 2009, Johnson et al. 2010a). This is consistent with the positive correlation of planet occurrence with orbital period found by Cumming et al. (2008). These results are based on the estimated planet mass function $F = 10^{-0.67\pm0.10}(m_{\rm P}/m_0)^{-0.78\pm0.12}$, which depends on the prior of the uniform probability of host stars harboring a planet. This uniform prior, however, does not affect our conclusion. Although the planet abundance N_q, which is the average

number of planets par star estimated from the mass ratio function in Section 5.9, is estimated lower without the prior, the above conclusion dose not change.

We demonstrate that larger number of planets exist beyond the snow line compared to the close-in planets. But, we should know the lens star mass without any assumption for the complete comparison of microlensing results with theoretical simulations. To achieve this, large number of planet detections and statistical studies by using the planets with mass measurement are required. In March 2010, OGLE collaboration started their new survey observation phase OGLE-IV with their new 1.4 deg^2 CCD camera, and this has been yielding twice as much planetary microlensing events as before in cooperation with MOA-II. Moreover, the Korean Microlensing Telescope Network (KMTNet) is constructing three new wide FOV microlensing survey telescope in Chile, South Africa, and Australia (Kim et al. 2010). These large survey telescopes located at distant longitude will allow us to monitor the microlensing light curve round-the-clock and produce much more planetary microlensing events found with survey data alone. Also, the capabilities of microlensing follow-up teams are also rapidly improving, most notably with the recent expansion (Brown et al. 2013) of the Las Cumbres Observatory Global Telescope Network (LCOGT), which should result in much higher light curve sampling rates of planetary signals discovered in progress.

Acknowledgement

I would like to express my great gratitude to my supervisor Prof. H. Shibai for giving me the opportunity of studying this work, and providing strong support for this ph.D. thesis.

I would express my sincere thanks to Prof. T. Sumi and Prof. M. Fukagawa for reviewing my thesis carefully and providing a lot of valuable advice. I would also like to extend my gratitude to Prof. Y. Muraki, Prof. F. Abe for supporting me in many ways.

I would like to thank all the members of the MOA collaboration for supporting this work. I would like to express my special thanks to Prof. D. P. Bennett for giving me a lot of advice. I would like to thank P. J. Tristram for giving me technical advice for observations and sharing fulfilling time at Mt. John. I would like to express my great appreciation to A. C. Gilmore and P. M. Kilmartin for everything they have done for me during my stay at Mt. John. I am really thankful to all the master and doctoral students of MOA, especially A. Fukui, N. Miyake, K. Furusawa, K. Wada, S. Kobara, K. Ohmori, K. Suzuki, S. Takino, N. Tsurumi, N. Yamai, N. Koshimoto, and S. Namba, for sharing fulfilling days through observations and discussion. I would also like to thank Prof. P. C. M. Yock for supporting the publication of my paper.

Finally, I am grateful to all the members of the Infrared Astronomy Laboratory of Osaka University for giving me comfortable environment and a lot of fun.

Bibliography

Alard, C. & Lupton, R.H. 1998, ApJ, 503, 325

Albrecht, S., Winn, J. N., Johnson, J. A., et al. 2012, ApJ, 757, 18

Alcock, C., Allsman, R. A., Axelrod, T. S., et al. 1993a, Sky Surveys. Protostars to Protogalaxies, 43, 291

Alcock, C., Akerlof, C. W., Allsman, R. A., et al. 1993b, Natur, 365, 621

Alcock, C., Allsman, R. A., Alves, D., et al. 1995, ApJL, 454, L125

Alcock, C., Allsman, R. A., Axelrod, T. S., et al. 1996, ApJ, 461, 84

Aubourg, E., Bareyre, P., Brehin, S., et al. 1993, The Messenger, 72, 20

Batista, V., Beaulieu, J.-P., Gould, A., et al. 2014, ApJ, 780, 54

Batista, V., Dong, S., Gould, A., et al. 2009, A&A, 508, 467

Bachelet, E., Shin, I.-G., Han, C., et al. 2012, ApJ, 754, 73

Beaulieu, J.-P., Bennett, D. P., Fouqué, P., et al. 2006, Natur, 439, 437

Bennett, D.P, 2008, in Exoplanets, ed. J. Mason (Berlin: Springer), 47

Bennett, D. P. 2010, ApJ, 716, 1408

Bennett, D. P., Batista, V., Bond, I. A., et al. 2013, arXiv:1312.3951

Bennett, D. P., Anderson, J., Bond, I. A., Udalski, A., & Gould, A. 2006, ApJL, 647, L171

Bennett, D. P., Anderson, J., & Gaudi, B.S. 2007, ApJ, 660, 781

Bennett, D. P., Bond, I. A., Udalski, A., et al. 2008, ApJ, 684, 663

Bennett, D. P. & Rhie, S.H. 1996, ApJ, 472, 660

Bennett, D. P., & Rhie, S. H. 2002, ApJ, 574, 985

Bennett, D. P., Rhie, S. H., Nikolaev, S., et al. 2010, ApJ, 713, 837

Bennett, D. P., Sumi, T., Bond, I. A., et al. 2012, ApJ, 757, 119

Bensby, T., Adén, D., Meléndez, J., et al. 2011, A&A, 533, A134

Bessell, M. S., & Brett, J. M. 1988, PASP, 100, 1134

Bond, I. A., Abe, F., Dodd, R. J., et al. 2001, MNRAS, 327, 868

Bond, I. A., Udalski, A., Jaroszyński, M., et al. 2004, ApJL, 606, L155

Bonfils, X., Delfosse, X., Udry, S., et al. 2013, A&A, 549, A109

Borucki, W. J., Koch, D. G., Basri, G., et al. 2011, ApJ, 736, 19

Brown, T. M., Baliber, N., Bianco, F. B., et al. 2013, PASP, 125, 1031

Butler, R. P., Wright, J. T., Marcy, G. W., et al. 2006, ApJ, 646, 505

Cassan, A. 2008, A&A, 491, 587

Cassan, A., Kubas, D., Beaulieu, J.-P., et al. 2012, Natur, 481, 167

Choi, J.-Y., Shin, I.-G., Park, S.-Y., et al. 2012, ApJ, 751, 41

Chung, S.-J., Han, C., Park, B.-G., et al. 2005, ApJ, 630, 535

Chwolson, O. 1924, Astronomische Nachrichten, 221, 329

Claret, A. 2000, A&A, 363, 1081

Cumming, A., Butler, R. P., Marcy, G. W., et al. 2008, PASP, 120, 531

Dominik, M. 2006, MNRAS, 367, 669

Dong, S., Gould, A., Udalski, A., et al. 2009a, ApJ, 695, 970

Dong, S., Bond, I. A., Gould, A., et al. 2009b, ApJ, 698, 1826

Dong, S., DePoy, D. L., Gaudi, B. S., et al. 2006, ApJ, 642, 842

Doyle, L. R., Carter, J. A., Fabrycky, D. C., et al. 2011, Sci, 333, 1602

Eddington, A. S. 1920, Cambridge Science Classics, Cambridge: University Press, 1920,

Einstein, A. 1936, Sci, 84, 506

Fukui, A., Narita, N., Kurosaki, K., et al. 2013, ApJ, 770, 95

Furusawa, K., Udalski, A., Sumi, T., et al. 2013, ApJ, 779, 91

Gaudi, B. S. 2012, ARA&A, 50, 411

Gaudi, B. S., Albrow, M. D., An, J., et al. 2002, ApJ, 566, 463

Gaudi, B. S., Bennett, D. P., Udalski, Al, et al. 2008, Sci, 319, 927

Girardi, L., Bertelli, G., Bressan, A., et al. 2002, A&A, 391, 195

Gould, A. 2000, ApJ, 542, 785

Gould, A., Dong, S., Bennett, D. P., et al. 2010a, ApJ, 710, 1800

Gould, A., Dong, S., Gaudi, B. S., et al. 2010b, ApJ, 720, 1073

Gould, A., & Loeb, A. 1992, ApJ, 396, 104

Gould, A., Udalski, A., Monard, B., et al. 2009, ApJL, 698, L147

Green, J., Schechter, P., Baltay, C., et al. 2012, arXiv:1208.4012

Griest, K., Alcock, C., Axelrod, T. S., et al. 1991, ApJL, 372, L79

Han, C. 2006, ApJ, 638, 1080

Han, C., & Gould, A. 1995, ApJ, 449, 521

Han, C., & Gould, A. 2003, ApJ, 592, 172

Holtzman, J. A., Watson, A. M., Baum, W. A., et al. 1998, AJ, 115, 1946

Howard, A. W. 2013, Sci, 340, 572

Howard, A. W., Marcy, G. W., Johnson, J. A., et al. 2010, Sci, 330, 653

Howard, A. W., Marcy, G. W., Bryson, S. T., et al. 2012, ApJS, 201, 15

Ida, S., & Lin, D. N. C. 2004a, ApJ, 604, 388

Ida, S., & Lin, D. N. C. 2004b, ApJ, 616, 567

Ida, S., & Lin, D. N. C. 2005, ApJ, 626, 1045

Janczak, J., Fukui, A., Dong, S., et al. 2010, ApJ, 711, 731

Jaroszyński, M. Skowron, J., Udalski, A., et al. 2010, AcA, 60, 197

Johnson, J. A., Aller, K. M., Howard, A. W., & Crepp, J. R. 2010b, PASP, 122, 905

Johnson, J. A., Howard, A. W., Marcy, G. W., et al. 2010a, PASP, 122, 149

Kains, N., Street, R. A., Choi, J.-Y., et al. 2013, A&A, 552, A70

Kasting, J. F., Whitmire, D. P., & Reynolds, R. T. 1993, Icarus, 101, 108

Kennedy, G. M., & Kenyon, S. J. 2008, ApJ, 673, 502

Kennedy, G. M., Kenyon, S. J., & Bromley, B. C. 2006, ApJL, 650, L139

Kervella, P., & Fouqué, P. 2008, A&A, 491, 855

Kervella, P., Thévenin, F., Di Folco, E., & Ségransan, D. 2004, A&A, 426, 297

Kerins, E., Robin, A. C., & Marshall, D. J. 2009, MNRAS, 396, 1202

Kim, S.-L., Park, B.-G., Lee, C.-U., et al. 2010, Proc. SPIE, 7733, 77733F

Kiraga, M., & Paczyński , B. 1994, ApJL, 430, L101

Kubas, D., Beaulieu, J. P., Bennett, D. P., et al. 2012, A&A, 540, A78

Laughlin, G., Bodenheimer, P., & Adams, F. C. 2004, ApJL, 612, L73

Lecar, M., Podolak, M., Sasselov, D., & Chiang, E. 2006, ApJ, 640, 1115

Liebes, S. 1964, Physical Review, 133, 835

Lissauer, J. J., Fabrycky, D. C., Ford, E. B., et al. 2011, Natur, 470, 53

Lissauer, J. J. 1993, ARA&A, 31, 129

Lodge, O. J. 1919, Natur, 104, 354

Mao, S., & Paczyński , B. 1991, ApJL, 374, L37

Marois, C., Macintosh, B., Barman, T., et al. 2008, Sci, 322, 1348

Mayor, M., Marmier, M., Lovis, C., et al. 2011, arXiv:1109.2497

Mayor, M., Udry, S., Lovis, C., et al. 2009, A&A, 493, 639

Mayor, M., & Queloz, D. 1995, Natur, 378, 355

Miyake, N., Sumi, T., Dong, S., et al. 2011, ApJ, 728, 120

Montet, B. T., Crepp, J. R., Johnson, J. A., Howard, A. W., & Marcy, G. W. 2013, arXiv:1307.5849

Mordasini, C., Alibert, Y., & Benz, W. 2009, A&A, 501, 1139

Muraki, Y., Sumi, T., Abe, F., et al. 1999, Progress of Theoretical Physics Supplement, 133, 233

Muraki, Y., Han, C., Bennett, D. P., et al. 2011, ApJ, 741, 22

Narita, N., Fukui, A., Ikoma, M., et al. 2013, ApJ, 773, 144

Nataf, D. M., Gould, A., Fouqué, P. et al. 2013, ApJ, 769, 88

Paczyński , B. 1986a, ApJ, 301, 503

Paczyński , B. 1986b, ApJ, 304, 1

Paczyński , B. 1991, ApJL 371, L63

Pollack, J. B., Hubickyj, O., Bodenheimer, P., et al. 1996, Icarus, 124, 62

Popowski, P., Griest, K., Thomas, C. L., et al. 2005, ApJ, 631, 879

Rameau, J., Chauvin, G., Lagrange, A.-M., et al. 2013, A&A, 553, A60

Rattenbury, N. J., Mao, S., Sumi, T., & Smith, M. C. 2007, MNRS, 378, 1064

Refsdal, S. 1964, MNRAS, 128, 295

Renn, J., Sauer, T., & Stachel, J. 1997, Sci, 275, 184

Rhie, S. H. 1997, ApJ, 484, 63

Rhie, S. H., Bennett, D. P., Becker, A. C., et al. 2000, ApJ, 533, 378

Sako, T., Sekiguchi, T., Sasaki, M., et al. 2008, ExA, 22, 51

Schechter, P. L., Mateo, M., & Saha, A. 1993, PASP, 105, 1342

Shvartzvald, Y. & Maoz, D. 2012, MNRAS, 419, 3631

Shvartzvald, Y., Maoz, D., Kaspi, S., et al. 2013, arXiv:1310.0008

Shin, I.-G., Sumi, T., Udalski, A., et al. 2013, ApJ, 764, 64

Stamatellos, D., & Whitworth, A. P. 2009, MNRAS, 392, 413

Sumi, T., Abe, F., Bond, I. A., et al. 2003, ApJ, 591, 204

Sumi, T., Bennett, D. P., Bond, I. A., et al. 2010, ApJ, 710, 1641

Sumi, T., Kamiya, K., Bennett, D. P., et al. 2011, Natur, 473, 349

Sumi, T., Bennett, D. P., Bond, I. A., et al. 2013, ApJ, 778, 150

Sumi, T., Woźniak, P. R., Udalski, A., et al. 2006, ApJ, 636, 240

Suzuki, D., Udalski, A., Sumi, T., et al. 2014, ApJ, 780, 123

Szymański, M. K., Udalski, A., Soszyński, I., et al. 2011, AcA, 61, 83

Tomaney, A. B. & Crotts, A. P. S. 1996, AJ, 112, 2872

Tsapras, Y., Choi, J.-Y., Street, R. A., et al. 2013, arXiv:1310.2428

Udalski, A. 2003, AcA, 53, 291

Udalski, A., Szymanski, M., Kaluzny, J., et al. 1992, AcA, 42, 253

Udalski, A., Szymanski, M., Kaluzny, J., et al. 1993, AcA, 43, 289

Udalski, A., Szymański, M., Kałużny, J., et al. 1994, AcA., 44, 227

Verde, L., Peiris, H. V., & Spergel, D. N., 2003, ApJS, 148, 195

Witt, H. J. 1990, A&A, 236, 311

Wood, A., & Mao, S. 2005, MNRAS, 362, 945

Yee, J. C., Udalski, A., Sumi, T., et al. 2009, ApJ, 703, 2082

Yee, J. C., Hung, L.-W., Bond, I. A., et al. 2013, ApJ, 769, 77

Yee, J. C., Shvartzvald, Y., Gal-Yam, A., et al. 2012, ApJ, 755, 102

Appendix A

List of Publications

1. "Planet Frequency beyond the Snow Line from MOA-II Microlensing Survey in 2007 – 2012"
   Suzuki, D., Sumi, T., Bennett, D. P., Bond, I. A., Abe, F., Botzler, C. S., Freeman, M., Fukagawa, M., Fukui, A., Fukunaga, D., Furusawa, K., Itow, Y., Koshimoto, N., Ling, C. H., Masuda, K., Matsubara, Y., Muraki, Y., Namba, S., Ohnishi, K., Rattenbury, N., Saito, To., Shibai, H., Sullivan, D. J., Sweatman, W. L., Tristram, P. J., Tsurumi, N., Wada, K., Yock, P. C. M., Yonehara, A., The MOA Collaboration
   To be submitted

2. "MOA-2008-BLG-379Lb: A Massive Planet from a High Magnification Event with a Faint Source"
   Suzuki, D., Udalski, A., Sumi, T., Bennett, D. P., Bond, I. A., Abe, F., Botzler, C. S., Freeman, M., Fukagawa, M., Fukui, A., Furusawa, K., Itow, Y., Ling, C. H., Masuda, K., Matsubara, Y., Muraki, Y., Ohnishi, K., Rattenbury, N., Saito, To., Shibai, H., Sullivan, D. J., Suzuki, K., Sweatman, W. L., Takino, S., Tristram, P. J., Wada, K., Yock, P. C. M., The MOA Collaboration, Szymański, M. K., Kubiak, M., Soszyński, I., Pietrzyński, G., Poleski, R., Ulaczyk, K., Wyrzykowski, Ł., The OGLE Collaboration
   The Astrophysical Journal, 780, 123 (2014)

3. "A Sub-Earth-Mass Moon Orbiting a Gas Giant Primary or a High Velocity Planetary System in the Galactic Bulge"
   Bennett, D. P., Batista, V., Bond, I. A., Bennett, C. S., **Suzuki, D.**, Beaulieu, J.-P., Udalski, A., Donatowicz, J., Abe, F., Botzler, C. S., Freeman, M., Fukunaga, D., Fukui, A., Itow, Y., Koshimoto, N., Ling, C. H., Masuda, K., Matsubara, Y., Muraki, Y., Namba, S., Ohnishi, K., Rattenbury, N. J., Saito, To., Sullivan, D. J., Sumi, T., Sweatman, W. L., Tristram, P. J., Tsurumi, N., Wada, K., Yock, P. C. M., The MOA collaboration, Albrow, M. D., Bachelet, E., Brillant, S., Caldwell, J. A. R., Cassan, A., Cole, A. A., Corrales, E., Coutures, C., Dieters, S., Dominis Prester, D., Fouqué, P., Greenhill, J., Horne, K., Koo, J.-R., Kubas, D., Marquette, J.-B., Martin, R., Menzies, J. W., Sahu, K. C., Wambsganss, J., Williams, A., Zub, M., The PLANET Collaboration, Choi, J. Y., DePoy, D. L., Dong, Subo, Gaudi, B. S., Gould, A., Han, C., Henderson, C. B., McGregor, D., Lee, C.-U., Pogge, R. W., Shin, I.-G., Yee, J. C., The μFUN Collaboration, Szymański, M. K., Skowron, J., Poleski, R., Kozłowski, S., Wyrzykowski, Ł., Kubiak, M., Pietrukowicz, P.,

Pietrzyński, G., Soszyński, I., Ulaczyk, K., The OGLE Collaboration, Tsapras, Y., Street, R. A., Dominik, M., Bramich, D. M., Browne, P., Hundertmark, M., Kains, N., Snodgrass, C., Steele, I. A., The RoboNet Collaboration, Dekany, I., Gonzalez, O. A., Heyrovský, D., Kandori, R., Kerins, E., Lucas, P. W., Minniti, D., Nagayama, T., Rejkuba, M., Robin, A. C., Saito, R.
eprint arXiv:1312.3951

4. "MOA-2010-BLG-328Lb: A Sub-Neptune Orbiting very Late M Dwarf?"
Furusawa, K., Udalski, A., Sumi, T., Bennett, D. P., Bond, I. A., Gould, A., Jørgensen, U. G., Snodgrass, C., Dominis Prester, D., Albrow, M. D., Abe, F., Botzler, C. S., Chote, P., Freeman, M., Fukui, A., Harris, P., Itow, Y., Ling, C. H., Masuda, K., Matsubara, Y., Miyake, N., Muraki, Y., Ohnishi, K., Rattenbury, N. J., Saito, To., Sullivan, D. J., **Suzuki, D.**, Sweatman, W. L., Tristram, P. J., Wada, K., Yock, P. C. M., The MOA Collaboration, Szymański, M. K., Soszyński, I., Kubiak, M., Poleski, R., Ulaczyk, K., Pietrzyński, G., Wyrzykowski, Ł., The OGLE Collaboration, Choi, J.-Y., Christie, G. W., DePoy, D. L., Dong, Subo, Drummond, J., Gaudi, B. S., Han, C., Hung, L.-W., Hwang, K.-H., Lee, C.-U., McCormick, J., Moorhouse, D., Natusch, T., Nola, M., Ofek, E., Pogge, R. W., Shin, I.-G., Skowron, J., Thornley, G., Yee, J. C., The μFUN Collaboration, Alsubai, K. A., Bozza, V., Browne, P., Burgdorf, M. J., Calchi Novati, S., Dodds, P., Dominik, M., Finet, F., Gerner, T., Hardis, S., Harpsøe, K., Hinse, T. C., Hundertmark, M., Kains, N., Kerins, E., Liebig, C., Mancini, L., Mathiasen, M., Penny, M. T., Proft, S., Rahvar, S., Ricci, D., Scarpetta, G., Schäfer, S., Schönebeck, F., Southworth, J., Surdej, J., Wambsganss, J., The MiNDSTEp Consortium, Street, R. A., Bramich, D. M., Steele, I. A., Tsapras, Y., The RoboNet Collaboration, Horne, K., Donatowicz, J., Sahu, K. C., Bachelet, E., Batista, V., Beatty, T. G., Beaulieu, J.-P., Bennett, C. S., Black, C., Bowens-Rubin, R., Brillant, S., Caldwell, J. A. R., Cassan, A., Cole, A. A., Corrales, E., Coutures, C., Dieters, S., Fouqué, P., Greenhill, J., Henderson, C. B., Kubas, D., Marquette, J.-B., Martin, R., Menzies, J. W., Shappee, B., Williams, A., Wouters, D., van Saders, J., Zellem, R., Zub, M., The PLANET Collaboration
The Astrophysical Journal, 779, 91 (2013)

5. "The Microlensing Event Rate and Optical Depth toward the Galactic Bulge from MOA-II"
Sumi, T., Bennett, D. P., Bond, I. A., Abe, F., Botzler, C. S., Fukui, A., Furusawa, K., Itow, Y., Ling, C. H., Masuda, K., Matsubara, Y., Muraki, Y., Ohnishi, K., Rattenbury, N., Saito, To., Sullivan, D. J., **Suzuki, D.**, Sweatman, W. L., Tristram, P. J., Wada, K., Yock, P. C. M., The MOA Collaboratoin
The Astrophysical Journal, 778, 150 (2013)

6. "Interpretation of a Short-term Anomaly in the Gravitational Microlensing Event MOA-2012-BLG-486"
Hwang, K.-H., Choi, J.-Y., Bond, I. A., Sumi, T., Han, C., Gaudi, B. S., Gould, A., Bozza, V., Beaulieu, J.-P., Tsapras, Y., Abe, F., Bennett, D. P., Botzler, C. S., Chote, P., Freeman, M., Fukui, A., Fukunaga, D., Harris, P., Itow, Y., Koshimoto, N., Ling, C. H., Masuda, K., Matsubara, Y., Muraki, Y., Namba, S., Ohnishi, K., Rattenbury, N. J., Saito, To., Sullivan, D. J., Sweatman, W. L., **Suzuki, D.**, Tristram, P. J., Wada, K., Yamai, N., Yock, P. C. M., Yonehara, A., The MOA Collaboration, de Almeida, L. Andrade, DePoy, D. L., Dong, Subo, Jablonski, F., Jung, Y. K., Kavka, A., Lee, C.-U., Park, H., Pogge, R. W., Shin, I.-G., Yee, J. C., The μFUN Collaboration, Albrow, M. D., Bachelet, E., Batista, V., Brillant, S.,

Caldwell, J. A. R., Cassan, A., Cole, A., Corrales, E., Coutures, Ch., Dieters, S., Dominis Prester, D., Donatowicz, J., Fouqué, P., Greenhill, J., Jørgensen, U. G., Kane, S. R., Kubas, D., Marquette, J.-B., Martin, R., Meintjes, P., Menzies, J., Pollard, K. R., Williams, A., Wouters, D., The PLANET Collaboration, Bramich, D. M., Dominik, M., Horne, K., Browne, P., Hundertmark, M., Ipatov, S., Kains, N., Snodgrass, C., Steele, I. A., Street, R. A., The RoboNet Collaboration
The Astrophysical Journal, 778, 55 (2013)

7. "Microlensing Discovery of a Tight, Low-mass-ratio Planetary-mass Object around an Old Field Brown Dwarf"
Han, C., Jung, Y. K., Udalski, A., Sumi, T., Gaudi, B. S., Gould, A., Bennett, D. P., Tsapras, Y., Szymański, M. K., Kubiak, M., Pietrzyński, G., Soszyński, I., Skowron, J., Kozłowski, S., Poleski, R., Ulaczyk, K., Wyrzykowski, Ł., Pietrukowicz, P., The OGLE Collaboration, Abe, F., Bond, I. A., Botzler, C. S., Chote, P., Freeman, M., Fukui, A., Furusawa, K., Harris, P., Itow, Y., Ling, C. H., Masuda, K., Matsubara, Y., Muraki, Y., Ohnishi, K., Rattenbury, N. J., Saito, To., Sullivan, D. J., Sweatman, W. L., **Suzuki, D.**, Tristram, P. J., Wada, K., Yock, P. C. M., The MOA Collaboration, Batista, V., Christie, G., Choi, J.-Y., DePoy, D. L., Dong, Subo, Hwang, K.-H., Kavka, A., Lee, C.-U., Monard, L. A. G., Natusch, T., Ngan, H., Park, H., Pogge, R. W., Porritt, I., Shin, I.-G., Tan, T. G., Yee, J. C., The μFUN Collaboration, Alsubai, K. A., Bozza, V., Bramich, D. M., Browne, P., Dominik, M., Horne, K., Hundertmark, M., Ipatov, S., Kains, N., Liebig, C., Snodgrass, C., Steele, I. A., Street, R. A., The RoboNet Collaboration
The Astrophysical Journal, 778, 38 (2013)

8. "MOA-2010-BLG-311: A Planetary Candidate below the Threshold of Reliable Detection"
Yee, J. C., Hung, L.-W., Bond, I. A., Allen, W., Monard, L. A. G., Albrow, M. D., Fouqué, P., Dominik, M., Tsapras, Y., Udalski, A., Gould, A., Zellem, R., Bos, M., Christie, G. W., DePoy, D. L., Dong, Subo, Drummond, J., Gaudi, B. S., Gorbikov, E., Han, C., Kaspi, S., Klein, N., Lee, C.-U., Maoz, D., McCormick, J., Moorhouse, D., Natusch, T., Nola, M., Park, B.-G., Pogge, R. W., Polishook, D., Shporer, A., Shvartzvald, Y., Skowron, J., Thornley, G., The μFUN Collaboration, Abe, F., Bennett, D. P., Botzler, C. S., Chote, P., Freeman, M., Fukui, A., Furusawa, K., Harris, P., Itow, Y., Ling, C. H., Masuda, K., Matsubara, Y., Miyake, N., Ohnishi, K., Rattenbury, N. J., Saito, To., Sullivan, D. J., Sumi, T., **Suzuki, D.**, Sweatman, W. L., Tristram, P. J., Wada, K., Yock, P. C. M., The MOA Collaboration, Szymański, M. K., Soszyński, I., Kubiak, M., Poleski, R., Ulaczyk, K., Pietrzyński, G., Wyrzykowski, Ł., The OGLE Collaboration, Bachelet, E., Batista, V., Beatty, T. G., Beaulieu, J.-P., Bennett, C. S., Bowens-Rubin, R., Brillant, S., Caldwell, J. A. R., Cassan, A., Cole, A. A., Corrales, E., Coutures, C., Dieters, S., Dominis Prester, D., Donatowicz, J., Greenhill, J., Henderson, C. B., Kubas, D., Marquette, J.-B., Martin, R., Menzies, J. W., Shappee, B., Williams, A., Wouters, D., van Saders, J., Zub, M., The PLANET Collaboration, Street, R. A., Horne, K., Bramich, D. M., Steele, I. A., The RoboNet Collaboration, Alsubai, K. A., Bozza, V., Browne, P., Burgdorf, M. J., Calchi Novati, S., Dodds, P., Finet, F., Gerner, T., Hardis, S., Harpsøe, K., Hessman, F. V., Hinse, T. C., Hundertmark, M., Jørgensen, U. G., Kains, N., Kerins, E., Liebig, C., Mancini, L., Mathiasen, M., Penny, M. T., Proft, S., Rahvar, S., Ricci, D., Sahu, K. C., Scarpetta, G., Schäfer, S., Schönebeck, F., Snodgrass, C., Southworth, J., Surdej, J., Wambsganss, J., The MiNDSTEp Consortium

The Astrophysical Journal, 769, 77 (2013)

9. "Microlensing Discovery of a Population of Very Tight, Very Low Mass Binary Brown Dwarfs"
Choi, J.-Y., Han, C., Udalski, A., Sumi, T., Gaudi, B. S., Gould, A., Bennett, D. P., Dominik, M., Beaulieu, J.-P., Tsapras, Y., Bozza, V., Abe, F., Bond, I. A., Botzler, C. S., Chote, P., Freeman, M., Fukui, A., Furusawa, K., Itow, Y., Ling, C. H., Masuda, K., Matsubara, Y., Miyake, N., Muraki, Y., Ohnishi, K., Rattenbury, N. J., Saito, To., Sullivan, D. J., Suzuki, K., Sweatman, W. L., **Suzuki, D.**, Takino, S., Tristram, P. J., Wada, K., Yock, P. C. M., The MOA Collaboration, Szymański, M. K., Kubiak, M., Pietrzyński, G., Soszyński, I., Skowron, J., Kozłowski, S., Poleski, R., Ulaczyk, K., Wyrzykowski, Ł., Pietrukowicz, P., The OGLE Collaboration, Almeida, L. A., DePoy, D. L., Dong, Subo, Gorbikov, E., Jablonski, F., Henderson, C. B., Hwang, K.-H., Janczak, J., Jung, Y.-K., Kaspi, S., Lee, C.-U., Malamud, U., Maoz, D., McGregor, D., Muñoz, J. A., Park, B.-G., Park, H., Pogge, R. W., Shvartzvald, Y., Shin, I.-G., Yee, J. C., The μFUN Collaboration, Alsubai, K. A., Browne, P., Burgdorf, M. J., Calchi Novati, S., Dodds, P., Fang, X.-S., Finet, F., Glitrup, M., Grundahl, F., Gu, S.-H., Hardis, S., Harpsøe, K., Hinse, T. C., Hornstrup, A., Hundertmark, M., Jessen-Hansen, J., Jørgensen, U. G., Kains, N., Kerins, E., Liebig, C., Lund, M. N., Lundkvist, M., Maier, G., Mancini, L., Mathiasen, M., Penny, M. T., Rahvar, S., Ricci, D., Scarpetta, G., Skottfelt, J., Snodgrass, C., Southworth, J., Surdej, J., Tregloan-Reed, J., Wambsganss, J., Wertz, O., Zimmer, F., The MiNDSTEp Consortium, Albrow, M. D., Bachelet, E., Batista, V., Brillant, S., Cassan, A., Cole, A. A., Coutures, C., Dieters, S., Dominis Prester, D., Donatowicz, J., Fouqué, P., Greenhill, J., Kubas, D., Marquette, J.-B., Menzies, J. W., Sahu, K. C., Zub, M., The PLANET Collaboration, Bramich, D. M., Horne, K., Steele, I. A., Street, R. A., The RoboNet Collaboration
The Astrophysical Journal, 768, 129 (2013)

10. "A giant planet beyond the snow line in microlensing event OGLE-2011-BLG-0251"
Kains, N., Street, R. A., Choi, J.-Y., Han, C., Udalski, A., Almeida, L. A., Jablonski, F., Tristram, P. J., Jørgensen, U. G., Szymański, M. K., Kubiak, M., Pietrzyński, G., Soszyński, I., Poleski, R., Kozłowski, S., Pietrukowicz, P., Ulaczyk, K., Wyrzykowski, Ł., Skowron, J., The OGLE Collaboration, Alsubai, K. A., Bozza, V., Browne, P., Burgdorf, M. J., Calchi Novati, S., Dodds, P., Dominik, M., Dreizler, S., Fang, X.-S., Grundahl, F., Gu, C.-H., Hardis, S., Harpsøe, K., Hessman, F. V., Hinse, T. C., Hornstrup, A., Hundertmark, M., Jessen-Hansen, J., Kerins, E., Liebig, C., Lund, M., Lundkvist, M., Mancini, L., Mathiasen, M., Penny, M. T., Rahvar, S., Ricci, D., Sahu, K. C., Scarpetta, G., Skottfelt, J., Snodgrass, C., Southworth, J., Surdej, J., Tregloan-Reed, J., Wambsganss, J., Wertz, O., The MiNDSTEp Consortium, Bajek, D., Bramich, D. M., Horne, K., Ipatov, S., Steele, I. A., Tsapras, Y., The RoboNet Collaboration, Abe, F., Bennett, D. P., Bond, I. A., Botzler, C. S., Chote, P., Freeman, M., Fukui, A., Furusawa, K., Itow, Y., Ling, C. H., Masuda, K., Matsubara, Y., Miyake, N., Muraki, Y., Ohnishi, K., Rattenbury, N., Saito, T., Sullivan, D. J., Sumi, T., **Suzuki, D.**, Suzuki, K., Sweatman, W. L., Takino, S., Wada, K., Yock, P. C. M., The MOA Collaboration, Allen, W., Batista, V., Chung, S.-J., Christie, G., DePoy, D. L., Drummond, J., Gaudi, B. S., Gould, A., Henderson, C., Jung, Y.-K., Koo, J.-R., Lee, C.-U., McCormick, J., McGregor, D., Muñoz, J. A., Natusch, T., Ngan, H., Park, H., Pogge, R. W., Shin, I.-G., Yee, J., The μFUN Collaboration, Albrow, M. D., Bachelet, E., Beaulieu, J.-P., Brillant, S.,

Caldwell, J. A. R., Cassan, A., Cole, A., Corrales, E., Coutures, Ch., Dieters, S., Dominis Prester, D., Donatowicz, J., Fouqué, P., Greenhill, J., Kane, S. R., Kubas, D., Marquette, J.-B., Martin, R., Meintjes, P., Menzies, J., Pollard, K. R., Williams, A., Wouters, D., Zub, M., The PLANET Collaboration
Astronomy & Astrophysics, 552, A70 (2013)

11. "Using Orbital Effects to Break the Close/Wide Degeneracy in Binary-lens Microlensing Events"
Shin, I.-G., Sumi, T., Udalski, A., Choi, J. Y., Han, C., Gould, A., Abe, F., Bennett, D. P., Bond, I. A., Botzler, C. S., Chote, P., Freeman, M., Fukui, A., Furusawa, K., Harris, P., Itow, Y., Ling, C. H., Masuda, K., Matsubara, Y., Miyake, N., Muraki, Y., Ohnishi, K., Rattenbury, N., Saito, To., Sullivan, D. J., **Suzuki, D.**, Sweatman, W. L., Tristram, P. J., Wada, K., Yock, P. C. M., The MOA Collaboration, Szymański, M. K., Kubiak, M., Soszyński, I., Pietrzyński, G., Poleski, R., Ulaczyk, K., Pietrukowicz, P., Kozłowski, S., Skowron, J., Wyrzykowski, Ł., The OGLE Collaboration
The Astrophysical Journal, 764, 64 (2013)

12. "MOA-2010-BLG-523: "Failed Planet" = RS CVn Star"
Gould, A., Yee, J. C., Bond, I. A., Udalski, A., Han, C., Jørgensen, U. G., Greenhill, J., Tsapras, Y., Pinsonneault, M. H., Bensby, T., Allen, W., Almeida, L. A., Bos, M., Christie, G. W., DePoy, D. L., Dong, Subo, Gaudi, B. S., Hung, L.-W., Jablonski, F., Lee, C.-U., McCormick, J., Moorhouse, D., Muñoz, J. A., Natusch, T., Nola, M., Pogge, R. W., Skowron, J., Thornley, G., The μFUN Collaboration, Abe, F., Bennett, D. P., Botzler, C. S., Chote, P., Freeman, M., Fukui, A., Furusawa, K., Harris, P., Itow, Y., Ling, C. H., Masuda, K., Matsubara, Y., Miyake, N., Ohnishi, K., Rattenbury, N. J., Saito, To., Sullivan, D. J., Sumi, T., **Suzuki, D.**, Sweatman, W. L., Tristram, P. J., Wada, K., Yock, P. C. M., The MOA Collaboration, Szymański, M. K., Soszyński, I., Kubiak, M., Poleski, R., Ulaczyk, K., Pietrzyński, G., Wyrzykowski, Ł., The OGLE Collaboration, Alsubai, K. A., Bozza, V., Browne, P., Burgdorf, M. J., Calchi Novati, S., Dodds, P., Dominik, M., Finet, F., Gerner, T., Hardis, S., Harpsøe, K., Hessman, F. V., Hinse, T. C., Hundertmark, M., Kains, N., Kerins, E., Liebig, C., Mancini, L., Mathiasen, M., Penny, M. T., Proft, S., Rahvar, S., Ricci, D., Sahu, K. C., Scarpetta, G., Schäfer, S., Schönebeck, F., Snodgrass, C., Southworth, J., Surdej, J., Wambsganss, J., The MiNDSTEp Consortium, Street, R. A., Horne, K., Bramich, D. M., Steele, I. A., The RoboNet Collaboration, Albrow, M. D., Bachelet, E., Batista, V., Beatty, T. G., Beaulieu, J.-P., Bennett, C. S., Bowens-Rubin, R., Brillant, S., Caldwell, J. A. R., Cassan, A., Cole, A. A., Corrales, E., Coutures, C., Dieters, S., Dominis Prester, D., Donatowicz, J., Fouqué, P., Henderson, C. B., Kubas, D., Marquette, J.-B., Martin, R., Menzies, J. W., Shappee, B., Williams, A., van Saders, J., Zub, M., The PLANET Collaboration
The Astrophysical Journal, 763, 141 (2013)

13. "MOA-2010-BLG-073L: An M-dwarf with a Substellar Companion at the Planet/Brown Dwarf Boundary"
Street, R. A., Choi, J.-Y., Tsapras, Y., Han, C., Furusawa, K., Hundertmark, M., Gould, A., Sumi, T., Bond, I. A., Wouters, D., Zellem, R., Udalski, A., The RoboNet Collaboration, Snodgrass, C., Horne, K., Dominik, M., Browne, P., Kains, N., Bramich, D. M., Bajek, D., Steele, I. A., Ipatov, S., The MOA Collaboration, Abe, F., Bennett, D. P., Botzler, C. S., Chote, P., Freeman, M., Fukui, A., Harris, P., Itow, Y., Ling, C. H., Masuda, K., Matsubara, Y., Miyake, N., Muraki, Y.,

Nagayama, T., Nishimaya, S., Ohnishi, K., Rattenbury, N., Saito, To., Sullivan, D. J., **Suzuki, D.**, Sweatman, W. L., Tristram, P. J., Wada, K., Yock, P. C. M., The OGLE Collaboration, Szymański, M. K., Kubiak, M., Pietrzyński, G., Soszyński, I., Poleski, R., Ulaczyk, K., Wyrzykowski, Ł., The μFUN Collaboration, Yee, J., Dong, S., Shin, I.-G., Lee, C.-U., Skowron, J., De Almeida, L. Andrade, DePoy, D. L., Gaudi, B. S., Hung, L.-W., Jablonski, F., Kaspi, S., Klein, N., Hwang, K.-H., Koo, J.-R., Maoz, D., Muñoz, J. A., Pogge, R. W., Polishhook, D., Shporer, A., McCormick, J., Christie, G., Natusch, T., Allen, B., Drummond, J., Moorhouse, D., Thornley, G., Knowler, M., Bos, M., Bolt, G., The PLANET Collaboration, Beaulieu, J.-P., Albrow, M. D., Batista, V., Brillant, S., Caldwell, J. A. R., Cassan, A., Cole, A., Corrales, E., Coutures, Ch., Dieters, S., Dominis Prester, D., Donatowicz, J., Fouqué, P., Bachelet, E., Greenhill, J., Kane, S. R., Kubas, D., Marquette, J.-B., Martin, R., Menzies, J., Pollard, K. R., Sahu, K. C., Wambsganss, J., Williams, A., Zub, M., The MiNDSTEp Consortium, Alsubai, K. A., Bozza, V., Burgdorf, M. J., Calchi Novati, S., Dodds, P., Dreizler, S., Finet, F., Gerner, T., Hardis, S., Harpsøe, K., Hessman, F., Hinse, T. C., Jørgensen, U. G., Kerins, E., Liebig, C., Mancini, L., Mathiasen, M., Penny, M. T., Proft, S., Rahvar, S., Ricci, D., Scarpetta, G., Schäfer, S., Schönebeck, F., Southworth, J., Surdej, J.
The Astrophysical Journal, 763, 67 (2013)

14. "Chemical evolution of the Galactic bulge as traced by microlensed dwarf and subgiant stars. V. Evidence for a wide age distribution and a complex MDF"
Bensby, T., Yee, J. C., Feltzing, S., Johnson, J. A., Gould, A., Cohen, J. G., Asplund, M., Meléndez, J., Lucatello, S., Han, C., Thompson, I., Gal-Yam, A., Udalski, A., Bennett, D. P., Bond, I. A., Kohei, W., Sumi, T., **Suzuki, D.**, Suzuki, K., Takino, S., Tristram, P., Yamai, N., Yonehara, A.
Astronomy & Astrophysics, 549, A147 (2013)

15. "Microlensing Binaries with Candidate Brown Dwarf Companions"
Shin, I.-G., Han, C., Gould, A., Udalski, A., Sumi, T., Dominik, M., Beaulieu, J.-P., Tsapras, Y., Bozza, V., Szymański, M. K., Kubiak, M., Soszyński, I., Pietrzyński, G., Poleski, R., Ulaczyk, K., Pietrukowicz, P., Kozłowski, S., Skowron, J., Wyrzykowski, Ł., The OGLE Collaboration, Abe, F., Bennett, D. P., Bond, I. A., Botzler, C. S., Freeman, M., Fukui, A., Furusawa, K., Hayashi, F., Hearnshaw, J. B., Hosaka, S., Itow, Y., Kamiya, K., Kilmartin, P. M., Kobara, S., Korpela, A., Lin, W., Ling, C. H., Makita, S., Masuda, K., Matsubara, Y., Miyake, N., Muraki, Y., Nagaya, M., Nishimoto, K., Ohnishi, K., Okumura, T., Omori, K., Perrott, Y. C., Rattenbury, N., Saito, To., Skuljan, L., Sullivan, D. J., **Suzuki, D.**, Sweatman, W. L., Tristram, P. J., Wada, K., Yock, P. C. M., The MOA Collaboration, Christie, G. W., Depoy, D. L., Dong, S., Gal-Yam, A., Gaudi, B. S., Hung, L.-W., Janczak, J., Kaspi, S., Maoz, D., McCormick, J., McGregor, D., Moorhouse, D., Muñoz, J. A., Natusch, T., Nelson, C., Pogge, R. W., Tan, T.-G., Polishook, D., Shvartzvald, Y., Shporer, A., Thornley, G., Malamud, U., Yee, J. C., Choi, J.-Y., Jung, Y.-K., Park, H., Lee, C.-U., Park, B.-G., Koo, J.-R., The μFUN Collaboration, Bajek, D., Bramich, D. M., Browne, P., Horne, K., Ipatov, S., Snodgrass, C., Steele, I., Street, R., Alsubai, K. A., Burgdorf, M. J., Calchi Novati, S., Dodds, P., Dreizler, S., Fang, X.-S., Grundahl, F., Gu, C.-H., Hardis, S., Harpsøe, K., Hinse, T. C., Hundertmark, M., Jessen-Hansen, J., Jørgensen, U. G., Kains, N., Kerins, E., Liebig, C., Lund, M., Lundkvist, M., Mancini, L., Mathiasen, M., Hornstrup, A., Penny, M. T., Proft, S., Rahvar, S., Ricci, D., Scarpetta, G., Skottfelt, J., Southworth, J., Surdej, J., Tregloan-Reed, J., Wertz, O.,

Zimmer, F., Albrow, M. D., Batista, V., Brillant, S., Caldwell, J. A. R., Calitz, J. J., Cassan, A., Cole, A., Cook, K. H., Corrales, E., Coutures, Ch., Dieters, S., Dominis Prester, D., Donatowicz, J., Fouqué, P., Greenhill, J., Hill, K., Hoffman, M., Kane, S. R., Kubas, D., Marquette, J.-B., Martin, R., Meintjes, P., Menzies, J., Pollard, K. R., Sahu, K. C., Wambsganss, J., Williams, A., Vinter, C., Zub, M.
The Astrophysical Journal, 760, 116 (2012)

16. "A brown dwarf orbiting an M-dwarf: MOA 2009-BLG-411L"
Bachelet, E., Fouqué, P., Han, C., Gould, A., Albrow, M. D., Beaulieu, J.-P., Bertin, E., Bond, I. A., Christie, G. W., Heyrovský, D., Horne, K., Jørgensen, U. G., Maoz, D., Mathiasen, M., Matsunaga, N., McCormick, J., Menzies, J., Nataf, D., Natusch, T., Oi, N., Renon, N., Tsapras, Y., Udalski, A., Yee, J. C., Batista, V., Bennett, D. P., Brillant, S., Caldwell, J. A. R., Cassan, A., Cole, A., Cook, K. H., Coutures, C., Dieters, S., Dominik, M., Dominis Prester, D., Donatowicz, J., Greenhill, J., Kains, N., Kane, S. R., Marquette, J.-B., Martin, R., Pollard, K. R., Sahu, K. C., Street, R. A., Wambsganss, J., Williams, A., Zub, M., The PLANET Collaboration, Bos, M., Dong, Subo, Drummond, J., Gaudi, B. S., Graff, D., Janczak, J., Kaspi, S., Kozłowski, S., Lee, C.-U., Monard, L. A. G., Muñoz, J. A., Park, B.-G., Pogge, R. W., Polishook, D., Shporer, A., The μFun Collaboration, Abe, F., Botzler, C. S., Fukui, A., Furusawa, K., Hearnshaw, J. B., Itow, Y., Korpela, A. V., Ling, C. H., Masuda, K., Matsubara, Y., Miyake, N., Muraki, Y., Ohnishi, K., Rattenbury, N. J., Saito, To., Sullivan, D., Sumi, T., **Suzuki, D.**, Sweatman, W. L., Tristram, P. J., Wada, K., The MOA Collaboration, Allan, A., Bode, M. F., Bramich, D. M., Clay, N., Fraser, S. N., Hawkins, E., Kerins, E., Lister, T. A., Mottram, C. J., Saunders, E. S., Snodgrass, C., Steele, I. A., Wheatley, P. J., The RoboNet-II Collaboration, Bozza, V., Browne, P., Burgdorf, M. J., Calchi Novati, S., Dreizler, S., Finet, F., Glitrup, M., Grundahl, F., Harpsøe, K., Hessman, F. V., Hinse, T. C., Hundertmark, M., Liebig, C., Maier, G., Mancini, L., Rahvar, S., Ricci, D., Scarpetta, G., Skottfelt, J., Southworth, J., Surdej, J., Zimmer, F., The MiNDSTEp Consortium
Astronomy & Astrophysics, 547, A55 (2012)

17. "Planetary and Other Short Binary Microlensing Events from the MOA Short-event Analysis"
Bennett, D. P., Sumi, T., Bond, I. A., Kamiya, K., Abe, F., Botzler, C. S., Fukui, A., Furusawa, K., Itow, Y., Korpela, A. V., Kilmartin, P. M., Ling, C. H., Masuda, K., Matsubara, Y., Miyake, N., Muraki, Y., Ohnishi, K., Rattenbury, N. J., Saito, To., Sullivan, D. J., **Suzuki, D.**, Sweatman, W. L., Tristram, P. J., Wada, K., Yock, P. C. M., The MOA Collaboration
The Astrophysical Journal, 757, 119 (2012)

18. "A New Type of Ambiguity in the Planet and Binary Interpretations of Central Perturbations of High-magnification Gravitational Microlensing Events"
Choi, J.-Y., Shin, I.-G., Han, C., Udalski, A., Sumi, T., Gould, A., Bozza, V., Dominik, M., Fouqué, P., Horne, K., Szymański, M. K., Kubiak, M., Soszyński, I., Pietrzyński, G., Poleski, R., Ulaczyk, K., Pietrukowicz, P., Kozłowski, S., Skowron, J., Wyrzykowski, Ł., The OGLE Collaboration, Abe, F., Bennett, D. P., Bond, I. A., Botzler, C. S., Chote, P., Freeman, M., Fukui, A., Furusawa, K., Itow, Y., Kobara, S., Ling, C. H., Masuda, K., Matsubara, Y., Miyake, N., Muraki, Y., Ohmori, K., Ohnishi, K., Rattenbury, N. J., Saito, To., Sullivan, D. J., **Suzuki, D.**, Suzuki, K., Sweatman, W. L., Takino, S., Tristram, P. J., Wada, K., Yock, P. C. M.,

The MOA Collaboration, Bramich, D. M., Snodgrass, C., Steele, I. A., Street, R. A., Tsapras, Y., The RoboNet Collaboration, Alsubai, K. A., Browne, P., Burgdorf, M. J., Calchi Novati, S., Dodds, P., Dreizler, S., Fang, X.-S., Grundahl, F., Gu, C.-H., Hardis, S., Harpsøe, K., Hinse, T. C., Hornstrup, A., Hundertmark, M., Jessen-Hansen, J., Jørgensen, U. G., Kains, N., Kerins, E., Liebig, C., Lund, M., Lunkkvist, M., Mancini, L., Mathiasen, M., Penny, M. T., Rahvar, S., Ricci, D., Scarpetta, G., Skottfelt, J., Southworth, J., Surdej, J., Tregloan-Reed, J., Wambsganss, J., Wertz, O., The MiNDSTEp Consortium, Almeida, L. A., Batista, V., Christie, G., DePoy, D. L., Dong, Subo, Gaudi, B. S., Henderson, C., Jablonski, F., Lee, C.-U., McCormick, J., McGregor, D., Moorhouse, D., Natusch, T., Ngan, H., Pogge, R. W., Tan, T.-G., Thornley, G., Yee, J. C., The μFUN Collaboration, Albrow, M. D., Bachelet, E., Beaulieu, J.-P., Brillant, S., Cassan, A., Cole, A. A., Corrales, E., Coutures, C., Dieters, S., Dominis Prester, D., Donatowicz, J., Greenhill, J., Kubas, D., Marquette, J.-B., Menzies, J. W., Sahu, K. C., Zub, M., The PLANET Collaboration
The Astrophysical Journal, 756, 48 (2012)

19. "OGLE-2008-BLG-510: first automated real-time detection of a weak microlensing anomaly - brown dwarf or stellar binary?"
Bozza, V., Dominik, M., Rattenbury, N. J., Jørgensen, U. G., Tsapras, Y., Bramich, D. M., Udalski, A., Bond, I. A., Liebig, C., Cassan, A., Fouqué, P., Fukui, A., Hundertmark, M., Shin, I.-G., Lee, S. H., Choi, J.-Y., Park, S.-Y., Gould, A., Allan, A., Mao, S., Wyrzykowski, Ł., Street, R. A., Buckley, D., Nagayama, T., Mathiasen, M., Hinse, T. C., Novati, S. Calchi, Harpsøe, K., Mancini, L., Scarpetta, G., Anguita, T., Burgdorf, M. J., Horne, K., Hornstrup, A., Kains, N., Kerins, E., Kjærgaard, P., Masi, G., Rahvar, S., Ricci, D., Snodgrass, C., Southworth, J., Steele, I. A., Surdej, J., Thöne, C. C., Wambsganss, J., Zub, M., Albrow, M. D., Batista, V., Beaulieu, J.-P., Bennett, D. P., Caldwell, J. A. R., Cole, A. A., Cook, K. H., Coutures, C., Dieters, S., Prester, D. Dominis, Donatowicz, J., Greenhill, J., Kane, S. R., Kubas, D., Marquette, J.-B., Martin, R., Menzies, J., Pollard, K. R., Sahu, K. C., Williams, A., Szymański, M. K., Kubiak, M., Pietrzyński, G., Soszyński, I., Poleski, R., Ulaczyk, K., DePoy, D. L., Dong, Subo, Han, C., Janczak, J., Lee, C.-U., Pogge, R. W., Abe, F., Furusawa, K., Hearnshaw, J. B., Itow, Y., Kilmartin, P. M., Korpela, A. V., Lin, W., Ling, C. H., Masuda, K., Matsubara, Y., Miyake, N., Muraki, Y., Ohnishi, K., Perrott, Y. C., Saito, To., Skuljan, L., Sullivan, D. J., Sumi, T., **Suzuki, D.**, Sweatman, W. L., Tristram, P. J., Wada, K., Yock, P. C. M., Gulbis, A., Hashimoto, Y., Kniazev, A., Vaisanen, P.
Monthly Notices of the Royal Astronomical Society, 424, 902 (2012)

20. "MOA-2011-BLG-293Lb: A Test of Pure Survey Microlensing Planet Detections"
Yee, J. C., Shvartzvald, Y., Gal-Yam, A., Bond, I. A., Udalski, A., Kozłowski, S., Han, C., Gould, A., Skowron, J., **Suzuki, D.**, Abe, F., Bennett, D. P., Botzler, C. S., Chote, P., Freeman, M., Fukui, A., Furusawa, K., Itow, Y., Kobara, S., Ling, C. H., Masuda, K., Matsubara, Y., Miyake, N., Muraki, Y., Ohmori, K., Ohnishi, K., Rattenbury, N. J., Saito, To., Sullivan, D. J., Sumi, T., Suzuki, K., Sweatman, W. L., Takino, S., Tristram, P. J., Wada, K., The MOA Collaboration, Szymański, M. K., Kubiak, M., Pietrzyński, G., Soszyński, I., Poleski, R., Ulaczyk, K., Wyrzykowski, Ł., Pietrukowicz, P., The OGLE Collaboration, Allen, W., Almeida, L. A., Batista, V., Bos, M., Christie, G., DePoy, D. L., Dong, Subo, Drummond, J., Finkelman, I., Gaudi, B. S., Gorbikov, E., Henderson, C., Higgins, D., Jablonski, F., Kaspi, S., Manulis, I., Maoz, D., McCormick, J., McGregor, D., Monard, L. A. G., Moorhouse, D.,

Muñoz, J. A., Natusch, T., Ngan, H., Ofek, E., Pogge, R. W., Santallo, R., Tan, T.-G., Thornley, G., Shin, I.-G., Choi, J.-Y., Park, S.-Y., Lee, C.-U., Koo, J.-R., The μFUN Collaboration
The Astrophysical Journal, 755, 102 (2012)

21. "Characterizing Low-mass Binaries from Observation of Long-timescale Caustic-crossing Gravitational Microlensing Events"
Shin, I.-G., Han, C., Choi, J.-Y., Udalski, A., Sumi, T., Gould, A., Bozza, V., Dominik, M., Fouqué, P., Horne, K., Szymański, M. K., Kubiak, M., Soszyński, I., Pietrzyński, G., Poleski, R., Ulaczyk, K., Pietrukowicz, P., Kozłowski, S., Skowron, J., Wyrzykowski, Ł., The OGLE Collaboration, Abe, F., Bennett, D. P., Bond, I. A., Botzler, C. S., Chote, P., Freeman, M., Fukui, A., Furusawa, K., Itow, Y., Kobara, S., Ling, C. H., Masuda, K., Matsubara, Y., Miyake, N., Muraki, Y., Ohmori, K., Ohnishi, K., Rattenbury, N. J., Saito, To., Sullivan, D. J., **Suzuki, D.**, Suzuki, K., Sweatman, W. L., Takino, S., Tristram, P. J., Wada, K., Yock, P. C. M., The MOA Collaboration, Bramich, D. M., Snodgrass, C., Steele, I. A., Street, R. A., Tsapras, Y., The RoboNet Collaboration, Alsubai, K. A., Browne, P., Burgdorf, M. J., Calchi Novati, S., Dodds, P., Dreizler, S., Fang, X.-S., Grundahl, F., Gu, C.-H., Hardis, S., Harpsøe, K., Hinse, T. C., Hornstrup, A., Hundertmark, M., Jessen-Hansen, J., Jørgensen, U. G., Kains, N., Kerins, E., Liebig, C., Lund, M., Lunkkvist, M., Mancini, L., Mathiasen, M., Penny, M. T., Rahvar, S., Ricci, D., Scarpetta, G., Skottfelt, J., Southworth, J., Surdej, J., Tregloan-Reed, J., Wambsganss, J., Wertz, O., The MiNDSTEp Consortium, Almeida, L. A., Batista, V., Christie, G., DePoy, D. L., Dong, Subo, Gaudi, B. S., Henderson, C., Jablonski, F., Lee, C.-U., McCormick, J., McGregor, D., Moorhouse, D., Natusch, T., Ngan, H., Park, S.-Y., Pogge, R. W., Tan, T.-G., Thornley, G., Yee, J. C., The μFUN Collaboration, Albrow, M. D., Bachelet, E., Beaulieu, J.-P., Brillant, S., Cassan, A., Cole, A. A., Corrales, E., Coutures, C., Dieters, S., Dominis Prester, D., Donatowicz, J., Greenhill, J., Kubas, D., Marquette, J.-B., Menzies, J. W., Sahu, K. C., Zub, M., The PLANET Collaboration
The Astrophysical Journal, 755, 91 (2012)

22. "MOA 2010-BLG-477Lb: Constraining the Mass of a Microlensing Planet from Microlensing Parallax, Orbital Motion, and Detection of Blended Light"
Bachelet, E., Shin, I.-G., Han, C., Fouqué, P., Gould, A., Menzies, J. W., Beaulieu, J.-P., Bennett, D. P., Bond, I. A., Dong, Subo, Heyrovský, D., Marquette, J.-B., Marshall, J., Skowron, J., Street, R. A., Sumi, T., Udalski, A., Abe, L., Agabi, K., Albrow, M. D., Allen, W., Bertin, E., Bos, M., Bramich, D. M., Chavez, J., Christie, G. W., Cole, A. A., Crouzet, N., Dieters, S., Dominik, M., Drummond, J., Greenhill, J., Guillot, T., Henderson, C. B., Hessman, F. V., Horne, K., Hundertmark, M., Johnson, J. A., Jørgensen, U. G., Kandori, R., Liebig, C., Mékarnia, D., McCormick, J., Moorhouse, D., Nagayama, T., Nataf, D., Natusch, T., Nishiyama, S., Rivet, J.-P., Sahu, K. C., Shvartzvald, Y., Thornley, G., Tomczak, A. R., Tsapras, Y., Yee, J. C., Batista, V., Bennett, C. S., Brillant, S., Caldwell, J. A. R., Cassan, A., Corrales, E., Coutures, C., Dominis Prester, D., Donatowicz, J., Kubas, D., Martin, R., Williams, A., Zub, M., The PLANET Collaboration, de Almeida, L. Andrade, DePoy, D. L., Gaudi, B. S., Hung, L.-W., Jablonski, F., Kaspi, S., Klein, N., Lee, C.-U., Lee, Y., Koo, J.-R., Maoz, D., Muñoz, J. A., Pogge, R. W., Polishook, D., Shporer, A., The μFUN Collaboration, Abe, F., Botzler, C. S., Chote, P., Freeman, M., Fukui, A., Furusawa, K., Harris, P., Itow, Y., Kobara, S., Ling, C. H., Masuda, K., Matsubara, Y., Miyake, N., Ohmori, K., Ohnishi, K., Rattenbury, N. J., Saito, To.,

Sullivan, D. J., **Suzuki, D.**, Sweatman, W. L., Tristram, P. J., Wada, K., Yock, P. C. M., The MOA Collaboration, Szymański, M. K., Soszyński, I., Kubiak, M., Poleski, R., Ulaczyk, K., Pietrzyński, G., Wyrzykowski, Ł., The OGLE Collaboration, Kains, N., Snodgrass, C., Steele, I. A., The RoboNet Collaboration, Alsubai, K. A., Bozza, V., Browne, P., Burgdorf, M. J., Calchi Novati, S., Dodds, P., Dreizler, S., Finet, F., Gerner, T., Hardis, S., Harpsøe, K., Hinse, T. C., Kerins, E., Mancini, L., Mathiasen, M., Penny, M. T., Proft, S., Rahvar, S., Ricci, D., Scarpetta, G., Schäfer, S., Schönebeck, F., Southworth, J., Surdej, J., Wambsganss, J., The MiNDSTEp Consortium
The Astrophysical Journal, 754, 73 (2012)

23. "Characterizing Lenses and Lensed Stars of High-magnification Single-lens Gravitational Microlensing Events with Lenses Passing over Source Stars"
Choi, J.-Y., Shin, I.-G., Park, S.-Y., Han, C., Gould, A., Sumi, T., Udalski, A., Beaulieu, J.-P., Street, R., Dominik, M., Allen, W., Almeida, L. A., Bos, M., Christie, G. W., Depoy, D. L., Dong, S., Drummond, J., Gal-Yam, A., Gaudi, B. S., Henderson, C. B., Hung, L.-W., Jablonski, F., Janczak, J., Lee, C.-U., Mallia, F., Maury, A., McCormick, J., McGregor, D., Monard, L. A. G., Moorhouse, D., Muñoz, J. A., Natusch, T., Nelson, C., Park, B.-G., Pogge, R. W., "TG" Tan, T.-G., Thornley, G., Yee, J. C., The μFUN Collaboration, Abe, F., Barnard, E., Baudry, J., Bennett, D. P., Bond, I. A., Botzler, C. S., Freeman, M., Fukui, A., Furusawa, K., Hayashi, F., Hearnshaw, J. B., Hosaka, S., Itow, Y., Kamiya, K., Kilmartin, P. M., Kobara, S., Korpela, A., Lin, W., Ling, C. H., Makita, S., Masuda, K., Matsubara, Y., Miyake, N., Muraki, Y., Nagaya, M., Nishimoto, K., Ohnishi, K., Okumura, T., Omori, K., Perrott, Y. C., Rattenbury, N., Saito, To., Skuljan, L., Sullivan, D. J., **Suzuki, D.**, Suzuki, K., Sweatman, W. L., Takino, S., Tristram, P. J., Wada, K., Yock, P. C. M., The MOA Collaboration, Szymański, M. K., Kubiak, M., Pietrzyński, G., Soszyński, I., Poleski, R., Ulaczyk, K., Wyrzykowski, Ł., Kozłowski, S., Pietrukowicz, P., The OGLE Collaboration, Albrow, M. D., Bachelet, E., Batista, V., Bennett, C. S., Bowens-Rubin, R., Brillant, S., Cassan, A., Cole, A., Corrales, E., Coutures, Ch., Dieters, S., Dominis Prester, D., Donatowicz, J., Fouqué, P., Greenhill, J., Kane, S. R., Menzies, J., Sahu, K. C., Wambsganss, J., Williams, A., Zub, M., The PLANET Collaboration, Allan, A., Bramich, D. M., Browne, P., Clay, N., Fraser, S., Horne, K., Kains, N., Mottram, C., Snodgrass, C., Steele, I., Tsapras, Y., The RoboNet Collaboration, Alsubai, K. A., Bozza, V., Burgdorf, M. J., Calchi Novati, S., Dodds, P., Dreizler, S., Finet, F., Gerner, T., Glitrup, M., Grundahl, F., Hardis, S., Harpsøe, K., Hinse, T. C., Hundertmark, M., Jørgensen, U. G., Kerins, E., Liebig, C., Maier, G., Mancini, L., Mathiasen, M., Penny, M. T., Proft, S., Rahvar, S., Ricci, D., Scarpetta, G., Schäfer, S., Schönebeck, F., Skottfelt, J., Surdej, J., Southworth, J., Zimmer, F., The MiNDSTEp Consortium
The Astrophysical Journal, 751, 41 (2012)

24. "Microlensing Binaries Discovered through High-magnification Channel"
Shin, I.-G., Choi, J.-Y., Park, S.-Y., Han, C., Gould, A., Sumi, T., Udalski, A., Beaulieu, J.-P., Dominik, M., Allen, W., Bos, M., Christie, G. W., Depoy, D. L., Dong, S., Drummond, J., Gal-Yam, A., Gaudi, B. S., Hung, L.-W., Janczak, J., Kaspi, S., Lee, C.-U., Mallia, F., Maoz, D., Maury, A., McCormick, J., Monard, L. A. G., Moorhouse, D., Muñoz, J. A., Natusch, T., Nelson, C., Park, B.-G., Pogge, R. W., Polishook, D., Shvartzvald, Y., Shporer, A., Thornley, G., Yee, J. C., The μFUN Collaboration, Abe, F., Bennett, D. P., Bond, I. A., Botzler, C. S., Fukui, A., Furusawa, K., Hayashi, F., Hearnshaw, J. B., Hosaka, S., Itow, Y., Kamiya, K.,

Kilmartin, P. M., Kobara, S., Korpela, A., Lin, W., Ling, C. H., Makita, S., Masuda, K., Matsubara, Y., Miyake, N., Muraki, Y., Nagaya, M., Nishimoto, K., Ohnishi, K., Okumura, T., Omori, K., Perrott, Y. C., Rattenbury, N., Saito, To., Skuljan, L., Sullivan, D. J., **Suzuki, D.**, Sweatman, W. L., Tristram, P. J., Wada, K., Yock, P. C. M., The MOA Collaboration, Szymański, M. K., Kubiak, M., Pietrzyński, G., Soszyński, I., Poleski, R., Ulaczyk, K., Wyrzykowski, Ł., Kozłowski, S., Pietrukowicz, P., The OGLE Collaboration, Albrow, M. D., Batista, V., Bramich, D. M., Brillant, S., Caldwell, J. A. R., Calitz, J. J., Cassan, A., Cole, A., Cook, K. H., Corrales, E., Coutures, Ch., Dieters, S., Dominis Prester, D., Donatowicz, J., Fouqué, P., Greenhill, J., Hoffman, M., Jørgensen, U. G., Kane, S. R., Kubas, D., Marquette, J.-B., Martin, R., Meintjes, P., Menzies, J., Pollard, K. R., Sahu, K. C., Wambsganss, J., Williams, A., Vinter, C., Zub, M., The PLANET Collaboration, Allan, A., Browne, P., Horne, K., Snodgrass, C., Steele, I., Street, R., Tsapras, Y., The RoboNet Collaboration, Alsubai, K. A., Bozza, V., Browne, P., Burgdorf, M. J., Calchi Novati, S., Dodds, P., Dreizler, S., Finet, F., Gerner, T., Glitrup, M., Grundahl, F., Hardis, S., Harpsøe, K., Hessman, F. V., Hinse, T. C., Hundertmark, M., Kains, N., Kerins, E., Liebig, C., Maier, G., Mancini, L., Mathiasen, M., Penny, M. T., Proft, S., Rahvar, S., Ricci, D., Scarpetta, G., Schäfer, S., Schönebeck, F., Skottfelt, J., Surdej, J., Southworth, J., Zimmer, F., The MiNDSTEp Consortium
The Astrophysical Journal, 746, 127 (2012)

25. "Discovery and Mass Measurements of a Cold, 10 Earth Mass Planet and Its Host Star"
Muraki, Y., Han, C., Bennett, D. P., **Suzuki, D.**, Monard, L. A. G., Street, R., Jørgensen, U. G., Kundurthy, P., Skowron, J., Becker, A. C., Albrow, M. D., Fouqué, P., Heyrovský, D., Barry, R. K., Beaulieu, J.-P., Wellnitz, D. D., Bond, I. A., Sumi, T., Dong, S., Gaudi, B. S., Bramich, D. M., Dominik, M., Abe, F., Botzler, C. S., Freeman, M., Fukui, A., Furusawa, K., Hayashi, F., Hearnshaw, J. B., Hosaka, S., Itow, Y., Kamiya, K., Korpela, A. V., Kilmartin, P. M., Lin, W., Ling, C. H., Makita, S., Masuda, K., Matsubara, Y., Miyake, N., Nishimoto, K., Ohnishi, K., Perrott, Y. C., Rattenbury, N. J., Saito, To., Skuljan, L., Sullivan, D. J., Sweatman, W. L., Tristram, P. J., Wada, K., Yock, P. C. M., The MOA Collaboration, Christie, G. W., DePoy, D. L., Gorbikov, E., Gould, A., Kaspi, S., Lee, C.-U., Mallia, F., Maoz, D., McCormick, J., Moorhouse, D., Natusch, T., Park, B.-G., Pogge, R. W., Polishook, D., Shporer, A., Thornley, G., Yee, J. C., The μFUN Collaboration, Allan, A., Browne, P., Horne, K., Kains, N., Snodgrass, C., Steele, I., Tsapras, Y., The RoboNet Collaboration, Batista, V., Bennett, C. S., Brillant, S., Caldwell, J. A. R., Cassan, A., Cole, A., Corrales, R., Coutures, Ch., Dieters, S., Dominis Prester, D., Donatowicz, J., Greenhill, J., Kubas, D., Marquette, J.-B., Martin, R., Menzies, J., Sahu, K. C., Waldman, I., Williams, A., Zub, M., The PLANET Collaboration, Bourhrous, H., Matsuoka, Y., Nagayama, T., Oi, N., Randriamanakoto, Z., IRSF Observers, Bozza, V., Burgdorf, M. J., Calchi Novati, S., Dreizler, S., Finet, F., Glitrup, M., Harpsøe, K., Hinse, T. C., Hundertmark, M., Liebig, C., Maier, G., Mancini, L., Mathiasen, M., Rahvar, S., Ricci, D., Scarpetta, G., Skottfelt, J., Surdej, J., Southworth, J., Wambsganss, J., Zimmer, F., The MiNDSTEp Consortium, Udalski, A., Poleski, R., Wyrzykowski, Ł., Ulaczyk, K., Szymański, M. K., Kubiak, M., Pietrzyński, G., Soszyński, I., The OGLE Collaboration
The Astrophysical Journal, 741, 22 (2011)

26. "Binary Microlensing Event OGLE-2009-BLG-020 Gives Verifiable Mass, Distance, and

Orbit Predictions"
Skowron, J., Udalski, A., Gould, A., Dong, Subo, Monard, L. A. G., Han, C., Nelson, C. R., McCormick, J., Moorhouse, D., Thornley, G., Maury, A., Bramich, D. M., Greenhill, J., Kozłowski, S., Bond, I., Poleski, R., Wyrzykowski, Ł., Ulaczyk, K., Kubiak, M., Szymański, M. K., Pietrzyński, G., Soszyński, I., The OGLE Collaboration, Gaudi, B. S., Yee, J. C., Hung, L.-W., Pogge, R. W., DePoy, D. L., Lee, C.-U., Park, B.-G., Allen, W., Mallia, F., Drummond, J., Bolt, G., The μFUN Collaboration, Allan, A., Browne, P., Clay, N., Dominik, M., Fraser, S., Horne, K., Kains, N., Mottram, C., Snodgrass, C., Steele, I., Street, R. A., Tsapras, Y., The RoboNet Collaboration, Abe, F., Bennett, D. P., Botzler, C. S., Douchin, D., Freeman, M., Fukui, A., Furusawa, K., Hayashi, F., Hearnshaw, J. B., Hosaka, S., Itow, Y., Kamiya, K., Kilmartin, P. M., Korpela, A., Lin, W., Ling, C. H., Makita, S., Masuda, K., Matsubara, Y., Muraki, Y., Nagayama, T., Miyake, N., Nishimoto, K., Ohnishi, K., Perrott, Y. C., Rattenbury, N., Saito, To., Skuljan, L., Sullivan, D. J., Sumi, T., **Suzuki, D.**, Sweatman, W. L., Tristram, P. J., Wada, K., Yock, P. C. M., The MOA Collaboration, Beaulieu, J.-P., Fouqué, P., Albrow, M. D., Batista, V., Brillant, S., Caldwell, J. A. R., Cassan, A., Cole, A., Cook, K. H., Coutures, Ch., Dieters, S., Dominis Prester, D., Donatowicz, J., Kane, S. R., Kubas, D., Marquette, J.-B., Martin, R., Menzies, J., Sahu, K. C., Wambsganss, J., Williams, A., Zub, M., The PLANET Collaboration
The Astrophysical Journal, 738, 87 (2011)

27. "Chemical evolution of the Galactic bulge as traced by microlensed dwarf and subgiant stars. IV. Two bulge populations"
Bensby, T., Adén, D., Meléndez, J., Gould, A., Feltzing, S., Asplund, M., Johnson, J. A., Lucatello, S., Yee, J. C., Ramírez, I., Cohen, J. G., Thompson, I., Bond, I. A., Gal-Yam, A., Han, C., Sumi, T., **Suzuki, D.**, Wada, K., Miyake, N., Furusawa, K., Ohmori, K., Saito, To., Tristram, P. J., Bennett, D. P.
Astronomy & Astrophysics, 533, A134 (2011)

28. "1 μm Excess Sources in the UKIDSS. I. Three T Dwarfs in the Sloan Digital Sky Survey Southern Equatorial Stripe"
Matsuoka, Y., Peterson, B. A., Murata, K. L., Fujiwara, M., Nagayama, T., Suenaga, T., Furusawa, K., Miyake, N., Omori, K., **Suzuki, D.**, Wada, K.
The Astronomical Journal, 142, 64 (2011)

29. "Measurements of Transit Timing Variations for WASP-5b"
Fukui, Akihiko, Narita, Norio, Tristram, Paul J., Sumi, Takahiro, Abe, Fumio, Itow, Yoshitaka, Sullivan, Denis J., Bond, Ian A., Hirano, Teruyuki, Tamura, Motohide, Bennett, David P., Furusawa, Kei, Hayashi, Fumiya, Hearnshaw, John B., Hosaka, Shun, Kamiya, Koki, Kobara, Shuhei, Korpela, Aarno, Kilmartin, Pam M., Lin, Wei, Ling, Cho Hong, Makita, Shota, Masuda, Kimiaki, Matsubara, Yutaka, Miyake, Noriyuki, Muraki, Yasushi, Nagaya, Maiko, Nishimoto, Kenta, Ohnishi, Kouji, Omori, Kengo, Perrott, Yvette, Rattenbury, Nicholas, Saito, Toshiharu, Skuljan, Ljiljana, **Suzuki, Daisuke**, Sweatman, Winston L., Wada, Kohei
Publications of the Astronomical Society of Japan, 63, 287 (2011)

30. "A Sub-Saturn Mass Planet, MOA-2009-BLG-319Lb"
Miyake, N., Sumi, T., Dong, Subo, Street, R., Mancini, L., Gould, A., Bennett, D. P., Tsapras, Y., Yee, J. C., Albrow, M. D., Bond, I. A., Fouqué, P., Browne, P., Han, C., Snodgrass, C., Finet, F., Furusawa, K., Harpsøe, K., Allen, W., Hundertmark, M.,

Freeman, M., **Suzuki, D.**, Abe, F., Botzler, C. S., Douchin, D., Fukui, A., Hayashi, F., Hearnshaw, J. B., Hosaka, S., Itow, Y., Kamiya, K., Kilmartin, P. M., Korpela, A., Lin, W., Ling, C. H., Makita, S., Masuda, K., Matsubara, Y., Muraki, Y., Nagayama, T., Nishimoto, K., Ohnishi, K., Perrott, Y. C., Rattenbury, N., Saito, To., Skuljan, L., Sullivan, D. J., Sweatman, W. L., Tristram, P. J., Wada, K., Yock, P. C. M., The MOA Collaboration, Bolt, G., Bos, M., Christie, G. W., DePoy, D. L., Drummond, J., Gal-Yam, A., Gaudi, B. S., Gorbikov, E., Higgins, D., Hwang, K.-H., Janczak, J., Kaspi, S., Lee, C.-U., Koo, J.-R., Kozłowski, S., Lee, Y., Mallia, F., Maury, A., Maoz, D., McCormick, J., Monard, L. A. G., Moorhouse, D., Muñoz, J. A., Natusch, T., Ofek, E. O., Pogge, R. W., Polishook, D., Santallo, R., Shporer, A., Spector, O., Thornley, G., The μFUN Collaboration, Allan, A., Bramich, D. M., Horne, K., Kains, N., Steele, I., The RoboNet Collaboration, Bozza, V., Burgdorf, M. J., Calchi Novati, S., Dominik, M., Dreizler, S., Glitrup, M., Hessman, F. V., Hinse, T. C., Jørgensen, U. G., Liebig, C., Maier, G., Mathiasen, M., Rahvar, S., Ricci, D., Scarpetta, G., Skottfelt, J., Southworth, J., Surdej, J., Wambsganss, J., Zimmer, F., The MiNDSTEp Consortium, Batista, V., Beaulieu, J. P., Brillant, S., Cassan, A., Cole, A., Corrales, E., Coutures, Ch., Dieters, S., Greenhill, J., Kubas, D., Menzies, J., The PLANET Collaboration
The Astrophysical Journal, 728, 120 (2011)

31. "OGLE-2009-BLG-092/MOA-2009-BLG-137: A Dramatic Repeating Event with the Second Perturbation Predicted by Real-time Analysis"
Ryu, Y.-H., Han, C., Hwang, K.-H., Street, R., Udalski, A., Sumi, T., Fukui, A., Beaulieu, J.-P., Gould, A., Dominik, M., Abe, F., Bennett, D. P., Bond, I. A., Botzler, C.S., Furusawa, K., Hayashi, F., Hearnshaw, J. B., Hosaka, S., Itow, Y., Kamiya, K., Kilmartin, P. M., Korpela, A., Lin, W., Ling, C. H., Makita, S., Masuda, K., Matsubara, Y., Miyake, N., Muraki, Y., Nishimoto, K., Ohnishi, K., Perrott, Y. C., Rattenbury, N., Saito, To., Skuljan, L., Sullivan, D. J., **Suzuki, D.**, Sweatman, W. L., Tristram, P. J., Wada, K., Yock, P. C. M., The MOA Collaboration, Szymański, M. K., Kubiak, M., Pietrzyński, G., Poleski, R., Soszyński, I., Szewczyk, O., Wyrzykowski, Ł., Ulaczyk, K., The OGLE Collaboration, Bos, M., Christie, G. W., Depoy, D. L., Gal-Yam, A., Gaudi, B. S., Kaspi, S., Lee, C.-U., Maoz, D., McCormick, J., Monard, B., Moorhouse, D., Pogge, R. W., Polishook, D., Shvartzvald, Y., Shporer, A., Thornley, G., Yee, J. C., The μFUN Collaboration, Albrow, M. D., Batista, V., Brillant, S., Cassan, A., Cole, A., Corrales, E., Coutures, Ch., Dieters, S., Fouqué, P., Greenhill, J., Menzies, J., The PLANET Collaboration, Allan, A., Bramich, D. M., Browne, P., Horne, K., Kains, N., Snodgrass, C., Steele, I., Tsapras, Y., RoboNet Collaboration, Bozza, V., Burgdorf, M. J., Calchi Novati, S., Dreizler, S., Finet, F., Glitrup, M., Grundahl, F., Harpsøe, K., Hessman, F. V., Hinse, T. C., Hundertmark, M., Jørgensen, U. G., Liebig, C., Maier, G., Mancini, L., Mathiasen, M., Rahvar, S., Ricci, D., Scarpetta, G., Skottfelt, J., Surdej, J., Southworth, J., Wambsganss, J., Zimmer, F., The MiNDSTEp Collaboration
The Astrophysical Journal, 723, 81 (2010)

32. "Determining the Physical Lens Parameters of the Binary Gravitational Microlensing Event MOA-2009-BLG-016"
Hwang, K.-H., Han, C., Bond, I. A., Miyake, N., Abe, F., Bennett, D. P., Botzler, C. S., Fukui, A., Furusawa, K., Hayashi, F., Hearnshaw, J. B., Hosaka, S., Itow, Y., Kamiya, K., Kilmartin, P. M., Korpela, A., Lin, W., Ling, C. H., Makita, S., Masuda, K., Matsubara, Y., Muraki, Y., Nishimoto, K., Ohnishi, K., Perrott, Y. C., Rattenbury, N., Saito, To., Sako, T., Skuljan, L., Sullivan, D. J., Sumi, T., **Suzuki, D.**, Sweatman, W. L.,

Tristram, P. J., Wada, K., Yock, P. C. M., The MOA Collaboration, Depoy, D. L., Gaudi, B. S., Gould, A., Lee, C.-U., Pogge, R. W., The μFUN Collaboration
The Astrophysical Journal, 717, 435 (2010)

33. "Chemical evolution of the Galactic bulge as traced by microlensed dwarf and subgiant stars. II. Ages, metallicities, detailed elemental abundances, and connections to the Galactic thick disc"
Bensby, T., Feltzing, S., Johnson, J. A., Gould, A., Adén, D., Asplund, M., Meléndez, J., Gal-Yam, A., Lucatello, S., Sana, H., Sumi, T., Miyake, N., **Suzuki, D.**, Han, C., Bond, I., Udalski, A.
Astronomy and Astrophysics, 512, A41 (2010)

Appendix B

List of Presentations

B.1 International Conference

1. "Planet frequency beyond the snow line from MOA-II observations in 2007-2011"
   Daisuke Suzuki, for the MOA collaboration
   1st Doha International Astronomy Conference、Qatar National Convention Centre, Doha, Qatar、February, 2013
2. "Detection Efficiencies of Low-magnification Events in MOA-II Data"
   Daisuke Suzuki, for the MOA collaboration
   Science with a Wide-field Infrared Telescope in Space and The 16th International Conference on Gravitational Microlensing、Pasadena, CA, USA、February, 2012
3. "Detection efficiency of planets in the low magnified gravitational microlensing events"
   Daisuke Suzuki, for the MOA collaboration
   Joint Assembly: JSPS-DST Asia Academic Seminar CPS 8th International School of Planetary Sciences Challenges in Astronomy: Observational Advances、 Hyogo, Japan、September, 2011
4. "Detection Efficiency of Planets in Low-Mag Event, MOA-2009-BLG-266"
   Daisuke Suzuki, for the MOA collaboration
   2011 Sagan Exoplanet Summer Workshop、California Institute of Technology, Pasadena, CA, USA、July, 2011
5. "Follow up observations of microlensing planets by IRSF"
   Daisuke Suzuki, for the MOA collaboration
   10 years of Infrared Survey Facility and the future、Nagoya University, Nagoya, Japan、November, 2010

B.2 Domestic Conference

1. "MOA-2008-BLG-379Lb：K 型星周りの巨大ガス惑星"
   鈴木大介、他 MOA グループ
   P216a　日本天文学会 2013 年秋季年会、東北大学、2013 年 9 月

2. “MOA-II による snow line の外側における惑星頻度”
   鈴木大介、他 MOA グループ
   P52b　日本天文学会 2013 年春季年会、埼玉大学、2013 年 3 月

3. “MOA-II による惑星の存在確率への制限”
   鈴木大介、他 MOA グループ
   P205a　日本天文学会 2012 年秋季年会、大分大学、2012 年 9 月

4. “Detection efficiencies of low-magnification microlensing events in MOA-II data”
   鈴木大介、他 MOA コラボレーション
   第 8 回太陽系外惑星大研究会、熱海、2012 年 4 月

5. “MOA-II による系外惑星探査：2011 年の結果”
   鈴木大介、他 MOA グループ
   P218a　日本天文学会 2012 年春季年会、龍谷大学、2012 年 3 月

6. “低増光率重力マイクロレンズイベントにおける惑星の検出効率”
   鈴木大介、他 MOA コラボレーション
   P64a　日本天文学会 2011 年秋季年会、鹿児島大学、2011 年 9 月

7. “低増光率重力マイクロレンズイベントにおける検出効率”
   鈴木大介、他 MOA コラボレーション
   P63a　日本天文学会 2011 年春季年会、筑波大学、2011 年 3 月

8. “最小質量比重力マイクロレンズイベント MOA-2009-BLG-266 の検出効率”
   鈴木大介、他 MOA グループ
   P51a　日本天文学会 2010 年秋季年会、金沢大学、2010 年 9 月